Static and dynamic properties of QCD at finite temperature

**Dissertation zur Erlangung des Grades
„Doktor der Naturwissenschaften"**

vorgelegt beim

Fachbereich Physik, Mathematik und Informatik
Johannes Gutenberg Universität in Mainz

JG|U

JOHANNES GUTENBERG
UNIVERSITÄT MAINZ

Daniel Robaina Fernández

geboren in Madrid

Mainz, 21. Januar 2016

Daniel Robaina Fernández: *Static and dynamic properties of QCD at finite temperature*

Datum der mündlichen Prüfung: 1. Juni 2016

Abstract

In this work we study strongly interacting matter at finite temperature. We consider Quantum Chromodynamics (QCD) mainly with two degenerate flavors of quarks below the phase transition. We rely on the Lattice approach to treat QCD in the non-perturbative regime. In this framework, the inclusion of finite temperature is fairly straightforward but extracting real-time properties from the Monte Carlo data is a non-trivial problem. The focus of the work is put on the pion quasiparticle. In particular we investigate the change in its dispersion relation due to thermal effects and compare it to the vacuum situation. At low momenta, the dispersion relation depends on a Renormalization Group Invariant (RGI) parameter $u(T)$ called the 'pion velocity' that can be calculated in terms of screening (or static) quantities. Those can be calculated with standard numerical techniques. We calculate the pion velocity for several values of the temperature at different quark masses and find strong evidence that boost invariance is violated due to thermal effects. Our findings are in qualitative agreement with analytic calculations in Chiral Perturbation Theory (ChPT). In addition, we explore a method to access information in spectral functions: the Backus-Gilbert method which has never been applied to QCD before and has the advantage over more traditional methods that a model-independent estimator for the spectral function can be defined. As a complementary project, we investigate SU(3) pure Yang-Mills theory with shifted boundary conditions. We use the latter to determine the renormalization constant of the off-diagonal elements of the energy-momentum-tensor at various values of the bare coupling. This constant is crucial for taking the continuum limit of energy-momentum-tensor-correlators from which transport properties of the system can be derived.

Contents

Chapter 1

Introduction

In the last three years, two Nobel prizes in Physics were awarded to the high energy physics community for outstanding research contributions that have a direct impact on the Standard Model of Particle Physics (SM). The discovery of the Higgs Boson by the CMS and ATLAS experiments at CERN in 2012 [1, 2] confirmed the ideas and concepts first introduced more than fifty years ago by P. Higgs, F. Englert and R. Brout [3, 4]. We think now we have a solid understanding about how all known fermions obtain their masses and we can successfully marry gauge invariance with the existence of massive vector gauge bosons. Although the beauty and consistency of the Standard Model is not doubted by any high energy theorist or experimentalist, by this time, the community already was aware that the Standard Model could by no means be the end of the story.

Apart from the obvious "embarrassing" fact that the first ever discovered elementary force by Newton is not included in the theory due to its inability to be naively quantized, there are a number of physics effects that the SM is unable to predict. One of the experimental pieces of evidence of Beyond Standard Model (BSM) physics are neutrino oscillations. Due to the chiral character of the weak force, the fathers of the Standard Model assumed only the existence of a left-handed neutrino and the absence of its right-handed component. This immediately pointed to a vanishing mass for the neutrino particle which was consistent with the experiments of the time. Now we know that neutrinos have tiny non-zero masses [5]. The disappearance of neutrinos with one flavor and the appearance of them with a different flavor led to the idea of neutrino oscillations. This phenomenon can only be explained if one assumes non-vanishing masses for them.

The history of the universe must account for all available information. It is believed that around $t \sim 10^{-12}s$ after the Big Bang, when temperatures were around 100 GeV, the electroweak transition took place. The Higgs field acquired a non-zero expectation value and the electroweak gauge bosons got their masses through the Higgs mechanism. The primitive universe formed out of the elementary particles cooled and expanded further until it reached temperatures of 100 MeV ($t \sim 10^{-6}s$). At this point the QCD phase transition happened whose consequences we investigate to some extent in this thesis. The hadronization process led to the formation of hadrons and the zoo of particles discovered in the fifties. In order to study a complicated system like a quark-antiquark pair confined inside a meson, we rely on the Lattice framework. In this formulation of Quantum Field theories, temperature effects can be included straightforwardly and strongly coupled systems can be analyzed in a systematic improvable manner. In this work we will not directly investigate the QCD phase transition. Its nature has been extensively studied by lattice theorists over the last decade (see e.g. [6,7] and references therein). By contrast, we will focus on the dynamics of QCD right below the phase transition and compare our findings with the standard hadronic physics at zero temperature. By doing so, we will make use of well established techniques and will investigate some of the problems that arise when following "the Lattice path".

When analyzing a statistical system at finite temperature there are two conceptually different quantities one can encounter: static and dynamic. While the former characterizes the system in a time-independent way, the latter makes contact to properties away from equilibrium. The challenge is then to obtain as much information from the dynamic response of the system by measuring static quantities. All needed information is encoded in spectral functions (see Sec. 2.3.1) that are in principle calculable from Euclidean correlators. In particular their slope at the origin makes contact with transport coefficients that are defined through the hydrodynamic description and the famous Kubo Formulas [8]. One example where contact between static and dynamic quantities can be made is presented in Chapter 6 where we show how to relate the shift in the pole of the pion quasiparticle to screening quantities.

We focus on the pion since chiral symmetry assures a vanishing mass in the chiral limit regardless of temperature effects. This fact can be further exploited

in order to constrain the form of spectral functions and make a theoretical prediction that we can test on the Lattice. The shift in the pole of the pion at finite temperature is an effect very difficult to test experimentally due to the difficulty of isolating a single pion and measure its energy in the presence of an equilibrated thermal bath that can only be produced in Heavy Ion Collisions (HIC) for a very tiny fraction of time. The results can be used more directly as input for various models that require information from the relevant quasiparticles and their dispersion relations at different temperatures.

From the cosmological point of view, the theory of strong interactions is at the origin of the formation of the observable universe although it represents only a tiny $\sim 5\%$ of the overall existing energy. Still, high energy physicists have overwhelming evidence that it is the correct theory that describes the interactions between quarks and gluons. Because of confinement, experiments are unable to see free quarks or gluons; instead they see hadronized jets of particles. The remarkable fact that Lattice Gauge theory was able to reproduce the low-lying QCD spectrum of bound states [9] was important evidence that QCD worked also at low-energies.

This thesis is organized as follows: Chapter 2 is devoted to introducing some concepts of Quantum Field theories in connection to the statistical interpretation. In Chapter 3 we provide an introduction to QCD and explain the importance of Chiral Symmetry which is mandatory to understand QCD thermodynamics. Chapter 4 is devoted to Lattice Gauge theory, a well established formulation of QFT on a finite and discrete space-time box. Chapter 5 shows and example of how one can use different types of boundary conditions in our advantage to better sample the QCD parameter space. Chapter 6 is devoted to the dynamics of QCD below the phase transition. Finally, Chapter 7 summarizes our findings and we state our conclusions.

Chapter 2

Basic concepts of QFT

Throughout this chapter we will introduce some carefully selected topics which will be of mayor importance throughout this work. Constant references to ideas and arguments of this chapter will be made. It is not intended to contain rigorous proofs or detailed explanations on any of the various aspects. The goal is rather to highlight the key concepts so as to gain intuition and be in a better position to understand some of the more elaborated tools used in the following chapters.

2.1   Path integral quantization

Ever since the path integral formulation was fully introduced by Feynman and Hibbs in 1965 so as to quantize field theories, the insight on the framework has grown substantially. Let us briefly review the basic ingredients and concepts within a toy model: the free scalar field theory. Consider the classical field equation

$$(\Box + M^2)\phi(x) = 0 \tag{2.1.1}$$

This equation can be derived from an action principle $\delta S = 0$ where

$$S[\phi] = -\frac{1}{2} \int d^4x \, \phi(x)(\Box + M^2)\phi(x) \tag{2.1.2}$$

is the action that follows from the Lorentz covariant Lagrangian density in Minkowski space with metric $g = (+ - --)$

$$\mathcal{L} = \frac{1}{2}\partial^\mu\phi\partial_\mu\phi - \frac{1}{2}M^2\phi^2. \tag{2.1.3}$$

The expectation value of any operator formed out of a time-ordered product of n fields can be written as

$$\langle 0|\mathcal{O}(x_1, ..., x_n)|0\rangle = \frac{\int \mathcal{D}\phi\ \mathcal{O}(x_1, ..., x_n)e^{iS[\phi]}}{Z} \tag{2.1.4}$$

where $|0\rangle$ stands for the vacuum of the system and

$$Z = \int \mathcal{D}\phi e^{iS[\phi]} \tag{2.1.5}$$

is called the partition function or path integral of the theory. The integration measure should be formally understood as an infinite dimensional integral that can be written as

$$\mathcal{D}\phi = \prod_{x \in \mathbb{R}^4} d\phi(x). \tag{2.1.6}$$

This is a well defined quantum description of our system because $\int \mathcal{D}\phi$ denotes the sum over all possible field configurations including those that do not satisfy the classical field equation written in Eq. (2.1.1). They represent quantum fluctuations and hence do not follow from an action minimizing principle. This formulation of Quantum Mechanics is not only useful at the formal level but also intuition is gained. By coupling the partition function to external sources one arrives at the generating functional $Z[J]$. The Taylor expansion of this object contains all Green Functions of the theory and therefore via the Lehmann-Symanzik-Zimmermann (LSZ) formula [10] any scattering process can be written in terms of those. Knowing all Green Functions means in practice that the theory has been solved. Unfortunately, this can only be done for a handful of theories that enjoy symmetries like scale invariance.

2.2   Quantum Statistical mechanics

Since this work deals with systems in the presence of a thermal bath at a constant temperature T we find it useful to introduce briefly the statistical description of a quantum system. Once a given system has a very high number of degrees of freedom, the number of micro states in which the system can appear grows very rapidly. It is therefore a problem to keep track of the dynamics of each of them, so one needs a special framework in order to treat the system globally and concentrate on its collective behavior. The thermodynamic description introduces a set of global variables like pressure, temperature or entropy that characterize the system from a global point of view, regardless of the dynamics of the internal degrees of freedom. The formalism we are about to introduce is used to describe bulk properties in or near equilibrium. The framework of Quantum Statistical Mechanics shares a lot of common features with the Path Integral formulation of Quantum Field Theory. As an illustrative example, we will work in the grand canonical ensemble. This describes a system that can exchange particles as well as energy with a reservoir. The thermodynamic variables of interest are temperature T, volume V and chemical potential μ which are fixed quantities. We begin with the definition of a density matrix $\hat{\rho}$

$$\hat{\rho} = \exp\left\{-\beta(\hat{H} - \mu_i \hat{N}_i)\right\} \tag{2.2.1}$$

where $\beta = 1/T$, $\hat{H}$ is the Hamiltonian of the system and $\hat{N}_i$ are conserved number operators, which e.g. can measure particle number or any other conserved charge. In terms of the density matrix, the expectation value of any operator corresponding to a meaningful observable is calculated as

$$\langle \mathcal{O} \rangle = \frac{\text{Tr}\hat{A}\hat{\rho}}{\text{Tr}\hat{\rho}} \tag{2.2.2}$$

where the trace is understood over all states that form the Hilbert space. The definition goes back to quantum mechanics and can be derived very easily. It confronts the situation where a system can appear in a so called mixed state $|\psi_k\rangle$ with probability p_k. In this basis, ρ is a diagonal matrix with the probabilities

along the diagonal so it can be written as

$$\hat{\rho} = \sum_k p_k \, |\psi_k\rangle \, \langle\psi_k| \,. \tag{2.2.3}$$

One can now choose a basis of eigenvectors $\{|\phi\rangle\}$ that form an orthonormal basis that fully diagonalizes e.g. the hamiltonian $\hat{H}$ (it could be any other hermitian operator since the trace operation is invariant) and write

$$\rho_{ij} = \langle\phi_i|\hat{\rho}|\phi_j\rangle = \sum_k p_k \, \langle\phi_i|\psi_k\rangle \, \langle\psi_k|\phi_j\rangle \,. \tag{2.2.4}$$

The expectation value of any hermitian operator in the "mixed system" is the sum of expectation values corresponding to all mixed states times the probability that the system is in the mixed state

$$\langle A\rangle = \sum_k p_k \, \langle\psi_k|A|\psi_k\rangle = \sum_{ijk} p_k \, \langle\psi_k|\phi_i\rangle \, \langle\phi_i|A|\phi_j\rangle \, \langle\phi_j|\psi_k\rangle = \sum_{ij} \rho_{ji} a_{ij} = \mathrm{Tr}\hat{A}\hat{\rho}. \tag{2.2.5}$$

The condition that $\sum_k p_k = 1$ translates into a normalized density matrix with unit trace, so $\mathrm{Tr}\hat{\rho} = 1$.

2.3 Thermal field theory

Taking the last section as an illustrating starting point, we want to make the connection to a thermal field theory. Both expressions written in Eq. (2.1.4) and Eq. (2.2.2) are very similar to each other. We can then identify the trace of the density matrix with the thermal field theory partition function Z and write

$$Z(T,V,\mu) = \mathrm{Tr}\exp\left\{-\beta(\hat{H} - \mu_i\hat{N}_i)\right\}. \tag{2.3.1}$$

Its logarithm makes connection to the Helmholtz free energy

$$F = -T\log Z(T,V,\mu). \tag{2.3.2}$$

Taking first derivatives with respect to T, V or μ one arrives at pressure, entropy or charge number potentials

$$S = \frac{\partial (T \log Z)}{\partial T}, \tag{2.3.3}$$

$$P = \frac{\partial (T \log Z)}{\partial V}, \tag{2.3.4}$$

$$N_i = \frac{\partial (T \log Z)}{\partial \mu_i}. \tag{2.3.5}$$

Second order derivatives are related to specific heats (at constant temperature or volume) and susceptibilities. From the quantum field theory perspective (at zero temperature), it turns out to be very natural that the free energy is the fundamental quantity from which the rest of thermodynamic potentials are derived. The reason behind it is that the generating functional $W[J]$ which is also defined proportional to $\log(Z[J])$ is the one that gives rise to all diagrams without bubble diagrams. These are the ones that ultimately contribute to the interaction term in any S-matrix element as opposed to $Z[J]$. In order to fully establish the parallelism and include Lorentz invariance into the framework, one needs to change from states to fields (a very illuminating explanation on this statement can be found in Peskin & Schröder). We therefore introduce scalar fields and their conjugate momenta operators in the Schrödinger picture

$$\hat{\phi}(x) \ket{\phi} = \phi(x) \ket{\phi} \tag{2.3.6}$$

$$\hat{\pi}(x) \ket{\pi} = \pi(x) \ket{\pi}. \tag{2.3.7}$$

Both set of fields fulfill continuum completeness and orthogonality conditions. We can write the partition function in terms of the fields as follow

$$Z(T, V, \mu) = \operatorname{Tr} \exp\left\{ -\beta(\hat{H} - \mu_i \hat{N}_i) \right\} = \sum_a \int d\phi_a \left\langle \phi_a \right| \exp\left\{ -\beta(\hat{H} - \mu_i \hat{N}_i) \right\} \left| \phi_a \right\rangle \tag{2.3.8}$$

where the index a labels all states that the system can be in. The term $e^{-\beta \hat{H}}$ looks very similar to the ordinary evolution operator in quantum mechanics $U(t, t') = e^{-i\hat{H}(t-t')}$. The only difference is that time is Wick rotated such that $t \to \tau = it$. Moreover, there is a fixed upper bound for imaginary times τ which is $\beta = 1/T$ that plays the role of temperature. Thus, in this formulation one gives

up real time in favor of temperature. One can calculate the matrix element $\left\langle \phi_a \right| \exp\left\{ -\beta(\hat{H} - \mu_i \hat{N}_i) \right\} \left| \phi_a \right\rangle$ (see e.g. [11]) and finally arrive at

$$Z(T, V, \mu) = \mathcal{N}_{\pi(x)} \int d\phi \exp\left(\int_0^\beta d\tau \int d^3x \, \mathcal{L}^E(\phi, \partial\phi) \right) \qquad (2.3.9)$$

where in the process that transforms the hamiltonian into the euclidean lagrangian density, the conjugate momenta $\pi(x)$, which were treated initially as independent degrees of freedom, are integrated over, since they appear only as gaussian integration variables yielding an irrelevant absolute normalization that cancels out whenever an expectation value is taken. One can show explicitly that scalar fields are periodic in τ. This is a consequence of the trace operation that appeared naturally in the quantum mechanical description of the density matrix. For this purpose we use the definition of the thermal Green function

$$G(x, y, \tau_1, \tau_2) = Z^{-1}\text{Tr}\left\{ \hat{\rho} T_\tau \left(\hat{\phi}(x, \tau_1)\hat{\phi}(y, \tau_2) \right) \right\} \qquad (2.3.10)$$

where T_τ is the time ordering product for bosons that acts like

$$T_\tau \left(\hat{\phi}(x, \tau_1)\hat{\phi}(y, \tau_2) \right) = \hat{\phi}(x, \tau_1)\hat{\phi}(y, \tau_2)\theta(\tau_1 - \tau_2) + \hat{\phi}(y, \tau_2)\hat{\phi}(x, \tau_1)\theta(\tau_2 - \tau_1).$$
$$(2.3.11)$$

We set $\mu_i = 0$ such that $\hat{\rho} = \frac{1}{Z}e^{-\beta\hat{H}}$ and we use the cyclic property of the trace in order to write

$$
\begin{aligned}
G(x, y, \tau, 0) &= Z^{-1}\text{Tr}\left(e^{-\beta\hat{H}}\hat{\phi}(x, \tau)\hat{\phi}(y, 0) \right) & (2.3.12) \\
&= Z^{-1}\text{Tr}\left(\hat{\phi}(y, 0)e^{-\beta\hat{H}}\hat{\phi}(x, \tau) \right) & (2.3.13) \\
&= Z^{-1}\text{Tr}\left(e^{-\beta\hat{H}}e^{\beta\hat{H}}\hat{\phi}(y, 0)e^{-\beta\hat{H}}\hat{\phi}(x, \tau) \right) & (2.3.14) \\
&= Z^{-1}\text{Tr}\left(e^{-\beta\hat{H}}\hat{\phi}(y, \beta)\hat{\phi}(x, \tau) \right) & (2.3.15) \\
&= Z^{-1}\text{Tr}\left(\hat{\rho} T_\tau \left(\hat{\phi}(x, \tau)\hat{\phi}(y, \beta) \right) \right) = G(x, y, \tau, \beta). & (2.3.16)
\end{aligned}
$$

The space-time domain is then always chosen to be $S^1 \times \mathbb{R}^3$ with a period of β. This means that scalar fields admit a Fourier expansion in imaginary time that

can be written as

$$\phi(x, \tau) = \sqrt{\frac{\beta}{V}} \sum_n \sum_{\mathbf{p}} e^{i(\mathbf{p}\mathbf{x} + \omega_n \tau)} \tilde{\phi}_n(\mathbf{p}) \tag{2.3.17}$$

where the values of $\omega_n = 2\pi n/\beta$ are called Matsubara frequencies with $n \in \mathbb{Z}$. If the spatial extent is finite (as in the Lattice case) the momenta are also discretized in units of $p_i = 2\pi n_i/L$. For the case of fermions, being Grassman variables, the treatment is the same with the only difference that Matsubara frequencies are multiples of $\omega_n = \pi(2n+1)/\beta$ due to the anti-periodicity of the fermionic fields $\psi(\mathbf{x}, 0) = -\psi(\mathbf{x}, \beta)$.

As a concluding remark, one should note that the necessity of Wick rotating into euclidean time has advantages and drawbacks. On the one side, we have shown that there exists a strong parallelism between quantum statistical mechanics and the imaginary time formulation of thermal field theory. The euclidean partition function e^{-S_E} acts like a Boltzmann weight suppressing field configurations that are away from the classical solution where the action gets minimal. Taking the lagrangian density of the free scalar theory of Sec. 2.1 as an example, it can be easily shown that indeed the change of variables $t \to \tau = it$ and integration by parts yields a real positive definite action quadratic in the fields

$$iS[\phi] = \frac{i}{2} \int_{-\infty}^{\infty} dt \int d^3x \ \left(\partial_t \phi(t, \mathbf{x}) \partial_t \phi(t, \mathbf{x}) - \nabla^2 \phi(t, \mathbf{x}) - M^2 \phi^2(t, \mathbf{x}) \right) \tag{2.3.18}$$

$$-S_E[\phi] = -\frac{1}{2} \int_0^{\beta} d\tau \int d^3x \ \left(\partial_\tau \phi(\tau, \mathbf{x}) \partial_\tau \phi(\tau, \mathbf{x}) + (\nabla \phi(\tau, \mathbf{x}))^2 + M^2 \phi^2(\tau, \mathbf{x}) \right). \tag{2.3.19}$$

The link between statistical mechanics and QFT cannot be achieved at real time due to the strong oscillating function e^{iS} one has in Minkowski metric. In addition, if one computes numerically expectation values at imaginary times (e.g. via Monte Carlo methods) it is an ill-posed problem to go back to real time by analytical continuation as we will state in Sec. 2.3.2. Nevertheless, this problem will only affect dynamic quantities that describe the response of the system to time-dependent perturbations as opposed to time-integrated or static quantities whose calculation is safe.

2.3.1   Introduction to spectral functions

Since important for later sections, we will quote some of the most important relations between euclidean and retarded correlators in the presence of a thermal bath in the approximation of zero chemical potential. The goal is to introduce the notion of a spectral function: a common function to all different type of correlators that unambiguously carries every perturbative and non-perturbative contribution. We start with Eq. (2.3.10) and define the form of a general time ordered thermal correlator for the case of two general composite operators A and B. We assume that the density matrix is normalized and both operators are projected to zero momentum such that the space-dependence is integrated over. The two possible contributions can be written as

$$G_>^{AB}(t) = \text{Tr}\{\hat{\rho} A(t) B(0)\} \tag{2.3.20}$$
$$G_<^{AB}(t) = \text{Tr}\{\hat{\rho} B(0) A(t)\} \tag{2.3.21}$$

These two equations can be combined into a commutator such that

$$G^{AB}(t) = i\text{Tr}\{\hat{\rho}[A(t), B(0)]\} = i(G_>^{AB}(t) - G_<^{AB}(t)). \tag{2.3.22}$$

It satisfies the relations

$$G^{AB}(-t) = -G^{BA}(t), \qquad G^{A^\dagger B^\dagger}(t) = G^{AB}(t^*)^* \tag{2.3.23}$$

and vanishes outside the light-cone, a consequence of the causality property of the theory. The euclidean correlator plays a fundamental role in the lattice formulation since it is this form of the correlator that can be computed with Monte Carlo techniques at imaginary times $\tau \in [0, \beta]$. It can be related to the above defined quantities as

$$G_E^{AB}(\tau) = G_>^{AB}(-i\tau) \tag{2.3.24}$$

The integral transform over the positive half axis defines the retarded correlator

$$G_R^{AB}(\omega) = \int_0^\infty dt e^{i\omega t} G^{AB}(t) \tag{2.3.25}$$

and for the case of $B = A^\dagger$ (as it is for the most commonly used correlators) the spectral function is defined as

$$\rho(\omega) = \frac{1}{\pi}\text{Im}G_R^{AA^\dagger}(\omega). \tag{2.3.26}$$

The reality property is also verified for the euclidean correlator $G_E^{AA^\dagger}(t)$ as well as for the spectral function. In addition, if $A^\dagger = \pm A$ the euclidean correlator is up to a global sign symmetric around $t = \beta/2$. We write for this case the relation between the spectral function and the euclidean correlator which then reads

$$G_E^{AA^\dagger}(t) = \int_0^\infty d\omega \rho(\omega)\frac{\cosh(\omega(\beta/2 - t))}{\sinh(\omega\beta/2)}. \tag{2.3.27}$$

The previous integral equation is of major importance in this thesis. The numerically ill-posed inversion of this equation to access the information in the spectral function is one of the goals of this work. Since the euclidean correlator is periodic in the interval $[0, \beta]$, we can expand it in a Fourier series such that

$$\tilde{G}_E(\omega_n) = \int_0^\beta dt e^{i\omega_n t}G_E(t) \tag{2.3.28}$$

where $\omega_n = 2\pi n/\beta$, $n \in \mathbb{Z}$ and the full euclidean correlator is recovered by summing over all Matsubara modes

$$G_E(t) = \frac{1}{\beta}\sum_{\omega_n}\tilde{G}_E(\omega_n)e^{-i\omega_n t}. \tag{2.3.29}$$

Finally one can show that the analytic continuation of the euclidean correlator in frequency space is the retarded correlator

$$G_R(i\omega_n) = \tilde{G}_E(\omega_n) \qquad n \geq 0 \tag{2.3.30}$$

and via Eq. (2.3.26) one arrives at the spectral function. The zero mode contribution needs special treatment (see e.g. [12]) if the spectral function is singular at the origin. Examples of perturbative results of spectral functions calculated via analytic continuation can be found in [13, 14] among others.

2.3.2   A numerically ill-posed problem

After having calculated the euclidean correlator in imaginary time in a typical thermal lattice like the ones used in this work, one ends up with a function evaluated at most at $N_\tau = 12$ points. Therefore it is clear that there is an infinite number of spectral functions that upon integrated with the kernel will yield the same euclidean correlator. Even if we had an enormous computing power such that we could simulate on very big thermal lattices, the problem is still not solved. Data will come with error bars, and it can be shown that the uncertainty of the spectral function decreases only logarithmically, meaning that the euclidean correlator needs exponentially increasing statistics which is completely unfeasible with known standard techniques. Therefore, the inversion of Eq. (2.3.27) is numerically an ill-posed problem. Various attempts of solving this problem have been tried. The most popular method in the lattice community is called the Maximum Entropy Method (MEM) (see [15–17] among others). In this method the guiding principle for the selection of the most likely solution given the finite number of lattice data points with errors and an input default model is Bayesian driven. The drawback of this approach is the prior selection of a default model whose parameters will be determined by MEM such that the solution is the most probable one. Therefore all studies relying on MEM need to make sure to disentangle correctly physical peak structures from systematic artifacts of the default model. We used this method in [18] but the results are not reproduced in this work.

By contrast, we make use of the Backus-Gilbert method [19–21] that will be introduced in Sec. 6.5.6 (see also Appendix F for a Mock-Data study). It has the advantage over MEM of not requiring any a priori selected model. Instead, a completely model-independent estimator for the true spectral function can always be defined. In addition, the formulation of the method ensures that if the target spectral function is constant, the estimator agrees exactly. The price to pay is the calculation of a resolution function that optimally balances error reduction versus resolving power. More details are given in the above mentioned sections.

2.4   Ward-Takahashi identities

Ward Identities [22, 23] were introduced in the 1950's in the context of Quantum Electrodynamics. It was shown then that divergent structures of the bare

parameters were related. Nowadays, Ward Identities are well established relations upon expectation values and are of major importance in the framework of Quantum Field Theory. They are valid at the non-perturbative level and therfore play an outstanding role in Lattice Theories (for a review on Lattice Ward Identities see [24].) Generally speaking, Ward Identities relate the divergence of a Green Function to some linear combination of other Green Functions. They are particularly interesting if they contain a current whose divergence vanishes. In the classical theory, this corresponds to a conserved current and Noether Theorem [25] implies an underlying symmetry. When inserted into expectation values, Ward Identities tell us how this symmetry is realized at the quantum level.

Ward Identities are derived by calculating the infinitesimal change of the partition function Z corresponding to an infinitesimal local transformation of the fields. Consider the expectation value of a multilocal operator in an abelian gauge theory like QED in euclidean space

$$\langle 0|\mathcal{O}(x_1,...,x_n)|0\rangle = \frac{1}{Z}\int \mathcal{D}[A_\mu]\mathcal{D}[\bar{\psi},\psi]\mathcal{O}(x_1,...,x_n)\exp\left(-S_G[A_\mu]-S_F[\bar{\psi},\psi]\right) \tag{2.4.1}$$

We perform a local transformation of the fermionic fields $\bar{\psi}$ and ψ as

$$\delta^\epsilon\psi = \epsilon(x)\psi, \qquad \delta^\epsilon\bar{\psi} = -\bar{\psi}\epsilon(x). \tag{2.4.2}$$

The expectation value of Eq. (2.4.1) is invariant under any change of the fermionic fields since they can be seen as pure integration variables. This leads to

$$\frac{\delta}{\delta\epsilon(x)}\langle 0|\mathcal{O}(x_1,...,x_n)|0\rangle = 0. \tag{2.4.3}$$

The previous expression can also be written as

$$\left\langle\frac{\delta\mathcal{O}(x_1,...,x_n)}{\delta\epsilon(x)}\right\rangle = \left\langle\mathcal{O}(x_1,...,x_n)\frac{\delta S_F}{\delta\epsilon(x)}\right\rangle. \tag{2.4.4}$$

Particularly interesting cases appear when the transformation leaves the action invariant, since the r.h.s of the previous equation vanishes. In Appendix E we provide a derivation for the case of Chiral Ward Identities in two-flavor QCD for two-point functions. They can be generalized to finite temperature and are used extensively in Chapter 6 to formally derive some of our main results.

Chapter 3

Quantum Chromodynamics (QCD)

In this chapter we will formally introduce the continuum Lagrangian of QCD and briefly state a few of its most important properties. In the modern approach to Quantum Field Theory, symmetries play an outstanding role since they dictate, for example, the allowed operators to be included in the lagrangian density so special attention will be devoted to the symmetry properties. In order to better establish the relation to lattice QCD we will be working directly in euclidean metric

$$\{\gamma_\mu, \gamma_\nu\} = 2\delta_{\mu\nu}\mathbb{I}. \tag{3.0.1}$$

3.1 Euclidean QCD lagrangian density

QCD is the theory of the strong interactions and together with the electromagnetic and the weak force form the Standard Model of Particle Physics. The matter content of QCD consists of 6 different spin-1/2 fermions which are called quarks living in the fundamental representation of the gauge group $SU(3)$. Thus, they can appear in any combination of three different color-states (red, green and blue). They are represented by a Dirac field $\psi^f(x)_{\alpha,a}$ where f, α and a represent the flavor, dirac and color-indices respectively. Like in any gauge theory, QCD has its own massless vector gauge boson of spin-1 called the gluon (g). It is represented by a lorentz-vector $A_{\mu,b}(x)$ where μ and b are lorentz and color-indices (throughout this work we will not always show all indices explicitly; only when important for the discussion). The gauge field lives in the adjoint representation so b runs from 1 to $N^2 - 1 = 8$. The only terms compatible with being locally invariant under the

$SU(3)$ gauge group and have dimension equal or less than 4 are (without θ-term)

$$\mathcal{L}[\bar{\psi}, \psi, A]_{\mathrm{QCD}} = \sum_{f=u,d,s,c,b,t} \bar{\psi}^f (\gamma_\mu(\partial_\mu + iA_\mu) + m^f)\psi^f + \frac{1}{2g^2}\mathrm{Tr}[F_{\mu\nu}F_{\mu\nu}]. \quad (3.1.1)$$

The field strength tensor is defined in the usual way taking into account the fact that $SU(3)$ is a non-abelian group

$$F_{\mu\nu}^a = \partial_\mu A_\nu^a - \partial_\nu A_\mu^a - f_{abc}A_\mu^b A_\nu^c. \quad (3.1.2)$$

These new terms are of fundamental importance in QCD since they give rise to the self-interaction vertices of the gluon field. Those are responsible for some of the most interesting properties of QCD like asymptotic freedom. The structure constants f_{abc} are defined via the common definition for any Lie group

$$[T^a, T^b] = if_{abc}T^c, \quad (3.1.3)$$

where T^a are the generators of the $SU(3)$ group in any representation $\mathcal{R}$. If $\mathcal{R}$ is the fundamental representation, the generators are the well known Gell-Mann matrices which are of dimension 3. The gauge field A_μ^a, lives in the adjoint representation. In this case the generators are 8 by 8 matrices fulfilling Eq. (3.1.3). In contrast to QED, Quantum Chromodynamics is an asymptotically free theory due to its non-abelian character. This means that once the theory is renormalized, the coupling $\alpha_s = g_R^2/(4\pi)$ becomes a function of a scale μ (the renormalization scale) with the property $g_R(\mu \to \infty) \to 0$. The function that governs this running is called the beta function which was firstly calculated in [26] yielding a negative leading coefficient. In this sense, perturbation theory holds only at very high energies, where the coupling is small. Unfortunately, at small energies, the renormalized coupling constant is $\mathcal{O}(1)$ and there is no hope of computing analytically any observable relying on perturbative expansions. From a theoretical point of view, this feature makes QCD a well behaved theory eliminating the Landau singularity present for example in QED spoiling the convergence of perturbative expansions at high energies. Nevertheless, at small energies where confinement occurs, Lattice Gauge Theory or effective theories with experimental input are the only tools at our disposal to gain information of the hadronic processes.

3.2 $SU(3)$ **gauge symmetry**

Obviously Eq. (3.1.1) describes a gauge invariant Lagrangian. To show this one has to specify the gauge transformations for the different fields:

$$\psi(x) \;\mapsto\; \psi'(x) = U_{\mathcal{F}}[g(x)]\psi(x), \qquad \bar{\psi}(x) \mapsto \bar{\psi}'(x) = \bar{\psi}(x)U_{\mathcal{F}}^{\dagger}[g(x)],$$

$$A_{\mu} \;\mapsto\; A'_{\mu} = U_{\mathcal{A}}[g(x)]A_{\mu}U_{\mathcal{A}}^{\dagger}[g(x)] + i(\partial_{\mu}U_{\mathcal{A}}[g(x)])U_{\mathcal{A}}^{\dagger}[g(x)]. \qquad (3.2.1)$$

Given the above transformations

$$F_{\mu\nu} \;\mapsto\; F'_{\mu\nu} = U_{\mathcal{A}}[g(x)]F_{\mu\nu}U_{\mathcal{A}}^{\dagger}[g(x)] \qquad (3.2.2)$$

where the subscripts $\mathcal{F}$ and $\mathcal{A}$ stand for the fundamental and adjoint representation respectively.

Some additional remarks on gauge symmetry can be made. For this purpose let us use a more simple gauge theory like quantum electrodynamics which is abelian. Gauge symmetry stems from a global symmetry: the empirical observation that electrons and positrons, having the same mass, couple with the same strength to the presence of an electromagnetic field. Nevertheless, why is there a need to promote this symmetry to a local one? The problem arises when trying to quantize the theory with say, the path integral formalism presented in Sec. 2.1. Once we have defined the electromagnetic current to be proportional to the Noether current (Noether currents always follow from global symmetries), it turns out that if the spinor fields do not satisfy the classical equations of motion, the electromagnetic current $j_{\mu}(x) = e\bar{\psi}(x)\gamma_{\mu}\psi(x)$ is no longer conserved at the quantum level. This would imply that the quantum system would be able to generate or annihilate net electric charge which is in clear contradiction with experiments. The way out relies on the definition of a gauge transformation which is local and depends on the space-time point x^{μ}. In this way the electromagnetic current is *always* conserved even if the classical equations of motion are violated (due to quantum fluctuations). A very interesting discussion on this topic can be found in [27] Chap. 58. For the case of non-abelian theories like QCD, additional problems arise with quantization. The inclusion of the Faddeev-Popov determinant which gives rise to the well known ghost fields are mandatory for keeping an $SU(3)$ gauge symmetry.

Nevertheless, this is beyond the scope of this work and, as we will see, in the Lattice formulation of gauge theories, this is in general unnecessary.

	up (u)	down (d)	strange (s)	charm (c)	bottom (b)	top (t)
Q	2/3	-1/3	-1/3	2/3	-1/3	2/3
mass	2.3 MeV	4.8 MeV	95 MeV	1.3 GeV	4.2 GeV	173.2 GeV

Table 3.1: Matter content of QCD. Quark masses are quoted in the $\overline{\text{MS}}$ scheme at a scale $\mu = 2\text{GeV}$ [28].

3.3   Chiral Symmetry

Chiral symmetry is of fundamental importance to understand, among other puzzles, the low-lying hadron spectrum of QCD. From Table 3.1 it can be seen that quark masses can be divided into a light and a heavy sector with the strange quark being neither light nor heavy. If interested in physics at the hadronic scale, ($\mu \lesssim 1\text{GeV}$) we can, in first approximation, consider two-flavor QCD where only up and down quarks are taken into account and the remaining degrees of freedom are "frozen" (or "integrated out") meaning that they are decoupled from the relevant physics scale. Moreover, we can send both light quark masses to zero $m_u = m_d \to 0$ and the Lagrangian exhibits a new set of global symmetries: mainly $U(2)_R \times U(2)_L \sim U(1)_V \times SU(2)_V \times SU(2)_A \times U(1)_A$ where the subscripts R, L, V, A refer to right, left, vector and axial (the precise definition of the symmetry transformation is found in Sec. 3.3.2.) This is the so-called chiral limit. The $U(1)_A$ group is broken due to quantum fluctuations and one refers to it as the chiral anomaly. It was first investigated in [29, 30] in the context of $\pi^0 \to \gamma\gamma$ decays.

3.3.1   Spontaneous symmetry breaking: $N_f = 2$

Given the above symmetry pattern one would naively expect that hadrons organize themselves into approximately degenerate multiplets fitting dimensionalities of irreducible representations of $SU(2)_L \times SU(2)_R \times U(1)_V$. The $U(1)_V$ group can be associated to baryon number. This means one can separate hadrons into baryons ($B = 1$) and mesons ($B = 0$). Since vector and axial charges have a

well defined behavior under the parity operation one expects to find particles fitting into multiplets with even and odd parity respectively. Nevertheless, it is an experimental fact that this parity doubling is not realized in nature.

Consequently, $SU(2)_L \times SU(2)_R$ cannot be a true symmetry of the vacuum (even if $m_u = m_d = 0$). In addition, we see that vector symmetry is indeed realized in nature since the pions can be arranged into an $SU(2)$ triplet with approximately degenerate masses (π^+, π^0, π^-) due to the fact that the mass matrix is diagonal and the flavor vector current is conserved. This limit is referred to as isospin limit. Apart from that, we see that pions have masses well below the typical confining scale of QCD (~ 1 GeV). It seems very unnatural that there is a huge mass gap between the lightest hadrons and the proton for example. Thus, one concludes that in order to explain the masses of pions, one must find a special theoretical framework that can be used to make sense out of such discrepancies. This pattern is Spontaneous Symmetry Breaking (SSB). Goldstone's Theorem, which is the main result of SSB [31, 32], can be invoked to explain the existence of a priori massless Goldstone Bosons (the pions) carrying axial quantum numbers and equally important, the absence of its parity doublers. To each generator that does not annihilate the vacuum there corresponds a massless spin 0 field, whose symmetry properties are tightly connected to the generator in question. One often says that the chiral group $SU(2)_L \times SU(2)_R$ is spontaneously broken to $SU(2)_V$. Nevertheless, we know that the real world Lagrangian of Eq. (3.1.1) explicitly breaks chiral symmetry due to non-vanishing quark masses. Once the symmetry is explicitly broken, one expects massive Goldstone bosons whose squared masses are, according to general theorems on soft symmetry breaking [32], proportional to the symmetry breaking parameters which are precisely the quark masses. It is important to point out that the existence of pseudoscalar degrees of freedom (massless or not) does not rely on the precise value of the quark masses but on the fact that some axial generators do not annihilate the vacuum state. One can apply the machinery of a spontaneously broken theory which leads then to the low energy hadron phenomenology we observe and the empirical fact of the existence of pseudo Goldstone bosons. A very detailed description of SSB can be found in [33] Sec. 3.

3.3.2   The chiral condensate as an order parameter of SSB

As stated in the previous section, the SSB pattern that governs chiral symmetry breaking can be written as $SU(2)_V \times SU(2)_A \to SU(2)_V$ (omitting the $U(1)'s$). Any system that exhibits a SSB pattern is suitable for the definition of an order parameter such that its expectation value is non-zero in the broken phase and zero in the symmetric phase. In QCD with two flavors of light quarks this role is played by the chiral condensate

$$\langle \bar{q}q \rangle = \left\langle \bar{\psi}^u \psi^u + \bar{\psi}^d \psi^d \right\rangle \neq 0 \qquad \text{if } T < T_C. \tag{3.3.1}$$

A general $SU(2)_V$ or $SU(2)_A$ transformation acts on the fields as follows

$$\psi \mapsto \psi' = e^{i\alpha_V^a \tau^a}\psi, \qquad \bar{\psi} \mapsto \bar{\psi}' = \bar{\psi}e^{-i\alpha_V^a \tau^a}, \tag{3.3.2}$$

$$\psi \mapsto \psi' = e^{i\alpha_A^a \gamma_5 \tau^a}\psi, \qquad \bar{\psi} \mapsto \bar{\psi}' = \bar{\psi}e^{i\alpha_A^a \gamma_5 \tau^a}. \tag{3.3.3}$$

where $a = 1, 2, 3$ and τ^a are the Pauli matrices which are the generators of the $SU(2)$ group. Given the above transformations it can be easily seen that the chiral condensate is invariant under $SU(2)_V$ but not under a chiral rotation. Therefore, it is a perfect candidate for an order parameter. The expectation is that at high temperatures, the value of the chiral condensate is zero and the full symmetry is restored. It is not clear yet, what the role of the axial anomaly near the phase transition is. We will further comment on the finite temperature aspects of chiral symmetry in Chapter 6.

3.3.3   Chiral Perturbation Theory

Chiral Perturbation theory (ChPT) is the effective theory of QCD at low-energies. The concept of an effective theory is usually well explained in the context of the Theory of Fermi interaction [34]. Way before the experimental discovery of the charged electroweak gauge bosons in 1983 at CERN, Feynman and Gell-Mann wrote down a Lagrangian density with a 4-fermion interaction term, which successfully described electroweak processes at small energies. Nonetheless, this new operator made the theory non-renormalizable and therefore lacking an UV-completion. A theory which is only valid in a specific range of energies is often called an effective theory. As opposed to Fermi's theory, ChPT is formulated in terms of completely

new degrees of freedom, namely mesons and baryons. We will stick to the case of mesons in $N_f = 2$ and therefore only pions are taken into account. They are described by fields $\phi^a(x)$ which are scalars under the Lorentz group. The most important constraint on the effective Lagrangian density comes from QCD vacuum symmetries. The pion fields are collected in a hermitian traceless matrix. After exponentiation the resulting matrix is a member of the $SU(2)$ group. This way of collecting the effective degrees of freedom is often referred to as the non-linear sigma model

$$\phi(x) = \sum_{a=1}^{3} \tau^a \phi^a(x) = \begin{pmatrix} \phi_3 & \phi_1 - i\phi_2 \\ \phi_1 + i\phi_2 & -\phi_3 \end{pmatrix} = \begin{pmatrix} \pi^0 & \sqrt{2}\pi^+ \\ \sqrt{2}\pi^- & -\pi^0 \end{pmatrix}. \tag{3.3.4}$$

The exponential map yields then

$$U(x) = \exp\left(i\frac{\phi(x)}{F_0}\right) \tag{3.3.5}$$

where F_0 is the pion decay constant in the chiral limit. It is one of the many low-energy constants that encodes the effects of the underlying theory which is QCD. A general left, right transformation acts on $U(x)$ as

$$U(x) \mapsto RU(x)L^\dagger, \tag{3.3.6}$$

where R and L are group elements of $SU(2)_R$ and $SU(2)_L$ respectively. The most general chirally invariant lagrangian density with the minimal number of derivatives for $N_f = 2$ reads

$$\mathcal{L} = \frac{F_0^2}{4} \text{Tr}\left\{\partial_\mu U \partial_\mu U^\dagger\right\}. \tag{3.3.7}$$

Finally, since we are interested in predictions regarding an expansion in the small light quark masses we can introduce a mass matrix proportional to a new low-energy constant Σ_0. It is the chiral-condensate in the chiral limit. The full lowest-order ($\mathcal{O}(p^2)$) ChPT Lagrangian then reads

$$\mathcal{L}_{LO} = \frac{F_0^2}{4} \text{Tr}\left\{\partial_\mu U \partial_\mu U^\dagger\right\} + \frac{F_0^2 \Sigma_0}{2} \text{Tr}\left\{MU^\dagger + UM^\dagger\right\}, \tag{3.3.8}$$

where

$$M = \begin{pmatrix} m_u & 0 \\ 0 & m_d \end{pmatrix}.$$ (3.3.9)

When calculating loop corrections, one notices that divergences which cannot be absorbed in a redefinition of the bare parameters F_0 and Σ_0 appear. This makes the theory unrenormalizable. Nevertheless, a power counting was defined by Weinberg [35] such that to a given order in the momentum expansion, the theory is still well behaved.

In the context of Lattice QCD, ChPT is usually used to extrapolate observables to the physical values of the quark masses. ChPT at finite temperature is also interesting, since the thermal modifications of various chiral observables can be defined as shown in Appendix G.

Chapter 4

Lattice Gauge Theory

Lattice Gauge Theory (LGT) is a framework based on Quantum Field Theory formulated in a finite and discrete space-time grid. The basic ideas were first introduced by Kenneth Wilson in 1974 in the celebrated paper (*Confinement of Quarks* [36]) where he laid the foundations of Lattice Gauge Theories. He was awarded the 1982 Nobel Prize in Physics for his novel understanding of Renormalization in Quantum Field Theories and the application to critical phenomena. The space-time discretization has several virtues. Firstly, the lattice regularization preserves gauge invariance exactly at finite lattice spacing. Secondly, field configurations are given in terms of compact variables which avoids the gauge fixing procedure. Still, LGT enables a non-perturbative definition of gauge theories like QCD. Finally, given that the number of degrees of freedom becomes finite, the lattice formulation is suitable for numerical simulations based on Monte Carlo methods given that the action can be rewritten as a positive definite functional form of the fields. The first numerical studies were performed by M. Creutz in [37, 38]. The crucial point is to recognize that no perturbative expansions are needed as opposed to the continuum formulation. Up to systematic errors called lattice artifacts, lattice results within QCD are valid to any order in perturbation theory and when continuum extrapolated represent the *"numerical realization of QCD"* (F. Wilczek).

4.1   Basic concepts of Lattice QCD

The central idea consists in replacing the continuum 4D space-time by a grid whose points are separated by a distance a called lattice spacing

$$\Lambda = \left\{ x \in \mathbb{R}^4 | x_\mu = a n_\mu; n_i = 0, ..., N_S - 1; n_0 = 0, ..., N_\tau - 1 \right\}. \qquad (4.1.1)$$

As it is demanded by the statistical interpretation of the path integral, we work with euclidean metric which for the case of QCD at vanishing chemical potential makes the action positive definite. This is not only important for implementing finite temperature as it has been shown in previous sections but also is of crucial importance for the generation of configurations.

The value of a in physical units is deduced a posteriori in a process called scale setting. For simplicity a is chosen to be equal in time and spatial directions. The opposite situation is called an anisotropic lattice which can be very useful in some particular situations but here, we will only work with isotropic lattices. The physical extent of our box is then a function of the lattice spacing. So is temperature, which as mentioned in the previous discussion, is related to the inverse of the imaginary-time extent

$$L \;=\; N_S a \qquad (4.1.2)$$

$$T \;=\; \frac{1}{N_\tau a}. \qquad (4.1.3)$$

The aspect ratio LT is independent of the lattice spacing and is a very natural object to estimate finite-volume effects with. It should be clear that in order to obtain results that are valid in the continuum we have to send $a \to 0$. Nevertheless, by doing so, we also are shrinking the box to zero. So one has to increase the number of points in both directions so as to keep the physical values of L and T fixed. This, of course, is very demanding from the computational point of view. The whole process can be repeated for different values of L with the hope of extrapolating our results to the thermodynamic limit at infinite L and finite T.

The practical way of proceeding can be summarized in three steps:

- First, one needs to find a discretized version of the action of the theory under study in euclidean metric. In our case we will discretize the continuum QCD lagrangian density of Eq. (3.1.1). During this process one encounters prob-

lems like the appearance of unwanted doublers, loss of chiral symmetry (even at vanishing quark masses) or discretization effects that can dramatically affect our results. It is important to note that there is a large set of actions that can reproduce the QCD action when the lattice spacing is sent to zero. We can use this ambiguity to our advantage to define different Lattice QCD actions with different properties that are better suited for a large variety of problems. We will address some of this issues in the upcoming sections.

- Expectation values of operators are calculated in the standard way

$$\langle \mathcal{O} \rangle = \frac{1}{Z} \int \mathcal{D}\{\phi\} \; \mathcal{O}(\{\phi\}) e^{-S_{QCD}^{\text{lat}}[\phi]}. \tag{4.1.4}$$

where $Z = \int \mathcal{D}\{\phi\} e^{-S_{QCD}^{\text{lat}}[\phi]}$, $\{\phi\}$ are intended to be the set of fields that enter the action and thus, describe the different degrees of freedom present in our simulation and $S_{QCD}^{\text{lat}}[\phi]$ is our particular lattice choice for the QCD action. In continuum QCD $\{\phi\} = \{\bar{\psi}, \psi, A_\mu\}$ but it is not guaranteed that the same parametrization is useful in Lattice actions as we will see. In any case, we will require that

$$\lim_{a \to 0} S_{QCD}^{\text{lat}}[\phi] = S_{QCD}[\bar{\psi}, \psi, A_\mu]. \tag{4.1.5}$$

Valid actions exist which do not have a continuum limit nor perturbation theory is well defined. They fall under the category of topological actions [39] and are constructed in a way that the right symmetries are respected and the quantum limit is reached at finite lattice spacing which is well used in the context of, for example, spin models. Since LGT is intended to be a first principles approach, one can think of several ways of evaluating the expectation value of some observable following Eq. (4.1.4). Let us define a set of random configurations $\Gamma_{\text{R}}(\{\phi\})$. Formally, one can then write

$$\langle \mathcal{O} \rangle = \frac{\sum_{\{\phi\} \in \Gamma_R} \mathcal{O}(\{\phi\}) e^{-S_{QCD}^{\text{lat}}[\phi]}}{\sum_{\{\phi\} \in \Gamma_{\text{R}}} e^{-S_{QCD}^{\text{lat}}[\phi]}}. \tag{4.1.6}$$

Nevertheless, this is not very efficient because the majority of configurations will yield a very big value of the action and therefore will contribute very little to the expectation value of the observable under consideration. Instead,

one uses a much more intelligent approach called importance sampling where one first generates a set of N configurations $\Gamma_{\text{MC}}(\{\phi\})$ which are precisely distributed according to the probability distribution density

$$dP(\{\phi\}) = \frac{e^{-S_{QCD}^{\text{lat}}[\phi]}\, \mathcal{D}\{\phi\}}{\int \mathcal{D}\{\phi\}\, e^{-S_{QCD}^{\text{lat}}[\phi]}}. \qquad (4.1.7)$$

In this way we can write Eq. (4.1.4) as

$$\langle \mathcal{O} \rangle = \lim_{N \to \infty} \frac{1}{N} \sum_{\{\phi\} \in \Gamma_{\text{MC}}} \mathcal{O}(\{\phi\}). \qquad (4.1.8)$$

Now it should be clear why it is so important that the action is positive definite acting like a Boltzmann factor. Otherwise the process of importance sampling cannot be pursued. The set of configurations $\Gamma_{\text{MC}}(\{\phi\})$ is generated via Montecarlo methods which we will discuss in some extent in Sec. 4.7. Apart from sampling correctly the space of configurations, taking only those that contribute most to the expectation value of any observable, this set of configurations is universal (for a given set of bare parameters) and can of course be reused for other observables.

- Finally, in order to compare with experimental results, the continuum limit needs to be taken. There is no general recipe to extrapolate a certain quantity to the continuum since it depends on how the calculation on the Lattice side took place and what quantity we are considering. Nevertheless, some general remarks can be made here. The parameters m and the coupling g are initially bare parameters that a priori have no meaning at all. In order to extract physics from our Lattice QCD action, we need to relate those parameters to physical observables which in practice means that one has to give up the measurement of some physical quantity that serves to set the overall scale (extract a in physical units). Different choices of the scale setting observable will lead to different results at finite lattice spacing. Nevertheless when the continuum limit is taken, they should agree. It then becomes obvious that the bare parameters have to depend nontrivially on the cutoff scale a in order to keep the physics constant as we move towards $a \to 0$ where the lattice

spacing dependence cancels out completely. This corresponds to the process of renormalizing the theory and will be adressed in Sec. 4.5.

4.1.1   The lattice spacing as a regulator

The lattice spacing a will play an outstanding role in the formulation of LGT. Recalling the situation in continuum QFT, we know that momentum integrals that arise due to quantum contributions in loop diagrams are in general divergent. The problem is solved by regulating the theory with the inclusion of some additional external parameter like a hard cutoff Λ (Pauli-Villars regularization) such that the integral is carried out up to the cutoff making the result finite, but cutoff dependent. Dimensional regularization is a commonly used regularization procedure as well. It appears as a consequence of the fact that the scaling of those integrals to infinity is different for different values of the space-time dimension d. In some cases of theories of low dimensionality, the integrals are even convergent. For example it is the case for QED in 1+1 dimensions which is a superrenormalizable theory. By doing the replacement $d = 4 - \epsilon$, one can move away from the divergent situation and isolate the infinite part. This non-analytic contribution is then included in the bare parameters of the initial Lagrangian (if the theory is renormalizable) such that it exactly cancels the infinities arising in momentum integrals. In a second step, one has to be sure that physical observables, which can be measured experimentally, cannot depend on the value of the scale where the infinite subtraction took place. In the continuum, this is done by solving the renormalization group invariant differential equations called Callan-Symanzik equations that lead to the well known Renormalization Group Invariant (RGI) quantities.

By contrast in LGT, the regulating parameter is automatically the lattice spacing a. Due to space-time discretization, momentum integrals are forced to live in the first Brillouin zone such that the maximum value is $\mathbf{p} = \pi/a(1,1,1)$. This ensures that all results calculated within the lattice formulation are finite. This very particular scale of order $\sim 1/a$ can be seen as the hard cutoff scale of the theory. Lattice results can only be compared to physically observable quantities if they are renormalized and continuum extrapolated. This refers to the process of eliminating the cutoff dependence and is achieved by repeating the calculation at even finer lattices until a safe extrapolation can be carried out. The Wilsonian approach to renormalization is specially relevant and intuitive in LGT. One can

imagine that the discretized version of some continuum action is nothing but the effective action of the continuum theory where the modes that range from $\sim 1/a$ to infinity are integrated out.

4.2   Pure Yang-Mills Theory on the Lattice

Pure Yang-Mills theory on the lattice is the main building block of any discretized gauge theory and QCD is no exception. Moreover, a substantial part of this thesis deals with some particular aspects of renormalization of pure $SU(3)$ Yang-Mills theory (see Chapter 5). Therefore we find it interesting to formally introduce its action. The gluonic contribution to the QCD action is given in the continuum by the following kinetic term

$$S_G^{\text{cont}} = \frac{1}{2g^2} \int d^4x \, \text{Tr}[F_{\mu\nu}F_{\mu\nu}]. \tag{4.2.1}$$

A discretized version has to be found for the lattice case. The usual way of introducing link variables which are meant to reproduce the dynamical gluon background is to note that the naive discretized version of the fermionic action (which we will treat in detail in the next section) is not gauge invariant unless a so called gauge transporter is introduced. The well known Dirac action for a single massive fermion is written as follows

$$S_F^{\text{cont}}[\psi, \bar{\psi}] = \int d^4x \, \bar{\psi}(x)(\gamma_\mu \partial_\mu + m)\psi(x). \tag{4.2.2}$$

Since on the lattice the fermion fields live at discrete values of space-time we have to use finite-difference derivatives such as

$$\partial_\mu \psi(x) \to \frac{1}{a}(\psi(n+\hat{\mu}) - \psi(n)) + \mathcal{O}(a) \tag{4.2.3}$$

where $\hat{\mu}$ is a unit vector pointing in the μ-direction. In practice, one uses a more complicated form of the derivative that removes higher order terms in a, but for the discussion now, this is sufficient. This form of the derivative will give us terms that are products of two field living at different nearby positions $\bar{\psi}(n)\psi(n+\hat{\mu})$. When gauge transforming these terms as given by Eq. (3.2.1) we note that they are not gauge invariant. The way out relies on the definition of a link variable that

lives between the two points and transform as

$$U_\mu(n) \rightarrow g(n)U_\mu(n)g^\dagger(n+\hat{\mu}) \tag{4.2.4}$$

where $g(n)$ represents some group element of $SU(3)$ depending on the space-time point n. Consequently, a term written as $\bar{\psi}(n)U_\mu(n)\psi(n+\hat{\mu})$ is now gauge invariant. In order to make the connection to the continuum theory one notes that the transformation rule of $U_\mu(n)$ is precisely the same as the one of a gauge transporter. Namely,

$$G(x,y) = P\exp\left(i\int_{\Gamma(x,y)} A\cdot ds\right) \rightarrow g(x)G(x,y)g^\dagger(y) \tag{4.2.5}$$

where P stands for the path-ordered operator, $\Gamma(x,y)$ is some curve that connects both points x and y and A is intended to be the gauge connection or gauge field $A_\mu(x)$ that encodes all information about the gauge manifold. So in order that two fields at different points "can talk to each other in a gauge invariant way" they have to be gauge transported to the same point via the gauge transporter. The key observation is that we can write our link variable as an expansion of the continuum gauge field $A_\mu(n)$ which is true up to lattice effects

$$U_\mu(n) = \exp(iaA_\mu(n)) = G(n,n+\hat{\mu}) + \mathcal{O}(a) = 1 + iaA_\mu(n) + \mathcal{O}(a^2). \tag{4.2.6}$$

Having identified the link variables $U_\mu(n)$ as only building blocks of our gauge theory that encode gauge degrees of freedom, we need to write a gauge invariant action such that when $a \rightarrow 0$ we recover the $SU(3)$ Yang-Mills continuum action

$$S_G^{\text{cont}} = \lim_{a\to 0} S_G. \tag{4.2.7}$$

The simplest gauge invariant action that one can write only in terms of link variables is the so called Wilson gauge action or plaquette action which reads

$$S_G^W[U] = \frac{\beta_L}{3}\sum_{n\in\Lambda}\sum_{\mu<\nu}\text{ReTr}[1 - U_{\mu\nu}] \tag{4.2.8}$$

where

$$U_{\mu\nu} = U_\mu(n)U_\nu(n+\hat{\mu})U_{-\mu}(n+\hat{\mu}+\hat{\nu})U_{-\nu}(n+\hat{\nu}) \tag{4.2.9}$$

is called the plaquette (see Fig. 4.1) and $\beta_L = 6/g^2$ is called inverse coupling which is a commonly used definition in the lattice community (not to be confused with β which is the physical imaginary time extent equal to $N_\tau a = 1/T$). All closed loops of link variables are gauge invariant objects being the plaquette the most simple one. It corresponds to the smallest orientable closed loop in the (μ, ν) plane. The links satisfy the property $U_{-\mu}(n) = U_\mu^\dagger(n - \hat{\mu})$. Taking the real part of the plaquette ensures that both orientations are taken into account since $\mathrm{Re}[U_{\mu\nu}] = \frac{1}{2}(U_{\mu\nu} + U_{\mu\nu}^\dagger)$ and $U_{\mu\nu}^\dagger = U_{\nu\mu}$.
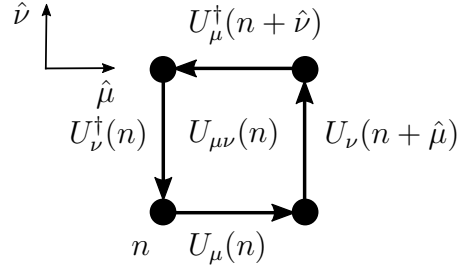
Figure 4.1: Plaquette $U_{\mu\nu}(n)$.

It can be easily proven by using the Taylor expansion of U_μ together with the Baker-Campbell-Hausdorff formula that

$$S_G^W[U] = \frac{\beta_L}{3} \sum_{n \in \Lambda} \sum_{\mu < \nu} \mathrm{Re}\mathrm{Tr}[1 - U_{\mu\nu}] = \frac{a^4}{2g^2} \sum_{n \in \Lambda} \mathrm{Tr}[F_{\mu\nu}]^2 + \mathcal{O}(a^2) \qquad (4.2.10)$$

and the continuum limit is recovered. Note that in the Lattice formulation of Yang-Mills theory, gauge degrees of freedom are group elements of $SU(3)$. Mainly 3×3 unitary matrices of unit determinant carrying color indices of the adjoint representation. This is conceptually different from the continuum, where the gauge field is a member of the algebra of the $SU(3)$ group, 3×3 hermitian traceless matrices satisfying ordinary Lie algebra commutation relations. One of the consequences is that the gauge-fixing procedure which is mandatory in the continuum, is for general purposes not needed on the lattice. The reason behind it is that $SU(N)$ gauge groups are compact such that an integration measure can be defined over the whole group making it possible to define a finite integral over the gauge links that

covers all possible link field configurations. This avoids the problem of choosing a privileged gauge trajectory such that gauge equivalent field configurations are not double counted. In the continuum, this leads to the inclusion of the Faddeev-Popov determinant.

4.3 Including fermions: the Wilson action

We conclude the discussion of the previous section with the inclusion of fermionic degrees of freedom. For this purpose it is useful to start with some discretization of the Dirac operator. Using a symmetrized version of the lattice derivative $\partial_\mu \psi \sim \frac{1}{2a}(\psi(n+\hat{\mu}) - \psi(n-\hat{\mu}))$ that removes $\mathcal{O}(a)$ effects one can write

$$S_F[\bar{\psi}, \psi, U] = a^4 \sum_{n \in \Lambda} \bar{\psi}(n) \left(\sum_\mu \gamma_\mu \frac{U_\mu(n)\psi(n+\hat{\mu}) - U_{-\mu}(n)\psi(n-\hat{\mu})}{2a} + m\psi(n) \right)$$
(4.3.1)

where appropriate link variables have been introduced to preserve gauge invariance. This is analogous to the minimal coupling procedure that is used in defining covariant derivatives in gauged theories. In order to define the free propagator of a single quark of mass m we have to invert the Dirac operator in momentum space with all links put equal to the identity matrix (this corresponds to the free theory). The solution reads

$$D(p) = m + \frac{i}{a} \sum_\mu \gamma_\mu \sin(p_\mu a) \tag{4.3.2}$$

$$D(p)^{-1} = \frac{m - ia^{-1} \sum_\mu \gamma_\mu \sin(p_\mu a)}{m^2 + a^{-2} \sum_\mu \sin(p_\mu a)^2} \tag{4.3.3}$$

It turns out that this form of the propagator yields 16 poles in the first Brillouin zone whereas only one of them is physical. This is known as the doubling problem. To get rid of it, Wilson proposed the addition of an extra term to the Dirac operator that vanishes linearly in the continuum limit and gives a very heavy mass to the doublers such that they decouple when the continuum limit is taken. This is the so-called Wilson term that we subtract from the naive action

$$S_F^W = S_F - \frac{r}{2}a^5 \sum_{n \in \Lambda} \bar{\psi}(n)\Box\psi(n) \tag{4.3.4}$$

where $\bar{\psi}(n)\Box\psi(m) = \sum_\mu \bar{\psi}(n)\frac{U_\mu(n)\psi(n+\hat{\mu})-2\psi(n)+U_{-\mu}(n)\psi(n-\hat{\mu})}{2a^2}$ is the naive discretized laplacian operator with appropriate links included for gauge invariance and r is the Wilson parameter that is commonly set to unity. With this term added we can recompute the inverse of the Dirac operator and we encounter that the masses of the fermions are shifted according to their momenta

$$m \to m(p) = m + \frac{2r}{a} \sum_\mu \sin(p_\mu a/2). \tag{4.3.5}$$

This ensures that as we take the naive continuum limit $a \to 0$ only the physical fermion survives while the doublers that live at the edges of the first Brillouin zone get an infinite mass and decouple. The full Wilson action for one fermion of mass m including the Wilson term then reads

$$S_F^W[\bar{\psi},\psi,U] = a^4 \sum_{n\in\Lambda} \bar{\psi}(n) \left(m + \frac{4}{a} \right) \psi(n) - \frac{1}{2a} \sum_{\mu=\pm\mu} \bar{\psi}(n)(1 - \gamma_\mu)U_\mu(n)\psi(n + \hat{\mu}) \tag{4.3.6}$$

where we have defined $\gamma_{-\mu} = -\gamma_\mu$. The drawback of this action is that we have explicitly broken chiral symmetry, even when $m = 0$ such that $\{D_W,\gamma_5\} \neq 0$. This introduces several problems when renormalizing the bare quark masses since it does not renormalize multiplicatively anymore. Instead, an additive renormalization parameter appears since there is no symmetry protecting from a mixing with the unit operator which has the same quantum numbers as the mass term

$$\overline{m} = Z_m(m - m_c) \tag{4.3.7}$$

where m_c is called the critical mass and Z_m is the renormalization constant that needs to be determined non-perturbatively. In practical simulations one makes use of a different parametrization for choosing the bare masses. Since the Wilson Dirac operator has to be inverted in order to calculate n-point functions it is useful to introduce the hopping expansion which reads

$$D_W = 1 - \kappa H, \qquad \kappa = \frac{1}{2am + 8} \tag{4.3.8}$$

where κ is the hopping parameter. In this way we can write for the inverse

$$D_W^{-1} = (1 - \kappa H)^{-1} = \sum_{n=0} \kappa^n H^n. \qquad (4.3.9)$$

It is a common practice that Lattice theorists use κ instead of m for referring to the bare quark mass following Eq. (4.3.8). For the renormalized quark mass, one first needs a precise definition such as the one written in Eq. (4.3.7). Nevertheless, there are other equally good options like e.g. the PCAC mass which will be introduced in Sec. 4.5.1.

4.4   Lattice artifacts

One can group systematic errors present in lattice calculations into three categories:

- Finite volume effects: They arise due to the finite extent of our 4D box. It is an infrared effect present at low energies. One often uses the value of the pion mass $m_\pi L$, (more precisely, the screening pion mass) to quantify them. Since finite volume effects are exponential $\sim e^{-m_\pi L}$, as a rule of thumb, if $m_\pi L > 4$ one is in the "safe regime", which means that finite volume effects may be small and under control. Ideally, one should always perform a finite volume study at bigger lattices in order to quantify finite volume corrections.

- Cutoff effects: The most important systematic errors come from the finite lattice spacing a we are forced to use in lattice calculations. It is an ultraviolet effect at energy scales $\mu \sim 1/a$. As stated in previous sections, the lattice spacing acts as a natural regulator of LGT since no momentum can be induced bigger than $\sim \pi/a$. In the far future, when computers are so powerful to perform simulations at sufficiently small values of a, cutoff effects may become numerically negligible. Until then, one needs to find a way to deal with them and in the best case to remove them completely. This will be the topic of the next section.

- Chiral extrapolation to physical quark masses: In many Lattice simulations the values of the renormalized quark masses are not the ones realized in nature. This leads to systematic errors in quantities that depend strongly with

the quark masses. A typical example is the pion mass m_π^2 which according to Chiral Perturbation Theory grows linearly with the quark mass. Simulations are often done at much heavier pion masses than the ~ 140 MeV value listed in the PDG. Two main reasons speak in favor of simulating at bigger pion masses. Firstly, finite size effects are suppressed with the lightest screening mass of the theory. Choosing a bigger value of the pion mass leads to smaller finite size effects. From the numerical point of view, the Wilson Dirac operator defined in the previous section needs to be inverted for the calculation of any observable within LGT. It turns out, the smaller one chooses the value of the masses, the bigger the condition number of D_W is. This leads to a higher computational cost in the calculation of its inverse. The extrapolation to the physical pion mass is done a posteriori with theoretical input from ChPT.

4.4.1   Improvement program

From the discussion on the discretized version of the pure gauge action we saw that the standard plaquette-Wilson action reproduces the continuum Yang-Mills action up to $\mathcal{O}(a^2)$ effects. It can be shown that pure gauge lattice actions are always $\mathcal{O}(a)$ improved. This is not true when introducing fermions. The main reason is the inclusion of the Wilson term, mandatory to remove doublers. As it can be seen from Eq. (4.3.4) it is a dimension 5 operator that vanishes linearly with the lattice spacing. Thus, our Wilson fermion action has $\mathcal{O}(a)$ effects. These discretization errors will propagate to any expectation value of any observable calculated on configurations generated with this action. Nevertheless, we can use to our advantage the freedom of adding other operators of dimension bigger than 4 that also vanish in the continuum limit and hence, reproduce the QCD action. When tuning the coefficients of those new operators, we may be able to exactly cancel discretization effects order by order. This is the philosophy behind the Symanzik improvement program [40, 41] we will try to summarize here.

Let us write an effective lattice action as an expansion in the lattice spacing a

$$S^{lat} = \int d^4x \left(L^{(0)} + aL^{(1)} + a^2 L^{(2)} + ... \right) \tag{4.4.1}$$

where $L^{(0)}$ is simply the continuum QCD lagrangian written in Eq. (3.1.1). The new terms $L^{(k)}$ have dimensions $4 + k$ and hence they are multiplied with a^k such

that the full action is dimensionless (in natural units). All new terms that appear as $k > 0$ have to respect all relevant QCD symmetries (gauge invariance, Lorentz covariance). For $k = 1$ we can write 5 different dimension 5 operators. Making use of the Dirac field equation we see that only 3 are linearly independent. Those are

$$L_1^{(1)} = \bar{\psi}(x)\sigma_{\mu\nu}F_{\mu\nu}\psi(x) \tag{4.4.2}$$

$$L_2^{(1)} = m\mathrm{Tr}[F_{\mu\nu}F_{\mu\nu}] \tag{4.4.3}$$

$$L_3^{(1)} = m^2\bar{\psi}(x)\psi(x) \tag{4.4.4}$$

where $\sigma_{\mu\nu} = \frac{i}{2}[\gamma_\mu, \gamma_\nu]$ are the generators of the Lorentz group. We notice that $L_2^{(1)}$ and $L_3^{(1)}$ are operators that are already included in our fermion Wilson action of Eq. (4.3.6). A redefinition of the bare parameters m and g would absorb those terms. We are left with $L_1^{(1)}$ which is called the Sheikholeslami-Wohlert term or clover term [42]. The $\mathcal{O}(a)$ improved Wilson action can then be written as

$$S_F^{W,\mathrm{imp}}[\bar{\psi}, \psi, U] = S_F^W[\bar{\psi}, \psi, U] + c_{\mathrm{sw}}a^5\sum_{n\in\Lambda}\sum_{\mu<\nu}\bar{\psi}\frac{1}{2}\sigma_{\mu\nu}\hat{F}_{\mu\nu}(n)\psi(n) \tag{4.4.5}$$

where c_{sw} is the coefficient we have to tune in order to properly remove $\mathcal{O}(a)$ discretization effects. The object $\hat{F}_{\mu\nu}$ is some discretized version of the field-strength tensor. One can show that the following operator is suitable

$$\hat{F}_{\mu\nu} = \frac{-i}{8a^2}(Q_{\mu\nu} - Q_{\nu\mu}) = F_{\mu\nu} + \mathcal{O}(a^2) \tag{4.4.6}$$

where $Q_{\mu\nu}(n)$ is the sum of plaquettes in the (μ, ν) plane at point n (see Fig. 4.2).

$$Q_{\mu\nu}(n) = U_{\mu,\nu}(n) + U_{-\mu,\nu}(n) + U_{\mu,-\nu}(n) + U_{-\mu,-\nu}(n) \tag{4.4.7}$$

and $U_{\mu,\nu}(n)$ is the plaquette at point n as defined in Eq. (4.2.9) with the property $U_{\mu,\nu}(n) = U_{-\mu,\nu}(n + \hat{\mu})$ (equivalently for ν). Since Q is a sum of plaquettes, $Q_{\mu\nu}^\dagger = Q_{\nu\mu}$ and therefore in $\hat{F}_{\mu\nu}$ the imaginary part is chosen since $\mathrm{Im}[Q_{\mu\nu}] = \frac{-i}{2}(Q_{\mu\nu} - Q_{\mu\nu}^\dagger)$.

The coefficient c_{sw} is calculated non-perturbatively [43] within the Schrödinger functional which is a specially suited renormalization scheme on the lattice. Through-
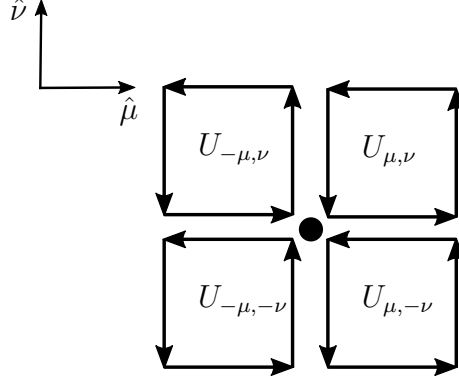
Figure 4.2: Clover term $Q_{\mu\nu}(n)$.

out this thesis, we will make use of those results for the generation of gauge configurations.

4.5   Scale setting and Renormalization

We know that a physical observable calculated on the Lattice has a well defined continuum limit where the lattice dependence has to cancel out

$$\lim_{a\to 0} P(g(a), m(a), a) = P_0. \tag{4.5.1}$$

The Callan-Symanzik equations

$$\frac{dP(g,m,a)}{d\log a} = \left(\frac{\partial}{d\log a} + \frac{\partial g}{\partial \log a}\frac{\partial}{\partial g} + \frac{\partial m}{\partial \log a}\frac{\partial}{\partial m} \right) P(g,m,a) = 0 \tag{4.5.2}$$

tell us how the bare parameters depend on the lattice spacing so as that Eq. (4.5.1) holds. A very important function is the beta function

$$\beta(g) = -\frac{\partial g}{\partial \log a} \stackrel{g\to 0}{=} -\beta_0 g^3 - \beta_1 g^5 + \mathcal{O}(g^7) \tag{4.5.3}$$

which determines how the bare coupling depends on the lattice spacing a. We can expand around $g = 0$ as written above where the first two completely universal coefficients determined within perturbation theory read for the case of N colors

and N_f flavors

$$\beta_0 = \frac{1}{(4\pi)^2}\left(\frac{11}{3}N - \frac{2}{3}N_f\right), \qquad (4.5.4)$$

$$\beta_1 = \frac{1}{(4\pi)^2}\left(\frac{34}{3}N^2 - \frac{10}{3}NN_f - \frac{N^2-1}{N}N_f\right). \qquad (4.5.5)$$

By solving and then inverting Eq. (4.5.3) so as to get a function $a(g_0)$ we notice that the continuum limit $a \to 0$ corresponds to $g_0 \to 0$. This property is called asymptotic freedom which is a genuine feature of QCD. Since the lattice regularization is nothing but a very special and convenient regularization procedure the two first universal coefficients apply also for the Lattice regularization. Lattice calculations usually take place at the other end of the spectrum, in the IR where the coupling constant is of order 1. Thus, none of the perturbative renormalization schemes are well suited. Lattice results are rarely compared to loop calculations within perturbative QCD, due to the fact that perturbative results are not valid at low energies where LGT is more powerful. This is one of the reasons because the Lattice comunity uses its own non-perturbative renormalization schemes the Schrödinger functional being one of them. For details we refer the reader to [44,45].

When starting a new simulation we have 3 parameters at our disposal $(\beta_L, \kappa, c_{\text{sw}})$. All of them depend nontrivially on the lattice spacing a and its dependence can be studied for a given action (e.g. Wilson action with two $\mathcal{O}(a)$ improved quarks). Firstly, the lattice spacing needs to be calculated. A common choice for doing so relies on the Sommer parameter r_0 [46]. This physical quantity is related to the static force between two quarks in the limit where they are infinitely heavy. Its physical value $r_0^{\text{phys}} \approx 0.5\text{fm}$ comes from experimental data. On the lattice we find this quantity in the Wilson loop, which is a closed temporal loop of links

$$\langle W(r,t)\rangle = c(r)\exp\left(-tV(r)\right) \qquad (4.5.6)$$

where r and t are the lenghts in space and time respectively. Taking the derivative of the potential we arrive at the force $F(r) = -\frac{dV(r)}{dr}$. Once extracted we need to find the adimensional number r_0 where [46]

$$F(r_0)r_0^2 = 1.65. \qquad (4.5.7)$$

Finally we just calculate the lattice spacing as the ratio of $(ar_0)/r_0^{\text{phys}}$ where the numerator comes directly from the simulation. We can repeat this process for different values of β_L so as to obtain a function $a(\beta_L)$.

For setting the mass scale, i.e. tuning the quark mass we can use hadronic renormalization schemes. One often uses ratios of hadron masses such as M_π/M_N or M_π/M_ρ because this reduces the quark mass dependence which leads then to smaller errors in the upcoming extrapolation. One may then compute at a given β_L mass ratios for different values of κ and then extrapolate to the κ^* where the ratio takes its physical value. Repeating this process for different values of β_L will yield a function $\kappa^*(\beta_L)$ such that we know how to tune the value of κ when approaching the continuum limit ($\beta_L \to \infty$) along the renormalization group trajectory that automatically will reproduce the real world in the continuum. Nevertheless, one rarely simulates along the κ^* trajectory since it would correspond to very small values of the quark masses and complications in the inversion of the Dirac operator appear. One prefers to simulate at unphysical masses and perform a chiral extrapolation at the end.

4.5.1   The PCAC mass: improvement of local operators

An alternative path to compute the renormalized quark mass $\overline{m}$ (cf. Eq. (4.3.7)) can be given by using the PCAC relation which is an operator identity that in euclidean space holds when inserted in expectation values. It relates the divergence of the non-singlet axial current $A_\mu^a = \bar{\psi}\gamma_\mu\gamma_5\frac{\tau^a}{2}\psi$ to the pseudoscalar density $P^a = \bar{\psi}\gamma_5\frac{\tau^a}{2}\psi$

$$\partial_\mu A_\mu^a = 2mP^a \qquad N_f = 2. \tag{4.5.8}$$

This relation can be derived by computing the Ward Identity associated to a chiral rotation of the fields. It is very useful in the context of renormalization and improvement. For example, it can be shown that the computation of the improvement coefficient c_{sw} is calculated by enforcing the PCAC relation at finite lattice spacing to order $\mathcal{O}(a^2)$. This is done by applying distinct operators $\mathcal{O}$ that yield a non-vanishing matrix element with the axial current and pseudoscalar density respectively [47]. The PCAC mass can be defined by applying for example the pseudoscalar density operator on each side and taking the expectation value. This choice is specially convenient since the pseudoscalar density two point function

has a very good signal-to-noise ratio

$$\partial_\mu \left\langle A_\mu^a(x) P^b(0) \right\rangle = 2m \left\langle P^a(x) P^b(0) \right\rangle. \tag{4.5.9}$$

One can then solve for m and write

$$m_{\mathrm{PCAC}}^{bare} = \frac{1}{2} \frac{\partial_\mu \left\langle A_\mu^a(x) P^b(0) \right\rangle}{\left\langle P^a(x) P^b(0) \right\rangle} \tag{4.5.10}$$

Notice that the quark mass is unrenormalized. This is due to the fact, that matrix elements that directly involve the bare fields need to further undergo a renormalization process so as the theory to become predictive. Since no other gauge invariant operators of dimension smaller or equal than 3 can mix with the operators appearing above implies that A_μ^a, V_μ^a, P^a are multiplicatively renormalizable. On top of that, the improvement process described in Sec. 4.4.1 will only guarantee the $\mathcal{O}(a)$ improvement of the spectrum (in particular hadron masses or energy values appearing in the exponents of n-point functions). Therefore one needs to improve and further renormalize also composite operators like V, A or P such that matrix elements of these operators approach the right continuum value. Common ways of relating them proceed through the regularization independent (RI) scheme or RI/MOM [48] or the Schrödinger Functional. One writes the $\mathcal{O}(a)$ improved and renormalized operators as

$$V_\mu^{a,r} = Z_V(g_0^2)(V_\mu^a + ac_V \partial_\nu^{\mathrm{imp}} \sigma_{\mu\nu}^a), \tag{4.5.11}$$

$$A_\mu^{a,r} = Z_A(g_0^2)(A_\mu^a + ac_A \partial_\nu^{\mathrm{imp}} P^a), \tag{4.5.12}$$

$$P^{a,r} = Z_P(g_0^2, \mu) P^a. \tag{4.5.13}$$

It turns out that the renormalization condition for the determination of the renormalization constants is set in the chiral limit. This means that $Z_{A,V}(g_0^2 \to 0) \to 1$ since both currents are conserved in the continuum chiral limit and thus are automatically renormalized. This assures also that there is no remaining scheme dependence if the results are continuum extrapolated. In order to connect to the case of finite quark mass additional parameters b_A, b_P, b_V, b_m [49] appear which are neglected in this work since the correction is very small. The case of Z_P is different: a scale dependence remains, tightly connected to the scheme that was used for its computation. Therefore, in order to quote results in some continuum

renormalization scheme as $\overline{\text{MS}}$ one needs an additional coefficient connecting the lattice renormalization scheme and the $\overline{\text{MS}}$ scheme at some scale which is commonly set to $\mu = 2\text{GeV}$ although the matching of renormalization schemes is done at much higher perturbative scales of order $\sim 100\text{GeV}$. We can then write the renormalized PCAC mass quoted in $\overline{\text{MS}}$ at a scale of $\mu = 2\text{GeV}$ as

$$\overline{m}_{\text{PCAC}}^{\overline{\text{MS}}}(\mu = 2GeV) = c^{\text{SFto}\overline{\text{MS}}}(\mu) \left(\frac{Z_A}{Z_P}\right) \frac{1}{2} \frac{\partial_\mu^{\text{imp}} \left\langle A_\mu^a(x) P^b(0)\right\rangle}{\left\langle P^a(x) P^b(0)\right\rangle} \qquad (4.5.14)$$

where A_μ^a and P^a are $\mathcal{O}(a)$ improved. In order to be consistent with the order of improvement considered, there are also some improved derivatives $\partial_\mu^{\text{imp}}$ that can be defined such that they are free of $\mathcal{O}(a)$ effects (see Appendix B). The relation with the definition of the renormalized mass given in Eq. (4.3.7) is the following. The bare PCAC-mass given in Eq. (4.5.10) vanishes for those values of β_L and κ for which the theory is chirally symmetric. Thus, we can use it to determine the value of $m_c(g_0^2)$ (or in the lattice version $\kappa_c(\beta_L)$). In a second step, we notice that after additive renormalization both definitions are proportional to each other. Still, there is a non-trivial factor r_m between them (see Eq. (E.1) of [50])

$$Z_A(g_0^2)/Z_P(g_0^2, \mu_R) m_{\text{PCAC}}^{bare} = Z_m(g_0^2) r_m(g_0^2)(m - m_c(g_0^2)) = r_m \overline{m}. \qquad (4.5.15)$$

where R is the renormalization scheme chosen for the calculation of Z_P at the scale μ.

4.6   Following lines of constant physics: temperature scans

We have discussed in the context of Thermal Field Theroy in Sec. 2.3 that Wick rotating a QFT theory to Euclidean time leads to a statistical interpretation and consequently, the inverse length of the periodic (antiperiodic for fermions) imaginary time extension denotes the temperature of the statistical system as stated in Eq. (4.1.3). Performing scans in temperature is one of the main objectives of Lattice QCD at finite temperature and is of major importance throughout this thesis. In principle, one can think of three straightforward manners of varying temperature:

- By varying the number of points in the time direction. This is called fixed scale approach and it has the advantage that one does not need to retune any of the bare parameters of the theory. This is very convenient if one is interested in coarse scans. The obvious drawback is that the discrete steps limit the resolution. In real simulations there are other practical restrictions concerning the algorithm and its parallelization such that the situation is even worse.

- By varying the lattice spacing a. These types of scans are far more difficult, since a retuning of all bare parameters is necessary in order to remain at the line of constant physics described by Eq. (4.5.2). This is achieved by choosing one dimensionfull quantity that remains constant throughout the whole scan. The scans used in this thesis are done at fixed renormalized quark mass following Eq. (4.5.14).

- Implementing shifted boundary conditions. This method was proposed in [51–53]. It relies on $SO(4)$ euclidean symmetry in the continuum while considering shifted boundary conditions in time. The conceptual idea is very similar to the twisted boundary idea [54] where those shifts are implemented in space enabling a finer resolution in momentum values such that $p_i^n = (2\pi n_i/L) + \theta_i$ where θ is related to the shift parameter. In a similar way, implementing those shifts in time, permits a much finer scan since three new parameters appear for choosing the imaginary time length making a total of 4 instead of one. In addition, considering different shift parameters does not imply a change in the bare parameters. Some details and one application is presented in Chapter 5.

4.7   Aspects of Montecarlo simulations

In this section, we will mention the strategy of generating configurations. From previous sections we have stated that expectation values are calculated according to

$$\langle \mathcal{O} \rangle = \lim_{N \to \infty} \frac{1}{N} \sum_{\{\phi\} \in \Gamma_{\mathrm{MC}}} \mathcal{O}(\{\phi\}) \tag{4.7.1}$$

where the configurations are generated according to the probability distribution
density

$$dP(\{\phi\}) = \frac{e^{-S^{\text{lat}}_{QCD}[\phi]} \, \mathcal{D}\{\phi\}}{\int \mathcal{D}\{\phi\} \, e^{-S^{\text{lat}}_{QCD}[\phi]}}. \tag{4.7.2}$$

We have also managed to identify the correct degrees of freedom of LGT, or more
precisely, its parametrization, such that we can write the integration measure as

$$\mathcal{D}\{\phi\} = \mathcal{D}[U]\mathcal{D}[\bar{\psi}, \psi] = \prod_{n \in \Lambda} \prod_{\mu} dU_{\mu}(n) \prod_{n' \in \Lambda} d\psi(n') d\bar{\psi}(n'). \tag{4.7.3}$$

The object dU is called the Haar measure which is well known in the mathematical
literature. The defining properties are gauge invariance and normalization. We
can list them as

$$dU = d(UV) = d(VU), \qquad \int_{SU(3)} dU = 1, \qquad U, V \in SU(3). \tag{4.7.4}$$

Putting everything together we can now write the full QCD lattice version of
the path integral for two flavors of light degenerate $\mathcal{O}(a)$ improved quarks (Pauli
term) with parametrically very heavy doublers (Wilson term) in the presence of a
dynamical gluon background as follows

$$Z^{\text{lat}}_{\text{QCD}} = \int \mathcal{D}[U]\mathcal{D}[\bar{\psi}, \psi] e^{-S^{W}_{G}[U] - S^{W,\text{imp}}_{F}[U, \bar{\psi}, \psi]} \tag{4.7.5}$$

where S^{W}_{G} is Eq. (4.2.8) and $S^{W,\text{imp}}_{F}$ is the improved fermion action of Eq. (4.4.5).
The goal is now to approximate the previous integral with stochastic methods
like Monte-Carlo algorithms and by doing this, generate a set of configurations on
which observables can be measured. We notice that the fermion action has the
following structure

$$S^{W,\text{imp}}_{F}[\bar{\psi}, \psi, U] = \sum_{n,m} \bar{\psi}(n) D_{W}(n, m)[U]\psi(m) \tag{4.7.6}$$

and thus, is quadratic in the fields. By remembering that fermionic variables obey
anticommutation relations such as $\{\eta_i, \eta_j\} = 0$ one can integrate out the fermion

fields analytically and write

$$Z_{\text{QCD}}^{\text{lat}} = \int \mathcal{D}[U] \det[D_W]_u \det[D_W]_d \ e^{-S_G^W[U]} \tag{4.7.7}$$

$$= \int \mathcal{D}[U] \det[D_W D_W^\dagger] \ e^{-S_G^W[U]} \tag{4.7.8}$$

where we have made explicit that there is one determinant factor coming from each flavor. Still, isospin symmetry assures that $\det[D_W]_u = \det[D_W]_d$ and the determinant operation is understood to be taken over space-time, color and spin indices. In addition, γ_5-hermiticity allows us to write it in a single determinant that involves the Dirac operator itself and its hermitian conjugate. Once fermions are integrated out, we are left with the normalized probability distribution density

$$dP[U] = \frac{\det[D_W D_W^\dagger] \ e^{-S_G^W[U]} \mathcal{D}[U]}{\int \mathcal{D}[U] \ \det[D_W D_W^\dagger] \ e^{-S_G^W[U]}}. \tag{4.7.9}$$

Neglecting the contribution of the determinant corresponds to the quenched approximation. In this limit, sea quarks are neglected in the calculation. One integrates out fermionic degrees of freedom because implementing Grassmann variables on computational platforms is a very non-trivial task. By doing so, the $\det[D_W D_W^\dagger]$-factor emerges. This leads us to another problem. The calculation of the determinant factor is very demanding due to its very non-local character. In general, the number of terms of a determinant of a $N \times N$ matrix goes like $N!$. In practical situations it is completely unfeasible to estimate. This leads to the inclusion of pseudo fermions [55]. The analogy relies on the relation of gaussian integrals between fermionic and bosonic variables. More precisely, the determinant factor appears in the denominator for bosonic variables and in the numerator for fermionic ones as it can be seen from Eq. (4.7.9). In order to see this let us consider a real vector of bosonic fields ϕ_i where i may be labelling for example the position on which it is evaluated (let i take discrete values), and the same for a real fermionic field η_i which is a Grassmann variable. We compute then the gaussian

integral for each case and encounter

$$\int \prod_i^N d\phi_i e^{-1/2\phi_i M_{ij}\phi_j} = (2\pi)^{N/2}\frac{1}{(\det[M])^{1/2}} \qquad (4.7.10)$$

$$\int \prod_i^N d\eta_i e^{-1/2\eta_i M_{ij}\eta_j} = (\det[M])^{1/2}. \qquad (4.7.11)$$

Starting from this relation, we first can promote ϕ_i and η_i to complex fields (as it is in QCD), this adds another factor of the $\det[M]^{\mp 1/2}$ respectively. On top of that, we account for both flavors which adds another $\det[M]^{\mp 1}$. We then are able to write

$$\int \mathcal{D}[\bar{\psi},\psi]e^{-\bar{\psi}_u D_u^W \psi_u - \bar{\psi}_d D_d^W \psi_d} = N_{(\pi)}\int \mathcal{D}[\phi^\dagger,\phi]e^{-\phi^\dagger (D_W D_W^\dagger)^{-1}\phi} \qquad (4.7.12)$$

where $N_{(\pi)}$ is an overall irrelevant normalization constant and we have used the fact that Dirac operator is free of zero modes such as $\det[D] = 1/\det[D^{-1}]$. It is now straightforward to understand that the fields ϕ and $\phi^\dagger$ need to posses the same degrees of freedom as the fermionic Grassmann variables $\bar{\psi}$ and ψ with the only distinction that they obey Bose-Einstein statistics instead of Fermi-Dirac. In simulations they are implemented as ordinary complex numbers. Nevertheless, this does not represent a problem since the mathematical identity of Eq. (4.7.12) assures that the correct effective action is generated which is the only relevant aspect that needs to be respected in order to properly generate configurations.

4.7.1   Completing a trajectory with the Hybrid Montecarlo algorithm

The simulation starts from a given configuration, i.e. one needs to specify all links that live between all lattice points. These are $(4 \times N_t \times N_s^3)$ 3×3 unitary matrices of unit determinant. Common choices for the starting configuration are all matrices equal to the identity matrix (this corresponds to the free theory) and is given the name of cold start or all matrices set to random elements of the $SU(3)$ group which is referred to as hot start. The fields that need to be stored are the links U whereas the pseudofermions ϕ will only help to sample the configuration space correctly. The Hybrid Montecarlo algorithm (HMC) is a global update algorithm.

This means, that at the beginning of each trajectory, a complete global set of fields is proposed at every space-time point.

One trajectory starts by generating a random vector η which has pseudofermionic degrees of freedom according to the probability distribution $e^{-\eta^\dagger \eta}$. Then, one constructs the true field ϕ by applying the Dirac operator $D[U]\eta = \phi$. This field will be kept constant throughout the whole trajectory. The Molecular Dynamics evolution equations are responsible for the update of the link variables and are the classical solutions of a non-relativistic system with Hamiltonian $H[P,Q]$ that depends on the generalized coordinates Q and their corresponding conjugate momenta P. The Hamilton operator reads

$$H[P,Q] = \frac{1}{2}P^2 - S[\phi,U] \tag{4.7.13}$$

where

$$S[\phi,U] = S_G^W[U] + \phi^\dagger(D_W D_W^\dagger)^{-1}\phi \tag{4.7.14}$$

One identifies the generalized coordinates Q with the parameters $\alpha_\mu^a(n)$ that define a given link $U_\mu(n) = e^{i\alpha_\mu^a(n)T^a}$ where T^a are the generators of $SU(3)$. In addition there are some conjugate momenta $P_\mu^a(n)$ which are the conjugate variables to α^a. Those are also random generated at the beginning of the trajectory according to the probability distribution $\exp[-\frac{1}{2}[\sum_{n\in\Lambda} P_\mu^a(n)P_\mu^a(n)]$ which comes from the first term in Eq. (4.7.13). Then one needs to solve the Hamilton equations for updating alternately $\alpha_\mu^a(n)$ (or equivalently, $U_\mu(n)$) and $P_\mu^a(n)$

$$\dot{P} = -\frac{\partial H}{\partial Q} = \frac{\partial S}{\partial Q}, \tag{4.7.15}$$

$$\dot{Q} = \frac{\partial H}{\partial P} = P. \tag{4.7.16}$$

The derivative ($\dot{P}$ and $\dot{Q}$) is to be understood with respect to the molecular dynamics evolution time. From the practical point of view, standard integrators such as the leapfrog technique, induce $\mathcal{O}(\epsilon^2)$ errors. Nevertheless, the algorithm can be made exact by introducing a Metropolis step at the end of the trajectory. In each substep of the update, the full inverse $(DD^\dagger)^{-1}$ needs to be calculated. This represents the most time consuming part of the algorithm. Once a sufficient amount of substeps (updates of U and P) have been performed, one completes the

trajectory with a Metropolis-accept-reject step. It accepts the configuration if a random number $r \in [0, 1)$ is smaller than $e^{-\Delta H[P,U|P',U']}$ where (P, U) and (P', U') are the variables at the beginning and at the end of the trajectory respectively. The trajectory itself has a length of $\tau = \epsilon n$ and n is the number of substeps. If the trajectory is accepted, the configuration is stored and a new trajectory begins from the previous configuration. This introduces autocorrelation effects that have to be studied in detail in order to not underestimate the error in our measurements. For a fixed τ, increasing the number of substeps n will lead to smaller errors and consequently to a bigger acceptance rate at the cost of needing more computational resources. Thus, one has to find a good set of parameters for the algorithm to produce uncorrelated configurations without spending too much Montecarlo time within each trajectory. Due to the Metropolis step at the end of the trajectory, the HMC algorithm is exact to machine precision in the sense that any accumulated numerical errors from the MD evolution will be fixed such that at the end we will indeed have configurations according to the probability distribution written in Eq. (4.7.9). Notice how by switching to the Hamilton formalism we are able to introduce conjugate momentum variables that always appear quadratically and are usually integrated out. Nevertheless, it is precisely those variables that are responsible for choosing "the direction in Montecarlo-space" that the trayectory is pointing to. They are gaussian distributed and chosen at the beginning. The same applies to η and consequenctly to ϕ which is also chosen randomly with the difference that it is kept fixed during the whole trajectory. Both choices of η and $P_\mu^a(n)$ together with the Metropolis step at the end are responsible for introducing quantum fluctuations into the system. This is important since the MD evolution is a completely deterministic process.

4.8   Euclidean 2pt-functions

A whole set of very basic but also important quantities are 2pt-functions. They correspond to the expectation value of an operator $O_1(0)^\dagger$ that creates a whole tower of states with the same quantum numbers as the operator O_1 itself at some time $t = 0$, and another operator O_2 that annihilates states with quantum numbers

of O_2 at some time t

$$\left\langle O_2(t)O_1^\dagger(0)\right\rangle = \frac{1}{Z}\text{Tr}\left[e^{-(\beta-t)H}O_2 e^{-tH}O_1\right] \qquad (4.8.1)$$

where $O_2(t) = e^{tH}O_2(0)e^{-tH}$, β is the finite time extent of the box and H is the lattice version of the QCD Hamilton operator acting on a Hilbert space as

$$H\left|n\right\rangle = E_n\left|n\right\rangle \qquad E_n < E_{n+1} \qquad \forall n \geq 0 \qquad (4.8.2)$$

It can be easily seen within this framework that $Z = \sum_n \left\langle n|e^{-\beta H}|n\right\rangle = \sum_n e^{-\beta E_n}$. Inserting a complete set of states one can arrive at

$$\left\langle O_2(t)O_1^\dagger(0)\right\rangle = \frac{\sum_{m,n}\left\langle m|O_2|n\right\rangle\left\langle n|O_1^\dagger|m\right\rangle e^{-t\Delta E_n}e^{-(\beta-t)\Delta E_m}}{1 + e^{-\beta\Delta E_1} + e^{-\beta\Delta E_2} + ...} \qquad \Delta E_n = E_n - E_0.$$
$$(4.8.3)$$

Taking the limit $\beta \to \infty$ (equivalent to sending the temperature $T \to 0$) will yield the spectral decomposition of the euclidean correlator

$$\lim_{\beta\to\infty}\left\langle O_2(t)O_1^\dagger(0)\right\rangle = \sum_n \left\langle 0|O_2|n\right\rangle\left\langle n|O_1^\dagger|0\right\rangle e^{-t\Delta E_n}. \qquad (4.8.4)$$

This formula, although strictly valid only at zero temperature will be of conceptual importance for extracting hadronic energy levels from euclidean correlators.

4.8.1   Evaluation of mesonic 2pt-functions

In order to already make connection with the work that will be presented in the next chapters, we will discuss here the evaluation of two-point functions of operators that create mesonic states within $N_f = 2$ QCD with degenerate masses. In this sense, we accommodate the two quark spinors into an $SU(2)$ doublet such that $\bar{\psi} = (\bar{u}\ \bar{d})$.

Throughout this thesis, we will mostly consider mesonic 2pt-functions with insertions of the local vector current, axial vector current and pseudo scalar density. They are defined as

$$V_\mu^a(x) = \bar{\psi}(x)\gamma_\mu\frac{\tau^a}{2}\psi(x), \qquad A_\mu^a(x) = \bar{\psi}(x)\gamma_\mu\gamma_5\frac{\tau^a}{2}\psi(x), \qquad P^a(x) = \bar{\psi}(x)\gamma_5\frac{\tau^a}{2}\psi(x)$$
$$(4.8.5)$$

State	J^{PC}	Particles
Vector	1^{--}	$\rho^{\pm}, \rho^0, \omega, K^*, \phi$, ...
Axial Vector	1^{++}	a_1, f_1, ...
Pseudoscalar	0^{-+}	$\pi^{\pm}, \pi^0, \eta, K^{\pm}, K^0$, ...

Table 4.1: Quantum numbers corresponding to the quark bilinears for $V_\mu(x)$, $A_\mu(x)$ and $P(x)$ together with the lightest mesons of the QCD spectrum carrying the same quantum numbers.

where τ^a are 2 by 2 Pauli matrices and have quantum numbers listed in Table 4.1. They create a full tower of states that have a nonzero overlap with the operator in question. In this regard, they do not only couple to the ground state but also to all other resonances and excited states with the same quantum numbers. Due to the fact that we are considering QCD with two degenerate light flavors of quarks we have a full $SU(2)$ isospin symmetry at our disposal that can be exploited. Mesons can then be arranged into degenerate multiplets corresponding to irreducible representations of $SU(2)$. The flavor structure of the operators listed in Eq. (4.8.5) is such that they belong to the adjoint (or isovector) representation of $SU(2)$. This can be shown by defining a flavor rotation on the quark fields as

$$\psi \to \psi' = e^{i\alpha^a\tau^a}\psi \qquad \bar{\psi} \to \bar{\psi}' = \bar{\psi}e^{-i\alpha^a\tau^a} \tag{4.8.6}$$

where α^a are the 3 parameters that define the flavor rotation and τ^a are the 3 different 2 by 2 Pauli matrices that correspond to the generators of SU(2) in the fundamental representation. One can show by using the expansion of the exponential for a small set of parameters α^a that for all operators in Eq. (4.8.5) regardless of their Dirac structure,

$$
\begin{aligned}
O^c \to O'^c &= \bar{\psi}'\Gamma\frac{\tau^c}{2}\psi' \\
&= \bar{\psi}(1 - i\alpha^a\tau^a)\Gamma\frac{\tau^c}{2}(1 + i\alpha^a\tau^a)\psi \\
&= O^c + i\alpha^a(-if_{acb})O^b + \mathcal{O}(\alpha^2) \\
&= O^c + i\alpha^a(T_{\mathcal{A}}^a)_{cb}O^b + \mathcal{O}(\alpha^2)
\end{aligned}
$$

where we used the fact that $(T_{\mathcal{A}}^a)_{bc} = -if_{abc}$ are the generators in the adjoint representation. We have proven that they belong to the adjoint representation with

total isospin $I = 1$. This fact represents a technical advantage for the calculation of 2pt-functions since quark disconnected diagrams cancel out.

Consider the meson interpolator $O^a(x) = \bar{\psi}(x)\Gamma\frac{\tau^a}{2}\psi(x)$. We want then to calculate the expectation value of the 2pt-function with one operator at x and the other at the origin. We define the quark propagator as the Wick contraction of two quark fields with the same flavor

$$D_q^{-1}(x,y)_{\alpha\beta}^{ab} = \overline{q(x)_\alpha^a\ \bar{q}(y)_\beta^b} \qquad q = u, d \tag{4.8.7}$$

where we have made color and spin indices explicit. We can then write

$$
\begin{aligned}
\langle O_1^a(x)O_2^b(0)\rangle &= \left\langle \bar{\psi}(x)\Gamma_1\frac{\tau^a}{2}\psi(x)\bar{\psi}(0)\Gamma_2\frac{\tau^b}{2}\psi(0)\right\rangle \\
&\stackrel{a=b=3}{=} \frac{1}{4}\left\langle \left[\bar{u}(x)\Gamma_1 u(x) - \bar{d}(x)\Gamma_1 d(x)\right]\left[\bar{u}(0)\Gamma_2 u(0) - \bar{d}(0)\Gamma_2 d(0)\right]\right\rangle \\
&= \frac{1}{4}\left\langle \bar{u}(x)\Gamma_1 u(x)\bar{u}(0)\Gamma_2 u(0)\right\rangle + \frac{1}{4}\left\langle \bar{d}(x)\Gamma_1 d(x)\bar{d}(0)\Gamma_2 d(0)\right\rangle \\
&\quad -\frac{1}{4}\left\langle \bar{u}(x)\Gamma_1 u(x)\bar{d}(0)\Gamma_2 d(0)\right\rangle - \frac{1}{4}\left\langle \bar{d}(x)\Gamma_1 d(x)\bar{u}(0)\Gamma_2 u(0)\right\rangle
\end{aligned}
$$

For simplicity, we have chosen $a = b = 3$ but the result is the same for other values of $a = b = 1, 2$ with the property that for $a \neq b$ the result is zero since they have different third isospin component and the operators would be orthogonal to each other.

$$
\begin{aligned}
\langle O_1^3(x)O_2^3(0)\rangle &= \frac{1}{4}\left(-\left\langle \text{Tr}[D_u^{-1}(x,0)\Gamma_1 D_u^{-1}(0,x)\Gamma_2]\right\rangle + \left\langle \text{Tr}[D_u^{-1}(x,x)\Gamma_1]\text{Tr}[D_u^{-1}(0,0)\Gamma_2]\right\rangle \right. \\
&\quad - \left\langle \text{Tr}[D_d^{-1}(x,0)\Gamma_1 D_d^{-1}(0,x)\Gamma_2]\right\rangle + \left\langle \text{Tr}[D_d^{-1}(x,x)\Gamma_1]\text{Tr}[D_d^{-1}(0,0)\Gamma_2]\right\rangle \\
&\quad - \left\langle \text{Tr}[D_u^{-1}(x,x)\Gamma_1]\text{Tr}[D_d^{-1}(0,0)\Gamma_2\right\rangle \\
&\quad \left. - \left\langle \text{Tr}[D_d^{-1}(x,x)\Gamma_1]\text{Tr}[D_d^{-1}(0,0)\Gamma_2]\right\rangle\right)
\end{aligned}
$$

where the trace operation is over spin and color indices. Since we have isospin symmetry $D_u^{-1} = D_d^{-1}$ and the disconnected pieces that involve $D_q^{-1}(x,x)$ or $D_q^{-1}(0,0)$ cancel out. So we are left with

$$\langle O_1^a(x)O_2^b(0)\rangle = -\frac{\delta^{ab}}{2}\left\langle \text{Tr}[D^{-1}(x,0)\Gamma_1 D^{-1}(0,x)\Gamma_2\right\rangle. \tag{4.8.8}$$

Quark disconnected pieces are very expensive to calculate, due to the fact that one needs all-to-all propagators and the full inverse of the Dirac operator is needed. At this point, it is important to say that quark disconnected diagrams are nonetheless connected in the usual field theoretical sense since any number of gluon lines can be drawn. On the lattice, these contributions are already included in the gauge average over configurations. As an additional fact one should note that the lattice Dirac operator we use satisfies γ_5-hermiticity. This property is expressed as

$$D^\dagger = \gamma_5 D \gamma_5 \implies (D^{-1})^\dagger = \gamma_5 D^{-1} \gamma_5 \qquad (4.8.9)$$

It relates the forward propagator with the backward propagator. This reduces the cost of the calculation drastically, since only one propagator needs to be calculated. Thus, we can write the above results for the fully connected piece as follows

$$\left\langle O_1^a(x) O_2^b(0) \right\rangle = -\frac{\delta^{ab}}{2} \left\langle \mathrm{Tr}[D^{-1}(x,0)\Gamma_1 \gamma_5 \left(D^{-1}(x,0)\right)^\dagger \gamma_5 \Gamma_2] \right\rangle. \qquad (4.8.10)$$

4.8.2   Placing sources on the lattice to calculate $D^{-1}(x,y)$

From the discussion in the previous section it has become clear that the most relevant building block is the propagator, i.e. the inverse of the Wilson-Dirac operator $D_W^{-1}[U]$ which is a matrix depending only on the link variables. One should keep in mind that we consider the $\mathcal{O}(a)$ improved action with the Pauli-term included and a non-perturbatively determined c_{sw} coefficient. We define then the propagator as

$$D^{-1}(x,y)_{\alpha,\beta}^{ab} \qquad x,y \in \Lambda. \qquad (4.8.11)$$

The Dirac operator D_W is a sparse matrix (cf. periodic boundary conditions), due to the theory being local, up to discretization effects. Due to the periodic boundary conditions in space and anti-periodic in time, we know that our action is invariant under a change of variables $x_\mu \to x_\mu + a_\mu$. In this sense, the propagator can only depend on the relative position of points x and y. Although in principle we are interested in the full inverse, i.e. calculating for every configuration the propagation of a quark from any point to any point of the lattice (all-to-all-propagator), this is not needed for the case of quark-connected contributions to 2pt-functions.

It is natural then to introduce point sources

$$\eta(x, x_0)_{\alpha\alpha_0}^{aa_0} = \delta(x - x_0)\delta_{aa_0}\delta_{\alpha\alpha_0}. \tag{4.8.12}$$

Instead of inverting the full Dirac matrix, we are only interested in the propagation of a quark from point x_0 to any point in the lattice (usually the source is placed at a random position in the lattice). Consequently we are looking for the solution of the following set of linear equations

$$\sum_{y \in \Lambda} D(x, y)_{\alpha\beta}^{ab} G(y, x_0)_{\beta a_0}^{ba_0} = \delta(x - x_0)\delta_{aa_0}\delta_{\alpha\alpha_0} \tag{4.8.13}$$

where G is the desired propagator that connects the source located at x_0 with any point in the lattice. This has to be solved for any combination of α_0 and a_0; in total $12 \times N_s^3 \times N_\tau$ equations. This is much less demanding than inverting the full dirac matrix for any pair x and y. There are multiple techniques that yield a satisfactory inverse of the Dirac operator. Known techniques are the conjugate gradient or Bi-conjugate Gradient methods [56]. Both of them rely on an iterative procedure, where one has a minimizing condition that improves the solution in every step until the desired accuracy is reached. In this work the 'DFL-SAP-GCR' solver is used (see [57] for a general review on solvers and [58] for accelerated HMC algorithms) in the process of generating configurations and for calculating expectation values of fermionic observables such as two-point functions.

Once the solution $G(y, x_0)$ is found one can repeat the procedure for different values of x_0 relying on the fact that translational invariance holds. Thus, one can define a set of source positions $\{x_0^i\}$ for $i = 1, ..., N_{\text{src}}$ and perform an average over the solutions

$$\langle G(y, 0) \rangle = \frac{1}{N_{\text{src}}} \sum_{i=1}^{N_{\text{src}}} G(y + x_0^i, x_0^i) \tag{4.8.14}$$

relying on the fact that we know that $G(x, y) = G(x - y)$. The expectation value of the previous equation should really be understood within one configuration and not to be confused with the true gauge average which is taken a posteriori. This procedure reduces our error roughly by a factor $\sqrt{N_{\text{src}}}$. Some interesting remarks can be made at this point. For the following argument we restrict ourselves to one configuration. Notice that by choosing a definite source position x_0^i, the Dirac

operator that needs to be inverted involves the links at position x_0^i. The fact that we average the propagator with another solution that was calculated by placing the source at x_0^j with $i \neq j$ relies on translational invariance. Nevertheless, it is clear that in general $U_\mu(x_0^i) \neq U_\mu(x_0^j)$. The difference is due to statistical fluctuations which to some extent can be interpreted as quantum fluctuations which are contributions to the path integral. This means that by averaging over different sources we are already including some quantum fluctuations although we are working within one single configuration. It is straightforward then to understand that the number of measurements of some observable is $N_{\mathrm{meas}} = N_{\mathrm{cnfg}} N_{\mathrm{src}}$. Following this lines, it is in principle possible to find one single representative gauge configuration with a very big volume (so as to reduce autocorrelation effects) and fill it up with a lot of sources such that we include all quantum fluctuations. In recent years it has been a topic of extensive study by Martin Lüscher (*"Stochastic Locality and simulations of very big lattices"*; talk at Schloss Liseland.) For a general introductory overview of LGT the author recommends [59] and [60] for a more elaborated description.

5

Shifted boundary conditions (sbc)

The path integral Z of a theory is the most fundamental object from which all properties of a system can be derived. Lattice results are called "from first principles" because expectation values are calculated taking into account all (relevant) non-perturbative effects that otherwise would be neglected if relying on perturbative approaches. Nevertheless, even on the Lattice, one never calculates the path integral itself. One usually writes that

$$\langle \mathcal{O} \rangle = \frac{\int d\{\phi\}\ \mathcal{O}(\{\phi\})e^{-S[\{\phi\}]}}{Z} = \lim_{N\to\infty} \frac{1}{N} \sum_{i\in\Gamma_{MC}} O_i \qquad (5.0.1)$$

where Γ_{MC} is a set of N configurations generated according to the probability density $dP = e^{-S[\{\phi\}]}d\{\phi\}$. If the theory is invariant under some global symmetry transformation, it can be shown that the path integral can be decomposed into a sum of functional integrals each giving the contribution from states with definite symmetry properties [61, 62]. Therefore, an interesting problem is to try to gain information about the relative contribution, due to the individual sectors.

5.1 Momentum distribution

Relying on translational invariance one can study the relative contribution of those states with well defined total momentum $\mathbf{p}$ [51–53]. Within the canonical ensemble

one can write it as

$$\frac{R(\beta, \mathbf{p})}{L^3} = \left\langle \hat{P}^{(\mathbf{p})} \right\rangle = \frac{\mathrm{Tr}\{e^{-\beta \hat{H}} \hat{P}^{(\mathbf{p})}\}}{\mathrm{Tr}\{e^{-\beta \hat{H}}\}} \tag{5.1.1}$$

where $\hat{P}^{(\mathbf{p})}$ is the projector onto those states with total momentum $\mathbf{p}$. By introducing the partition function $Z(\beta, \boldsymbol{\xi}) = \mathrm{Tr}\left\{e^{-\beta(\hat{H} - i\hat{P}\boldsymbol{\xi})}\right\}$ where $\boldsymbol{\xi}$ is called the shift parameter $\boldsymbol{\xi} = \mathbf{z}/\beta$ which is a ratio of two physical lengths and therefore does not need any normalization (see Fig. 5.1.) We can express $R(\beta, \mathbf{p})$ as

$$R(\beta, \mathbf{p}) = \beta^3 \int d^3\boldsymbol{\xi} \; e^{-i\beta \mathbf{p}\boldsymbol{\xi}} \frac{Z(\beta, \boldsymbol{\xi})}{Z(\beta, \mathbf{0})}. \tag{5.1.2}$$

One can further define the generating functional $K(\beta, \mathbf{z})$ as

$$e^{-K(\beta, \boldsymbol{\xi})} = \frac{1}{L^3} \sum_{\mathbf{p}} e^{i\beta \mathbf{p}\boldsymbol{\xi}} R(\beta, \mathbf{p}) \tag{5.1.3}$$

and consequently

$$K(\beta, \boldsymbol{\xi}) = -\log\left(\frac{Z(\beta, \boldsymbol{\xi})}{Z(\beta, \mathbf{0})}\right). \tag{5.1.4}$$

The partition function $Z(\beta, \boldsymbol{\xi})$ has the same action as $Z(\beta, \mathbf{0})$ with the only difference that states with total momentum $\mathbf{p}$ are weighted by a phase $e^{i\beta \mathbf{p}\boldsymbol{\xi}}$. This is equivalent to consider that the fields obey shifted boundary conditions

$$\phi(\beta, \mathbf{x}) = \pm\phi(0, \mathbf{x} - \beta\boldsymbol{\xi}) \tag{5.1.5}$$

with $(\pm)$ for bosons and fermions respectively.

5.2 The free energy of a shifted system

If one considers a relativistic 4-dimensional QFT in euclidean time, the Lorentz group is replaced by the $SO(4)$ group. One may reinterpret the shift parameter $\boldsymbol{\xi}$ as an imaginary velocity $\boldsymbol{v} = i\boldsymbol{\xi}$ and boost the system. Following the definition of Eq. (2.3.2) we can write the free energy density of a boosted (or shifted) system as

$$f(\beta, \boldsymbol{\xi}) = -\frac{1}{\beta L^3} \log Z(\beta, \boldsymbol{\xi}). \tag{5.2.1}$$
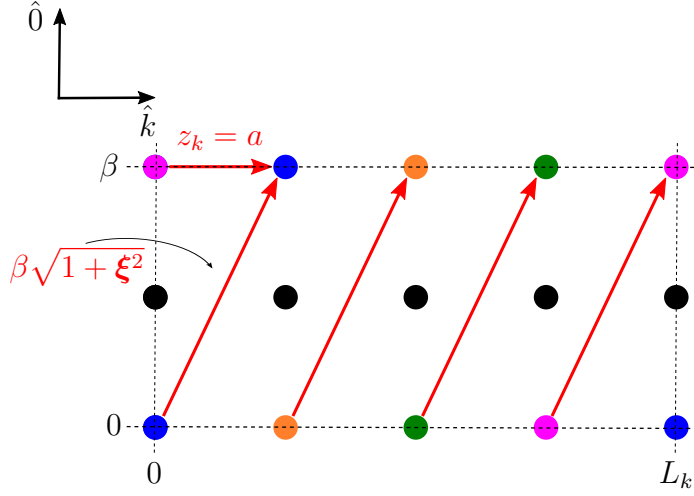
Figure 5.1: Shifted lattice with renormalized shift parameter $\xi_k = \frac{z_k}{\beta}$ for a 4×2 lattice. Points with the same color are identified.

At zero-temperature and in infinite volume, $SO(4)$ symmetry implies that the free energy density of the boosted system cannot depend on $\boldsymbol{\xi}$

$$\frac{\partial}{\partial \boldsymbol{\xi}} \left[\lim_{\beta \to \infty} \lim_{L \to \infty} \left(-\frac{1}{\beta L^3} \log Z(\beta, \boldsymbol{\xi}) \right) \right] = 0. \tag{5.2.2}$$

This statement goes back to the general argument that if a theory (more precisely, its vacuum) is invariant under the action of some group G, expectation values of operators that belong to non-trivial irreducible representations of the group, vanish. In [53], the authors demonstrated that when the imaginary time extent is finite (so $T \neq 0$) the $SO(4)$ group is broken softly due to the effect of the boundaries. In this case, the free energy does depend on $\boldsymbol{\xi}$ but only through the combination $\beta\sqrt{1 + \boldsymbol{\xi}^2}$ due to the remaining $SO(3)$ symmetry. The key observation is then to recognize that there is a relation between an unshifted system at inverse temperature $\beta\sqrt{1 + \boldsymbol{\xi}^2}$ and a system shifted by a vector $\boldsymbol{\xi}$ at inverse temperature β. This can be written in terms of the free energy densities of both systems as

$$f(\beta, \boldsymbol{\xi}) = f(\beta\sqrt{1 + \boldsymbol{\xi}^2}, \mathbf{0}) \tag{5.2.3}$$

which is the master equation, strictly valid only in the thermodynamic limit, from which a whole set of non-trivial relations can be derived. The finite extension of the spatial directions is a further source of $SO(4)$ breaking and the authors

calculated the corrections to Eq. (5.2.3) which are exponentially suppressed with the lightest screening mass of the theory [53].

5.3 Thermodynamic potentials

Taking derivatives of the free energy with respect to β and $\boldsymbol{\xi}$ one is able to calculate the cumulants of energy and momentum respectively. Moreover, by using Eq. (5.2.3) one finds that they are related by a linear transformation. This corresponds to the statement that in the thermodynamic limit, the total energy and momentum distributions are related. This opens the possibility to calculate thermodynamic potentials within a relativistic QFT from momentum distribution cumulants at non-zero shift and vice versa.

For example, it can be shown that the entropy density of a system at inverse temperature $\beta\sqrt{1+\boldsymbol{\xi}^2}$ can be calculated as

$$s = -Z_T \frac{\beta\left(1+\boldsymbol{\xi}^2\right)^{3/2}}{\xi_k} \left\langle T_{0k} \right\rangle_{\boldsymbol{\xi}} \tag{5.3.1}$$

where $\left\langle T_{0k} \right\rangle_{\boldsymbol{\xi}}$ corresponds to the expectation value in a lattice with shifted boundary conditions. The coefficient Z_T renormalizes the off diagonal components of the energy-momentum tensor due to breaking of translational invariance to a discrete subgroup on the lattice and will be computed non-perturbatively in $SU(3)$ pure gauge theory in Sec. 5.5. Eq. (5.3.1) is one of many relations one can derive based on Eq. (5.2.3). Other thermodynamic potentials like specific heat can also be expressed in terms of expectation values of energy momentum tensor correlators at non-zero shift [51–53].

5.4 Temperature scans with shifted boundaries

As already stated in Sec. 4.6 one can use the parameter $\boldsymbol{\xi}$ to vary the temperature without altering the ultraviolet behavior of the theory under consideration. This means, that lattice spacings as well as all renormalization constants do not change when varying the value of $\boldsymbol{\xi}$. This may be very relevant when trying to perform fine scans due to the presence of e.g. a phase transition. In [53] the authors illustrated

the increased temperature-resolution due to the additional parameters ξ_1, ξ_2 and ξ_3.

5.5   Renormalization of the momentum density on the lattice using (sbc)

This section corresponds to published work in PoSLattice2013. In particular, subsections 5.5.1, 5.5.2, 5.5.3, 5.5.5 and 5.5.6 contain identical text from the original work in [63] with minor structural modifications in order to maintain consistency across the whole chapter. In the above mentioned sections, some minor changes are introduced as well as additional information and plots that initially were left out due to restrictions in space in the published version.

5.5.1   Introduction

In the modern approach to study static and dynamic properties of a strongly interacting quantum system like the Quark-Gluon-Plasma (QGP), calculating the transport coefficients plays an important role. These "low energy constants" of hydrodynamics, viewed as an effective field theory, can be extracted from spectral functions calculated in the underlying theory via the famous Kubo-formulas (see for instance [8]). As a prominent example we can mention the shear viscosity η which parametrizes how efficiently the momentum of a layer of fluid diffuses in the direction orthogonal to the layer. It should be obvious that transport of energy and momentum is governed by energy-momentum-tensor-correlators.

Due to the lack of continuous Poincaré invariance induced by the lattice regularization, the discretized Energy-momentum-tensor (EMT) is only conserved up to cutoff effects

$$\partial_\mu T_{\mu\nu}^{\text{lat}} = 0 + \mathcal{O}(a^2). \tag{5.5.1}$$

Hence, on the lattice we have to further investigate the renormalization pattern of $T^{\mu\nu}$ in order to have a well defined continuum limit of its correlation functions and be able to safely extract transport coefficients.

This project will address the problem of calculating the renormalization constant Z_T of the momentum densitiy T^{0k} for $SU(3)$ pure Yang-Mills theory with the Wilson plaquette action (see Eq. (4.2.8)) using shifted boundary conditions.

5.5.2   Renormalization pattern of $T_{\mu\nu}$

In the continuum, the pure SU(3) EMT can be splitted into a traceless part and the trace itself,

$$T_{\mu\nu} = \theta_{\mu\nu} + \frac{1}{4}\delta_{\mu\nu}\theta, \qquad (5.5.2)$$

where

$$\theta_{\mu\nu} = \frac{1}{4}\delta_{\mu\nu}F^a_{\rho\sigma}F^a_{\rho\sigma} - F^a_{\mu\alpha}F^a_{\nu\alpha} \quad \text{and} \quad \theta = T_{\mu\mu}. \qquad (5.5.3)$$

On the lattice, we discretize $\theta_{\mu\nu}$ by using the "clover" form $\hat{F}_{\mu\nu}$ of the field strength tensor as written in Eq. (4.4.6).

In order to proceed with the renormalization of the momentum densitiy T^{0k} we need to know the transformation properties of this operator under the symmetry group of the lattice: the hypercubic group denoted by $H(4)$. The operators $T_{\mu\nu}$ split into irreducible representations of $H(4)$. In particular, $T^{0k} = \theta^{0k}$ belongs to a six dimensional representation along with the other off-diagonal components of $T^{\mu\nu}$ [64]. Since there are no other gauge invariant operators of equal or lower dimension, T^{0k} renormalizes multiplicatively

$$T^{\mathrm{R}}_{\mu\nu} = Z_T T_{\mu\nu} \qquad \mu \neq \nu. \qquad (5.5.4)$$

Our aim will be to determine in a non perturbative way the renormalization constant $Z_T = Z_T(g_0^2)$. Since in the continuum the momentum density is a conserved current, this renormalization constant does not depend on any external scale (like temperature) but only on the bare coupling g_0^2. In the classical field theory, $Z_T = 1$ and due to asymptotic freedom, we expect

$$\lim_{g_0^2 \to 0} Z_T = 1. \qquad (5.5.5)$$

The $\mathcal{O}(g_0^2)$ correction has been computed in Lattice Perturbation Theory in [65] yielding

$$Z_T(g_0^2) = 1 + 0.27 g_0^2 + \mathcal{O}(g_0^4). \qquad (5.5.6)$$

5.5.3   Consistency check on $s\beta^3/s_{SB}\beta^3$ in the free theory

Before moving on to the extraction of Z_T, we performed consistency checks on the free theory where this constant takes a value of 1. In [53] the authors calculated
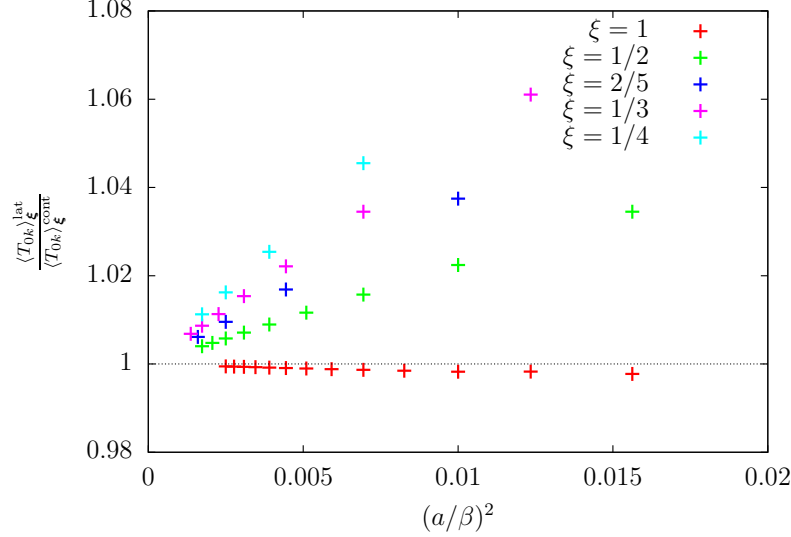
Figure 5.2: Ratio of momentum densities at non-zero shift as a function of $(a/\beta)^2$.

in perturbation theory the expectation value of the momentum density in the free lattice theory for different values of the shift. Via Eq. (5.3.1) they extracted the ratio of the entropy at finite lattice spacing with respect to the continuum value

$$\frac{(s\beta^3)}{(s_{SB}\beta^3)} = 1 + c_1(a/\beta) \tag{5.5.7}$$

where $s_{SB}\beta^3 = 32\pi^2/45$ for $SU(3)$ and c_1 is a coefficient that encodes the lattice discretization effects and depends only on $(a/\beta)^2$. It has to approach zero when the true continuum limit is taken. In Fig. 5.2 we show the ratio of momentum densities at different $\boldsymbol{\xi}$. At leading order in Lattice Perturbation theory cutoff effects grow as we lower the value of $\boldsymbol{\xi}$.

In order to reproduce this ratio we have to simulate at very small values of g_0^2 which corresponds to the free theory. This leads to some complications. On the one hand the critical slowdown of the algorithm makes it harder to maintain autocorrelation effects under control (see e.g. [66]). On the other hand, finite size effects are of order $\sim e^{-g_0^2 L/\beta}$. This requires that one chooses a very large aspect ratio L/β for decreasing values of g_0^2. We simulate at 4 different values of g_0^2 at fixed $a/\beta = 1/2$ and $\boldsymbol{\xi} = (1, 0, 0)$. Results are summarized in Table 5.1.
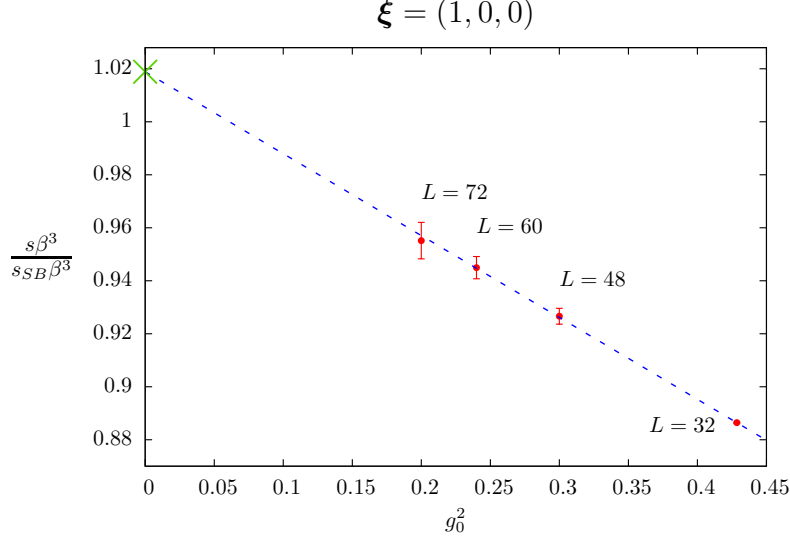
Figure 5.3: Linear extrapolation to $g_0^2 \to 0$ of $s\beta^3/s_{SB}\beta^3$ for $a/\beta = 1/2$ fixed.

After the linear extrapolation, the intercept at $g_0^2 = 0$ takes a value of

$$\frac{(s\beta^3)}{(s_{SB}\beta^3)} = 1.018(6) \tag{5.5.8}$$

which compared to the analytic value calculated in lattice perturbation theory $(s\beta^3)/(s_{SB}\beta^3) = 1.026$ gives a standard deviation of $\sim 1.2\sigma$, indicating that we are able to reproduce the "free value" within errors and we have managed to maintain finite size effects under control.

5.5.4   Ensemble generation: *heat-bath* and *overrelaxation*

We will briefly discuss the update strategy for generating configurations in pure $SU(3)$ gauge theory. The goal is to generate configurations according to the probability distribution $P[U] \sim e^{-S_G^W[U]}$ where $S_G^W[U]$ follows the definition of Eq. (4.2.8). Since we have no fermions, the theory is automatically $\mathcal{O}(a)$ improved. The method used is a combination of heat-bath and overrelaxation steps together with an accept-reject step at the end similar to the one introduced in Sec. 4.7. Both of them correspond to local changes of the link variables. This situation is qualitatively different from the HMC algorithm where a single change of a link variable $U_\mu(n)$ would require the recomputation of the action that involves

all link variables present in the lattice. This is due to the non-locality property of the determinant factor of Eq. (4.7.9). In the present case, the difference of the action involves only the calculation of the six plaquettes where the updated link is contributing. The remaining plaquettes are not affected by the local change. On the one hand, local update algorithms are in general less expensive in terms of computing resources since the change in the action involves only the nearby plaquettes. On the other hand, autocorrelation effects may become a problem since the configuration space is scanned very slowly. The local change in the action by changing $U_\mu(n) \to U'_\mu(n)$ is given by

$$\Delta S = -\frac{2}{g_0^2} \text{ReTr}\{[U'_\mu(n) - U_\mu(n)]A\} \tag{5.5.9}$$

where A is the sum of 6 *staples*. Each staple is the product of the links that together with $U_\mu(n)$ form the plaquettes that are modified due to the change in $U_\mu(n)$. Due to the group property of $SU(3)$ we can modify a given link $U_\mu(n)$ by multiplying it with some random group element $g \in SU(3)$. The question is then what link is modified and in which manner such it is likely to be accepted in the Metropolis step at the end.

The heat-bath algorithm proposes a new link variable $U'_\mu(n)$ according to the probability distribution

$$P[U'_\mu(n)] \sim \exp\left(\frac{2}{g_0^2}\text{ReTr}[U'_\mu(n)A(n)]\right). \tag{5.5.10}$$

This assures that the new link variable, although different, yields a change in the action that is likely to be accepted. When repeating this process for all link variables in the lattice one often refers to it as a heat-bath sweep. The overrelaxation algorithm is used in order to speed up the sampling of the configuration space so as to reduce autocorrelation effects. This is done by performing local changes of all link variables (overrelaxation sweep) with the restriction that the total change in the action vanishes. This assures that overrelaxation sweeps do not affect the probability of a given configuration to be accepted or not. For detailed information we refer the reader to the seminal paper of Cabibbo and Marianari [67]. The configuration update that was used throughout this project is characterized by

a combination of one heat bath and two overrelaxation sweeps. All simulations are started from a hot start, so a finite number of updates steps (combination of heat-bath and overrelaxation sweeps) has to be completed in order for the system to reach thermalization. From this point on, all configurations produced are valid configurations on which observables can be measured. The number of thermalization steps was set to 1000.

5.5.5   Computation of $Z_T(g_0^2)$

In order to extract the relevant renormalization constant we need some already renormalized quantity to compare with. For this purpose, we make use of the generating functional associated with the momentum distribution $K(\beta, \boldsymbol{\xi})$ already introduced in Eq. (5.1.4) which is a ratio of two partition functions: in the numerator the one with shifted boundary conditions and in the denominator the ordinary partition function with periodic boundary conditions. It turns out that this is a RGI quantity and therefore has a finite and universal continuum limit. Any derived quantity that one can compute by taking derivatives with respect to this functional is already renormalized, too. In particular,

$$\frac{\partial K(\beta, \boldsymbol{\xi})}{\partial \xi_k} = -\beta Z_T \left\langle \int d^3x \, T_{0k}(x) \right\rangle_{\boldsymbol{\xi}}. \tag{5.5.11}$$

How to systematically compute ratios of partition functions was first investigated in [61, 62]. This motivated the study of the contribution to any field theoretical partition function due to states with a given set of quantum numbers. If we stick to the case of $\boldsymbol{\xi} = (\xi_1, 0, 0)$ it can be shown that the cumulants of this functional are related to thermodynamic potentials [53]. For example, the entropy of the system at finite lattice spacing is defined by

$$\left(\frac{s}{T^3}\right)_R = \frac{\partial^2}{\partial \xi_1^2} \left. \frac{K(\beta, \xi)}{T^3 L^3} \right|_{\xi=0} = \frac{2K(\beta, \xi)}{|\xi|^2 T^3 L^3} + \mathcal{O}(|\boldsymbol{\xi}^2|) \tag{5.5.12}$$

where an R subscript indicates that this is a renormalized quantity and β is the inverse temperature. In [51] , the authors calculated $K(\beta, \boldsymbol{\xi})$, the last equality in the previous equation coming from a limiting procedure so as to estimate the value of the renormalized entropy in terms of $K(\beta, \boldsymbol{\xi})$. By combining Eq. (5.5.11) and Eq. (5.5.12) one can come to the conclusion that by measuring the expecta-

tion value of the momentum density along the x-direction at nonzero shift and taking the first derivative with respect to ξ_1 one ends up with an unrenormalized prediction for $(s/T^3)_0$ that can be written as the traditional definition of the derivative:

$$\left(\frac{s}{T^3}\right)_0 = \frac{\partial}{\partial \xi_1} \left.\frac{\langle T_{01}\rangle_\xi}{T^4}\right|_{\xi=0} = \lim_{\xi_1 \to 0}\left[\frac{\langle T_{01}\rangle_\xi}{T^4 \xi_1}\right]. \tag{5.5.13}$$

The last term cancels out because of symmetry considerations since at zero shift the expectation value of the total momentum vanishes. Since on the lattice ξ_1 is not a continuous parameter that can be tuned we have to stick to rational values and let them be close to zero where the derivative needs to be evaluated. The best choice is to take $\xi_1 = a/\beta$ to get more accurate results for increasing number of points in the temporal direction. In addition, since $\langle T_{01}\rangle_\xi$ is an odd function in ξ_1 our errors are of $\mathcal{O}(a/L_0)^2$. The master equation for calculating the renormalization constant is then

$$Z_T = \frac{\left(\frac{s}{T^3}\right)_R}{\left(\frac{s}{T^3}\right)_0} \tag{5.5.14}$$
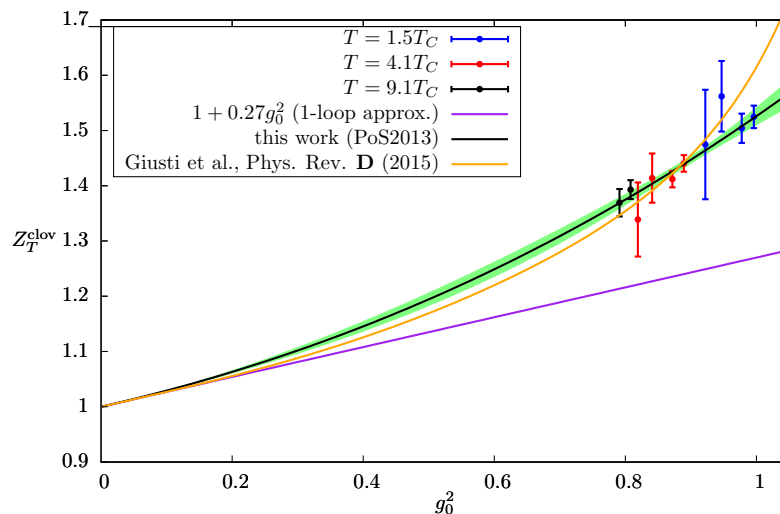
Figure 5.4: Z_T as a function of g_0^2 for three different sets of values of temperature.

5.5.6   Results & Conclusions

Results are summarized in Table 5.2. Different capital letters correspond to different temperatures. $A_\#$ corresponds to $T = 1.5T_C$, $B_\#$ correspond to $T = 4.1T_C$ and $C_\#$ corresponds to $T = 9.1T_C$. In [51] the scale setting was done following the data of [68] via the Sommer parameter r_0 and T_C can be found in [69]. In order to connect with perturbative results we used as an input for our fit function the one-loop approximation that was calculated in [65] (Eq. (5.5.6)). It should be noticed that the good agreement between the three different data sets corresponding to different temperatures is an indication that we have $\mathcal{O}(aT)^2$ errors under control since Z_T should not depend on any external scale. After performing the fit to the data our final result is

$$Z_T(g_0^2) = \frac{1 + 0.1368g_0^2 + 0.1858g_0^4}{1 - 0.1332g_0^2}. \tag{5.5.15}$$

(see Fig. 5.4 and Table 5.2). The absolute error is ~ 0.008 when $g_0^2 \in [0.8, 1.0]$. Recently, Giusti et al. recomputed the value of $Z_T(g_0^2)$ following a somewhat different approach [70]. Calculating $K(\beta, \boldsymbol{\xi})$ becomes quickly very demanding. They extracted Z_T by noting that derivatives with respect to g_0^2 yield differences of expectation values of the action at different shift parameters which can be calculated very accurately with current cumputer resources. Further tree-level improvement of the data of $\langle T_{0k} \rangle_{\boldsymbol{\xi}}$ yields the result shown in Fig. 5.4.

5.5.7   Outlook

In the future, one could try to simulate at smaller values of the coupling in order to better match the perturbative prediction. This may be difficult because of the critical slowing down of the algorithm to generate configurations correctly distributed across the whole Montecarlo space (see. [71] for topological charge freezing and solutions to the problem). Due to the following relation

$$Z_T \langle T_{0k} \rangle_{\boldsymbol{\xi}} = \frac{\xi_k}{1 - \boldsymbol{\xi}^2} z_T \left(\langle T_{00} \rangle_{\boldsymbol{\xi}} - \langle T_{kk} \rangle_{\boldsymbol{\xi}} \right) \qquad \text{no summation on } k. \tag{5.5.16}$$

that can be derived from Eq. (5.2.3) the authors in [70] already calculated the renormalization factor z_T of the diagonal components with previous information on Z_T and by measuring $\langle T_{00} \rangle$ and $\langle T_{kk} \rangle$ at non-zero shift. Ultimately the purpose

is to simulate within full QCD. Therefore adding the contribution of dynamical fermions is of key interest to extract renormalization constants that can be used for the calculation of energy-momentum-tensor correlators.

5.5.8   Tables

g_0^2	L/a	L/β	$\langle T_{01} \rangle \beta L^3$	$s\beta^3/s_{SB}\beta^3$
0.429	32	18	1365.1(4)	0.88641(2)
0.3	48	24	3371(11)	0.9266(3)
0.24	60	30	5371(24)	0.944(4)
0.2	72	36	7819(56)	0.955(7)

Table 5.1: Ensembles used for the $g_0^2 \to 0$ extrapolation so as to estimate $c_1(a/\beta)$. The number of point in the time direction is kept fixed at $L_0/a = 2$ as well as the shift parameter $\boldsymbol{\xi} = (1, 0, 0)$. For each $\beta_L = 6/g_0^2$ 40000 measurements were performed.

Lat	$6/g_0^2$	L_0/a	L/a	$\left(\frac{s}{T^3}\right)_R$	$\left(\frac{s}{T^3}\right)_0$	Z_T
A_2	6.024	5	16	4.98(4)	3.27(3)	1.52(2)
A_3	6.137	6	18	4.88(6)	3.24(4)	1.50(3)
A_4	6.337	8	24	5.12(19)	3.28(6)	1.56(6)
A_5	6.507	10	30	4.9(3)	3.32(9)	1.47(10)
B_2	6.747	5	16	6.53(6)	4.53(2)	1.44(2)
B_3	6.883	6	18	6.40(6)	4.53(2)	1.41(2)
B_4	7.135	8	24	6.42(20)	4.54(2)	1.41(4)
B_5	7.325	10	30	6.1(3)	4.55(4)	1.33(7)
C_2	7.426	5	20	7.13(8)	5.11(3)	1.39(2)
C_3	7.584	6	24	6.94(12)	5.07(3)	1.36(3)

Table 5.2: The values of the column $\left(\frac{s}{T^3}\right)_R$ were taken from [51].

Chapter 6

Chiral dynamics in the low-temperature phase of QCD

Ever since the discovery of asymptotic freedom in QCD [26], theorists have strived to understand the properties of a hadronic system under extreme conditions (very high temperature and densities). It seems very natural to think that, since the coupling constant of QCD becomes smaller with increasing energy, at very high temperatures, the system may be very weakly coupled and consists of weakly coupled quarks and gluons. Moreover, from the cosmological point of view, it is believed that the universe started in a dense and hot phase. In the process of expanding, it cooled down undergoing a phase transition from a plasma phase to a confined hadronic phase, the one we now live in. Therefore, a conjectured phase diagram of QCD has emerged which has been the object of very intensive study in the last decades (see Fig. 6.1).

Chiral symmetry plays a fundamental role in the study of thermodynamic properties of QCD. As already pointed out in Sec. 3.3.2, the QCD Lagrangian density exhibits a new symmetry in the limit of vanishing quark masses. For the case of two degenerate flavors ($N_f = 2$), the new symmetry group is $SU(2)_L \times SU(2)_R$ which correspond to two independent flavor rotations of the left-handed and right-handed components of the quark fields. An order parameter associated with the spontaneous breaking of chiral symmetry can be defined: the quark condensate. Symmetries, their breaking pattern or the complete absence of them are closely related to phase transitions and to their order. In the massless scenario, the spontaneous breaking pattern is the same as in a 3-dimensional ferromagnet
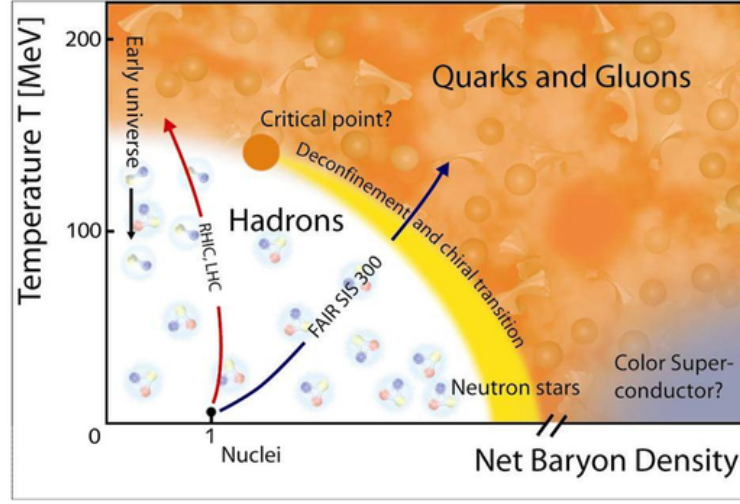
Figure 6.1: Conjectured phase diagram of QCD. On the x-axis one often plots baryon chemical potential μ_B which can be identified with baryon density. The y-axis corresponds to temperature. Figure taken from [72].

$(O(4) \sim SU(2)_L \times SU(2)_R \to SU(2)_V)$ which is second order, the quark condensate being its order parameter.[1] When adding a third strange quark, Pisarski and Wilczek argued that the transition cannot be second order [74]. On the other hand, Lattice simulations at zero chemical potential μ_B show that the transition is a crossover at physical quark masses (see e.g. [75, 76]). This means that all thermodynamic functions are analytic functions of the thermodynamic variables. In this scenario the transition temperature T_C is not a sharply defined quantity since it depends on the observable which is used for its determination. This is consistent with the picture that in the real world, chiral symmetry is only realized approximately due to the light non-vanishing up and down quark masses and the spontaneous symmetry breaking pattern described above is only an appropriate approximation. Nevertheless, depending on the value of the strange quark mass, there may be a critical point located at the endpoint of the first order phase transition line where the crossover region begins. Locating the critical point of QCD (if any) is one of the most important tasks in the field of QCD thermodynamics.

---

[1]Second order phase transitions, can be grouped into universality classes regardless of their distinct nature. Within each class, there is a set of critical exponents which dictate how certain key observables vanish or diverge as the critical temperature is approached (for further reading on universality classes see [73]).

The plasma phase, usually called Quark-Gluon-Plasma (QGP), is claimed to be produced in ultra relativistic heavy ion collisions (at RHIC and LHC). In order to reproduce the extreme conditions of the early stages of the universe, regarding temperature and density, very heavy nuclei like gold or lead are smashed against one another almost at the speed of light ($\sqrt{s} = 200$GeV at RHIC). During this process the system evolves from a state where quark and gluons are released and consequently almost free, to a confined phase where a vast type of hadronic species are measured at the detectors. In the intermediate state, an almost (still strongly coupled) ideal fluid is produced in local thermal equilibrium which can be described by the laws of hydrodynamics.

One of the pieces of evidence for the formation of a QGP-type system comes from so-called thermal fits [77]. One performs a two parameter fit within the grand-canonical ensemble so as to obtain temperature and baryon chemical potential by feeding in data on the relative abundance of about a dozen different hadron species. The temperature extracted in this way is called freeze-out temperature, which can be interpreted as the temperature at which the system becomes dilute enough that inelastic hadron-hadron collisions cease to modify abundance ratios [78]. At RHIC, typical freeze-out temperatures are in the range 155-180MeV [79] which is interesting since these values are quite close to the expected chiral transition temperatures that come from Lattice studies [80].

Elliptic flow is one of the most famous experimental signatures for the formation of the QGP. In this type of analysis one studies the azimuthal distribution of produced particles perpendicular to the beam pipe. The idea is to recognize that as the two heavy nuclei collide at non-zero impact parameter, a few hundred nucleon-nucleon collisions occur. If the system did not behave collectively, the distribution of produced particles would be distributed isotropically due to the free-streaming of the produced particles. The data however tells otherwise. What one sees is a very anisotropic distribution favoring the production of particles along directions corresponding to small angles with respect to the interaction plane. The hydrodynamic description does surprisingly well at predicting this anisotropy [81].

In order to conclude this brief discussion about the high-temperature phase, one should mention one of the most celebrated results coming from the AdS/CFT correspondence. It concerns $\mathcal{N} = 4$ supersymmetric Yang-Mills theory at non-zero temperature which has been shown to share a lot of common features with

the plasma phase of QCD. In 2001, Policastro et al. [82] calculated the ratio of shear viscosity to entropy density $\eta/s = 1/4\pi$ in the limit of infinite coupling. This value is surprisingly low compared to other systems (for water is about two orders of magnitude bigger) making maybe the QGP one of the most interesting and perfects fluids discovered so far.

Chapter 6 is based on published work in Physical Review D [18, 83] and Proceedings of Science [84, 85] and the purpose of the author here was to provide a self consistent description of the whole research project. In this regard, although structured differently, most parts of the chapter are taken over from the original publications so as to respect the formulation of the precise arguments and their interpretation originally made. For completeness, the same applies to appendices E and F which were slightly modified with respect to the originals. The author of this thesis was involved in all steps of this project, starting from the generation of configurations (especially for the finite volume check for which a complete additional ensemble was generated) until the extraction and analysis of all quantities considered in this thesis.

In the low-temperature phase, it is natural to ask how close the properties of the excitations are to those of the known hadrons at zero temperature. Viewed globally, the spectrum does not appear to change much until temperatures close to the transition temperature are reached, where the rapid crossover to a deconfined and chirally symmetric phase takes place. This conclusion is based on the success of the hadron resonance gas model in describing equilibrium properties of the medium (particularly the equation of state and quark number susceptibilities) computed in lattice QCD [86–88], and on its success in describing particle yields in heavy-ion collisions [89, 90]. However, reliable information about individual excitations is sparse. For the work presented in this chapter several different ensembles are used. They are summarized in Table 6.1.

6.1   Introduction

One picture of the low-temperature phase that has had significant phenomenological success is the hadron resonance gas (HRG) model. It assumes that the

Lattice Calculation (#)	T [MeV]	$\overline{m}^{\overline{\text{MS}}}$ [MeV]	$N_\tau \times N_s^3$	a [fm]
(I) C1 scan	150-235	~ 15	16×32^3	$\sim 0.05 - 0.08$
(I) D1 scan	177-203	~ 8	16×32^3	$\sim 0.06 - 0.07$
(II) O7-type	170	~ 13	24×64^3	~ 0.05
(III) A5-type	150	~ 15	16×48^3	~ 0.08

Table 6.1: Summary of all QCD thermal ensembles used in this thesis. The number in the parenthesis in the first column indicates in what section this ensemble is used. The quark mass is given at a scale $\mu = 2\text{GeV}$.

thermodynamic properties of the system, including the conserved charge fluctuations, are given by the sum of the partial contributions of non-interacting hadron species

$$\log Z(T, V, \mu^a) = -\frac{V}{2\pi^2} \sum_i \int_0^\infty dp \, p^2 \log \left(1 - \xi_i z_i(\mu^a) e^{-E_i/T}\right). \qquad (6.1.1)$$

The sum extends over all resonances up to about 2.5GeV mass, since for most of them the width is not large compared to the temperature. The coefficient $\xi_i = \pm 1$ takes into account mesons and baryons respectively. Eventually, one would like to couple the system to different chemical potential variables. This information is incoded in the fugacities $z_i = e^{(B_i \mu_B + S_i \mu_S + Q_i \mu_Q)/T}$ where B_i, S_i and Q_i correspond to baryon number, strangeness and electric charge of the different hadron species. Notice that $E_i = \sqrt{m_i^2 + \mathbf{p}^2}$ such that one feeds in a free vacuum-type dispersion relation in order to obtain thermodynamic medium properties. The model gives an economic description of particle yields in heavy-ion collisions (see the recent [89], [90] and references therein) and gives a good estimate of the pressure and charge fluctuations determined in lattice calculations [86–88]. On the other hand, relatively little is known with certainty about the spectral functions of local operators (say, the conserved vector current, the axial current or the energy-momentum tensor) at finite temperature, which encode the real-time excitations of the system [12]. The success of the HRG model for static quantities does not imply that the real-time excitations of the system are in any sense similar to the ordinary QCD resonances observed at $T = 0$.

A good starting point to investigate the excitations of the thermal medium is to study what becomes of the pion [91,92]. At sufficiently low temperatures $T \ll T_c$,

correlation functions can be computed using chiral perturbation theory. The result is that a well-defined pion quasiparticle persists, with small modifications to the real part of the pole, and a parametrically small imaginary part [93–95]. It is not clear how far up in temperature this treatment can be justified, since the partition function is certainly no longer dominated by the pions for $T \gtrsim 100\,\mathrm{MeV}$. However, the pion is special in that the Goldstone theorem guarantees the presence of a divergent static correlation length when $m \to 0$ for all temperatures in the chirally broken phase [96]. If we consider the temperature vs. quark-mass plane (T, m), this observation suggests an expansion in the quark mass around the point $(T, 0)$. In this case, one gives up on relating the chiral condensate $\langle \bar{\psi}\psi \rangle$ and the screening pion amplitude f_π to their $T = 0$ counterparts, however the range of applicability is significantly extended; see Fig. 6.2. This is the approach adopted by Son and Stephanov [97,98]. The result of their analysis is that a pion quasiparticle persists, with a parametrically small imaginary part compared to the real part of the pole position. The real part of its dispersion relation is, however, no longer the relation implied by Lorentz invariance, but rather

$$\omega_{\mathbf{p}}^2 = u^2(T)(m_\pi^2 + \mathbf{p}^2). \tag{6.1.2}$$

Here m_π is the inverse static correlation length in the pseudoscalar channel, and u, the 'pion velocity', is an a priori unknown function of temperature which can however be related to static quantities [98]. At finite temperature it is important to distinguish between the pion static screening mass and the quasiparticle mass. The former is the inverse length scale over which a localized pseudoscalar perturbation turned on adiabatically is screened. It is thus a property of the static response of the system. The pion quasiparticle mass is a property of the dynamic response and can be given the following interpretation. Suppose that the expectation value of the axial charge is driven out of equilibrium adiabatically by an external perturbation until the instant $t = 0$, where the perturbation is switched off. Consider then how the system relaxes back to equilibrium at large positive times. The pion quasiparticle mass (times $c^2/\hbar$) is the frequency at which the axial charge present in the system would oscillate as a function of time[2]. Technically, while the quasiparticle mass is the real-part of a pole of the retarded correlator $G_R(\omega, |\mathbf{p}| = 0)$ of

---

[2]The amplitude of the oscillations would be damped slowly in comparison with the oscillation frequency. The interpretation given is valid in the linear response approximation. By contrast,
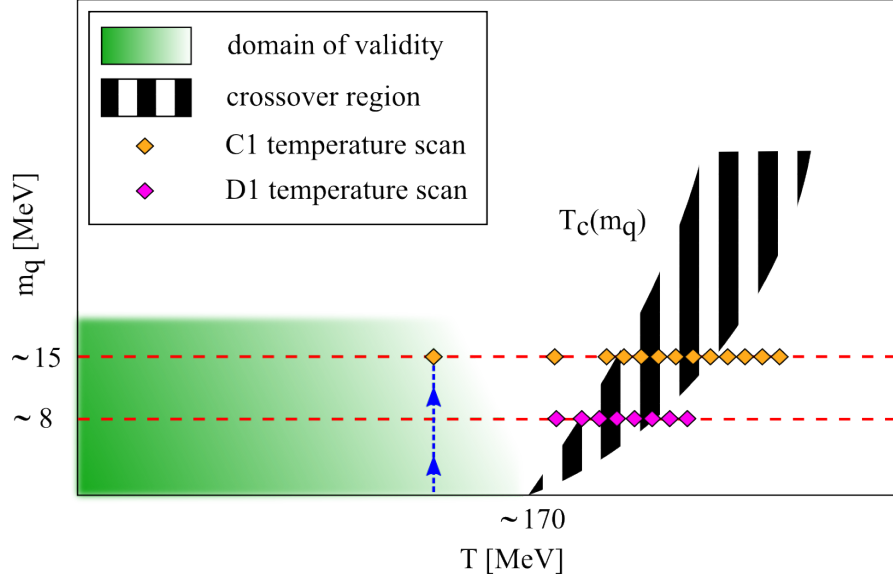
Figure 6.2: Sketch of the domain of validity of the chiral effective field theory in the quark mass vs. temperature plane. The expansion is represented by the blue arrowed vertical line. The quark mass on the vertical axis is understood to be $\overline{m}^{\overline{\text{MS}}}$. The value of the critical temperature at the chiral limit $T_c(0) \simeq 170$ is taken from [99].

the pseudoscalar density in the frequency variable, the static screening mass is a pole of $G_R(\omega = 0, \mathbf{p})$ in the spatial momentum $|\mathbf{p}|$. At zero temperature, Lorentz symmetry implies that the two masses are equal. Determining $u(T)$ using lattice QCD for a few temperatures below T_c is one of the main goals. We first rederive Eq. (6.1.2), present an improved estimator for $u(T)$, and show that the spectral function ρ_{A} of the axial charge density obeys the following exact sum rule for all temperatures, quark masses and spatial momenta,

$$\int_{-\infty}^{\infty} d\omega \, \omega \, \rho_{\text{A}}(\omega, T, \mathbf{p}) \Big|_0^T = -m \langle \bar{\psi}\psi \rangle \Big|_0^T. \tag{6.1.3}$$

The respective pion pole contributions (which dominate) at zero and at finite temperature satisfy the sum rule.

We will be working in QCD with two flavors of (O(a) improved Wilson) quarks with renormalized masses $8\text{MeV} \leq \overline{m}^{\overline{\text{MS}}} \leq 15\text{MeV}$. In this range of quark

---

perturbing a conserved quark number (vector charge) with a wave vector $\mathbf{k}$ leads to a purely damped late-time response $e^{-D\mathbf{k}^2 t}$, with D the diffusion coefficient.

masses, the transition from the low-temperature to the high-temperature phase is a crossover, as it is at physical quark masses. At vanishing m, there must be a sharp phase transition, however its nature is not known with certainty[3]. The crossover temperature, defined conventionally by some observable, depends quite strongly on the quark mass. The results of [99] indicate that the pseudo-critical temperatures are $T_c = 211(5)\,\mathrm{MeV}$ and $T_c = 193(7)\,\mathrm{MeV}$ at respectively $\overline{m}^{\overline{\mathrm{MS}}} \simeq 15\mathrm{MeV}$ and $\overline{m}^{\overline{\mathrm{MS}}} \simeq 8\mathrm{MeV}$ in the two-flavor theory. An extrapolation to $\overline{m}^{\overline{\mathrm{MS}}} = 0$ yields values between 160MeV and 175MeV for the critical temperature in the chiral limit [99]. See [75, 76] for other lattice studies of the transition in the two-flavor theory.

The dependence of T_c on the quark mass is sketched in Fig. 6.2. The expected domain of applicability of a chiral expansion around a point (T, m) for $T < T_c(m = 0)$ is also indicated by the shaded region. The two horizontal lines and the corresponding dots correspond to two scans at constant renormalized quark mass. Unfortunately, most of the ensembles considered in this first analysis correspond to the crossover region. We point out, however, that all observables considered here are well defined for any temperature and any quark mass; this is in particular true for the estimators of the quantity $u(T)$ introduced above. It is the interpretation of the quantity $u(T)$ as the velocity of a quasiparticle that is uncertain when calculating near or at the transition region.

The relatively strong dependence of the pseudocritical temperature on the quark mass tends to reduce the domain of applicability of the chiral expansion at fixed T. For instance, we clearly observe that the scaling $m_\pi^2 \propto m$ is violated at $T \simeq 180\,\mathrm{MeV}$. Instead the screening pion mass increases (sic!) as the quark mass is reduced from 15 MeV to 8 MeV. A plausible explanation is that at the smaller quark mass, the system is already entering the crossover region, where the chiral expansion breaks down.

We have found it useful to introduce the following 'effective chiral condensate' based on the Gell-Mann–Oakes–Renner (GOR) relation,

$$\langle\bar{\psi}\psi\rangle_{\mathrm{GOR}} \equiv -\frac{f_\pi^2 m_\pi^2}{m}. \tag{6.1.4}$$

By construction it has the property that it tends to the actual chiral condensate

---

[3]The possibility considered to be the 'standard scenario' is that it is a second order phase transition in the 3d O(4) universality class.

when $m \to 0$; it is of order m above T_c, and thereby an order parameter with respect to chiral symmetry. We remark that none of the observables considered here requires the use of a lattice action preserving chiral symmetry.

The goals of this project are the following:

1. test the validity of the chiral expansion around $(T, m = 0)$ and compute the pion quasiparticle velocity $u(T)$;

2. test the chiral expansion around $(T = 0, m = 0)$;

3. investigate the behavior of m_π, f_π and other quantities around the crossover, where no obvious expansion applies.

6.2 Chiral Ward identities in the thermal field theory

We consider Euclideanized QCD with two flavors of degenerate quarks on the space $S^1 \times \mathbb{R}^3$, with the Matsubara cycle S^1 of length $\beta \equiv 1/T$. We label the Euclidean time direction as '0', while the direction 1, 2 and 3 are of infinite extent; we write $x_\perp \equiv (x_1, x_2)$. Unexplained notation follows [100]. The Dirac field is a flavor doublet, for instance $\bar{\psi}(x) = (\bar{u}(x) \ \bar{d}(x))$.

We define the vector current, axial current and the pseudoscalar density as

$$V_\mu^a(x) = \bar{\psi}\gamma_\mu \frac{\tau^a}{2}\psi(x), \qquad A_\mu^a(x) = \bar{\psi}\gamma_\mu\gamma_5 \frac{\tau^a}{2}\psi(x), \qquad P^a(x) = \bar{\psi}(x)\gamma_5 \frac{\tau^a}{2}\psi(x).$$
$$(6.2.1)$$

where $a \in \{1, 2, 3\}$ is an adjoint $SU(2)_{\text{isospin}}$ index and τ^a is a Pauli matrix. The PCAC (partially conserved axial current) relation reads

$$\partial_\mu A_\mu^a(x) = 2mP^a(x), \tag{6.2.2}$$

where m is the common mass of the up and down quark. (Eq. (6.2.2)) is valid in any on-shell correlation function. The Ward identities for two-point functions (valid for all x; see appendix E) that follow from the partial conservation of the axial current are

$$\langle A_\nu^a(0)\partial_\mu A_\mu^b(x)\rangle = 2m\langle A_\nu^a(0)P^b(x)\rangle \tag{6.2.3}$$

where we assume zero isospin chemical potential ($\langle V_\mu^a \rangle = 0 \; \forall a, \mu$), and

$$\langle P^a(0) \partial_\mu A_\mu^b(x) \rangle = -\frac{\delta^{ab}}{2} \langle \bar{\psi}\psi \rangle \delta^{(4)}(x) + 2m \langle P^a(0) P^b(x) \rangle. \tag{6.2.4}$$

6.2.1 Correlators in the massless theory

Space-time symmetries imply the following form for the $\langle P \vec{A} \rangle$ correlator,

$$\int dx_0 \; \langle P^a(0) \vec{A}^b(x) \rangle = \delta^{ab} g(r) \vec{e}_r, \qquad r = |\vec{x}|, \quad \vec{e}_r = \frac{\vec{x}}{r}. \tag{6.2.5}$$

Integrating Eq. (6.2.4) over $\int_0^\beta dx_0 \int_{|\vec{x}|<R} d^3x$, using the form (6.2.5) and Gauss's theorem, we get

$$g(r) = -\frac{\langle \bar{\psi}\psi \rangle}{8\pi r^2}. \tag{6.2.6}$$

This static correlator is thus fully determined by the chiral WI. Integrating Eq. (6.2.5) over an $x_3 = $ constant plane, one obtains

$$\int dx_0 \, d^2x_\perp \; \langle A_3^a(x) P^b(0) \rangle = -\frac{\delta^{ab}}{4} \, \text{sign}(x_3) \, \langle \bar{\psi}\psi \rangle, \qquad m = 0. \tag{6.2.7}$$

A second correlator can also be determined exactly in the massless theory. Indeed, for $x_0 \neq 0$ we have

$$\partial_0 \int_{r<R} d^3x \langle P^a(0) A_0^b(x) \rangle = -\int_{S_R} d\vec{\sigma} \cdot \langle P^a(0) \vec{A}^b(x) \rangle. \tag{6.2.8}$$

We assume that, when $\langle P^a(0) A^a(x) \rangle$ is expanded in a Fourier series in x_0, the non-constant modes fall off faster than $1/r^2$. If we then take the limit $R \to \infty$, using Eq. (6.2.5)–Eq. (6.2.6) we obtain

$$\partial_0 \int d^3x \; \langle P^a(0) A_0^b(x) \rangle = \delta^{ab} \frac{\langle \bar{\psi}\psi \rangle}{2\beta}. \tag{6.2.9}$$

Thus, since $\langle P^a(0) A_0^a(x) \rangle$ is odd in x_0 and in particular vanishes at $x_0 = \beta/2$,

$$\int d^3x \; \langle P^a(0) \, A_0^b(x) \rangle = \delta^{ab} \frac{\langle \bar{\psi}\psi \rangle}{2\beta} \left(x_0 - \frac{\beta}{2} \right). \tag{6.2.10}$$

6.2.2 Correlators at small quark mass: the pion decay constant and the GOR relation

The power law found in Eqs. (6.2.5–6.2.6) shows that P couples to a massless screening particle. The main idea in the following is to obtain the residue of the poles in the chiral limit, where they are determined by chiral Ward identities, and to use those at small but finite quark mass.

At finite quark mass, we expect[4]

$$\int dx_0 \, d^2x_\perp \, \langle A_3^a(x) P^b(0) \rangle \overset{|x_3| \to \infty}{=} \delta^{ab} \text{sign}(x_3) \, c(m) \, \exp(-m_\pi |x_3|), \qquad (6.2.11)$$

with $c(0) = -\frac{1}{4}\langle \bar{\psi}\psi \rangle$ in view of Eq. (6.2.7). Since the PCAC relation (6.2.2) implies

$$\partial_3 \int dx_0 \, d^2x_\perp \, \langle A_3^a(x) P^b(0) \rangle = 2m \int dx_0 \, d^2x_\perp \, \langle P^a(0) \, P^b(x) \rangle, \qquad (6.2.12)$$

we learn from (6.2.11) that close to the chiral limit,

$$\int dx_0 \, d^2x_\perp \, \langle P^a(0) \, P^b(x) \rangle = \delta^{ab} \frac{\langle \bar{\psi}\psi \rangle \, m_\pi}{8m} \exp(-m_\pi |x_3|). \qquad (6.2.13)$$

This equation shows that the correlation function of the pseudoscalar density admits a pole at m_π with residue $\frac{m_\pi^2 \langle \bar{\psi}\psi \rangle}{4m}$. Consequently, since the scalar propagator is $\frac{\exp(-m_\pi r)}{4\pi r}$ in three dimensions, we can write

$$\int dx_0 \, \langle P^a(0) \, P^b(x) \rangle \overset{r \to \infty}{=} \delta^{ab} \frac{m_\pi^2 \langle \bar{\psi}\psi \rangle}{4m} \frac{\exp(-m_\pi r)}{4\pi r}. \qquad (6.2.14)$$

Now returning to Eq. (6.2.11), multiplying both sides by $2m$ and using the PCAC relation shows that close to the chiral limit,

$$\int dx_0 \, d^2x_\perp \, \langle A_3^a(x) A_3^b(0) \rangle \overset{|x_3| \to \infty}{=} -\delta^{ab} \frac{m \langle \bar{\psi}\psi \rangle}{2m_\pi} \exp(-m_\pi |x_3|). \qquad (6.2.15)$$

We know that the correlator $\int dx_0 \langle P^a(0) \vec{A}^a(x) \rangle$ is non-zero at $m = 0$; therefore the coupling of P to the Goldstone boson cannot vanish at $m = 0$ — consistently

---

[4]This equation defines m_π.

with Goldstone's theorem. Since the residue at the pion pole in the correlator (6.2.14) cannot diverge in the chiral limit, we conclude that $m_\pi^2 \sim m$.

The scaling of m_π with the quark mass motivates the definition of f_π (for any value of the quark mass) at any temperature below T_C via

$$G_{\rm A}^{\rm s}(x_3, T, \mathbf{0}) = \int dx_0 \, d^2 x_\perp \langle A_3^a(x) A_3^b(0) \rangle = \frac{\delta^{ab}}{2} f_\pi^2 m_\pi e^{-m_\pi |x_3|}, \qquad |x_3| \to \infty. \tag{6.2.16}$$

Comparison with the chiral prediction (6.2.15) shows that

$$f_\pi^2 m_\pi^2 = -m \langle \bar\psi \psi \rangle, \qquad m \to 0, \tag{6.2.17}$$

in particular f_π has a finite, non-vanishing limit when $m \to 0$ as long as $\langle \bar\psi \psi \rangle$ is finite.

6.2.3   Spectral functions in the axial sector

Relation (6.2.10) shows that the pseudoscalar density and the axial charge density couple to a (real-time) massless excitation in the chiral limit. The goal is now to compute the dispersion relation of this excitation for small quark masses and spatial momenta. We recall the relation between the spectral function and the Euclidean correlator for the following cases,

$$\delta^{ab} G_{\rm P}(x_0, T, \mathbf{p}) \equiv \int d^3 x \, e^{i\mathbf{p}\mathbf{x}} \langle P^a(x) P^b(0) \rangle = \delta^{ab} \int_0^\infty d\omega \, \rho_{\rm P}(\omega, T, \mathbf{p}) \frac{\cosh(\omega(\beta/2 - x_0))}{\sinh(\omega\beta/2)} \tag{6.2.18}$$

$$\delta^{ab} G_{\rm AP}(x_0, T, \mathbf{p}) \equiv \int d^3 x \, e^{i\mathbf{p}\mathbf{x}} \langle P^a(x) A_0^b(0) \rangle = \delta^{ab} \int_0^\infty d\omega \, \rho_{\rm AP}(\omega, T, \mathbf{p}) \frac{\sinh(\omega(\beta/2 - x_0))}{\sinh(\omega\beta/2)} \tag{6.2.19}$$

$$\delta^{ab} G_{\rm A}(x_0, T, \mathbf{p}) \equiv \int d^3 x \, e^{i\mathbf{p}\mathbf{x}} \langle A_0^a(x) A_0^b(0) \rangle = \delta^{ab} \int_0^\infty d\omega \, \rho_{\rm A}(\omega, T, \mathbf{p}) \frac{\cosh(\omega(\beta/2 - x_0))}{\sinh(\omega\beta/2)} \tag{6.2.20}$$

The PCAC relation (6.2.2) implies

$$2m \, \rho_{\rm P}(\omega, T, \mathbf{0}) = -\omega \, \rho_{\rm AP}(\omega, T, \mathbf{0}), \tag{6.2.21}$$

$$\omega \, \rho_{\rm A}(\omega, T, \mathbf{0}) = 2m \, \rho_{\rm AP}(\omega, T, \mathbf{0}). \tag{6.2.22}$$

Equation (6.2.10), which is an exact expression in the chiral limit, shows that

$$\rho_{\mathrm{AP}}(\omega, T, \mathbf{0}) = -\frac{\langle \bar{\psi}\psi \rangle}{2} \delta(\omega) \qquad (m = 0). \qquad (6.2.23)$$

Since $P(x)$ and $A_0(x)$ couple to a massless excitation at $m = \mathbf{p} = 0$, they must also couple to an excitation when m and $\mathbf{p}$ are small but finite. In the following we assume that the imaginary part of the pole is negligible compared to its real part. An analysis in the hydrodynamic framework supports this assumption [98], as well as the chiral expansion around $T = 0$ [94]. We thus write the ansatz

$$\rho_{\mathrm{P}}(\omega, T, \mathbf{p}) = \mathrm{sign}(\omega) C(\mathbf{p}^2) \delta(\omega^2 - \omega_{\mathbf{p}}^2) + \dots \qquad (6.2.24)$$

for the spectral function of the pseudoscalar density. We must have $\omega_{\mathbf{p}} \to 0$ when $m, \mathbf{p} \to 0$ and the function $C(\mathbf{p}^2)$ is the residue of the pole in ω^2 and is non-vanishing when $m_\pi, \mathbf{p} \to 0$. We now show that the dispersion relation is of the form

$$\omega_{\mathbf{p}}^2 = u^2(m_\pi^2 + \mathbf{p}^2) + \mathrm{O}((\mathbf{p}^2)^2). \qquad (6.2.25)$$

The key observation is that we know the static correlator, Eq. (6.2.14); it is proportional to a three-dimensional scalar propagator. The static correlator can be expressed in terms of the spectral function as follows (see for instance [101]),

$$
\begin{aligned}
\int dx_0 \, \langle P^a(0) \, P^b(x) \rangle &= 2\delta^{ab} \lim_{\epsilon \to 0} \int \frac{d^3 p}{(2\pi)^3} e^{i\mathbf{p}\mathbf{x}} \int_0^\infty \frac{d\omega}{\omega} e^{-\epsilon\omega} \rho_{\mathrm{P}}(\omega, T, \mathbf{p}) \\
&= \delta^{ab} \int \frac{d^3 p}{(2\pi)^3} e^{i\mathbf{p}\mathbf{x}} \frac{C(\mathbf{p}^2)}{\omega_{\mathbf{p}}^2} + \dots
\end{aligned}
\qquad (6.2.26)
$$

Comparing with Eq. (6.2.14), we see that $\omega_{\mathbf{p}}^2$ must be proportional to $m_\pi^2 + \mathbf{p}^2$. Calling the proportionality factor u^2, we have proved Eq. (6.2.25) and we then have

$$C(\mathbf{p}^2) = -\frac{\langle \bar{\psi}\psi \rangle^2 \, u^2}{4 f_\pi^2} \qquad (6.2.27)$$

in the limit of small m_π and $\mathbf{p}$. Relations (6.2.21–6.2.22) now lead to

$$
\begin{aligned}
\rho_{\mathrm{AP}}(\omega, T, \mathbf{0}) &= -\frac{\omega_{\mathbf{0}} \langle \bar{\psi}\psi \rangle}{2} \delta(\omega^2 - \omega_{\mathbf{0}}^2) + \dots, & (6.2.28) \\
\rho_{\mathrm{A}}(\omega, T, \mathbf{0}) &= \mathrm{sign}(\omega) f_\pi^2 m_\pi^2 \, \delta(\omega^2 - \omega_{\mathbf{0}}^2) + \dots & (6.2.29)
\end{aligned}
$$

6.2.4   An exact sum rule for $\rho_{\mathrm{A}}(\omega, T, \mathbf{p})$

In appendix E, we show that the chiral Ward identities, together with the ultraviolet properties of the axial current correlator, imply the following exact sum rule for the axial current spectral function

$$\int_{-\infty}^{\infty} d\omega \, \omega \, \rho_{\mathrm{A}}(\omega, T, \mathbf{p})\Big|_0^T = -m\langle\bar{\psi}\psi\rangle\Big|_0^T. \qquad (6.2.30)$$

This equation is valid at vanishing chemical potential, but for any quark mass; it is to be compared to the corresponding sum rule in the vector channel ($\langle V_0 V_0 \rangle$, [102, 103]),

$$\int_{-\infty}^{\infty} d\omega \, \omega \, \rho_{\mathrm{V}}(\omega, T, \mathbf{p})\Big|_0^T = 0. \qquad (6.2.31)$$

The symbol $\{\ldots\}\Big|_0^T$ means that the zero-temperature contribution is subtracted. The subtraction is necessary to make the integral over frequency convergent. One easily checks that the pion-quasiparticle contribution to $\rho_{\mathrm{A}}(\omega, T, \mathbf{0})$ given in (6.2.29) and the $T = 0$ pion contribution satisfy the sum rule (6.2.30).

The sum rules (6.2.30) and (6.2.31) are complementary to the sum rules derived in [104] in the massless theory. For $m = 0$, Eq. (6.2.30)–Eq. (6.2.31) are consistent with the sum rule 'II-L' given in [104] upon substracting the $T = 0$ contributions.

6.2.5   Expressing u^2 in terms of static quantities

The parameter u can be obtained from $G_{\mathrm{A}}(x_0, T, \mathbf{0})$, at sufficiently small quark mass, by noting that

$$\omega_{\mathbf{0}}^2 = \frac{\partial_0^2 G_{\mathrm{A}}(x_0, T, \mathbf{0})}{G_{\mathrm{A}}(x_0, T, \mathbf{0})}\bigg|_{x_0=\beta/2} = -4m^2 \frac{G_{\mathrm{P}}(x_0, T, \mathbf{0})}{G_{\mathrm{A}}(x_0, T, \mathbf{0})}\bigg|_{x_0=\beta/2} \qquad (6.2.32)$$

The chiral Ward identities allow one to express $\partial_0^2 G_{\mathrm{A}}(x_0, T, \mathbf{0})$ in terms of f_π, m_π and $\omega_{\mathbf{0}}$. Using the spectral function (6.2.29), one obtains

$$\partial_0^2 G_{\mathrm{A}}(x_0, T, \mathbf{0}) = \frac{f_\pi^2 m_\pi^2 \omega_{\mathbf{0}}}{2} \frac{\cosh(\omega_{\mathbf{0}}(\beta/2 - x_0))}{\sinh(\omega_{\mathbf{0}}\beta/2)}. \qquad (6.2.33)$$

Inserting expression (6.2.33) into Eq. (6.2.32) yields the following algebraic equa-

tion for u,

$$u \sinh(u \, m_\pi \beta/2) = \frac{f_\pi^2 m_\pi}{2G_A(\beta/2, T, \mathbf{0})}. \tag{6.2.34}$$

This equation provides a way to extract the velocity u from Euclidean correlation functions. It is valid throughout the shaded region in Fig. 6.2, i.e. for sufficiently small quark masses and for all $T < T_c(m = 0)$. In the massless case, this relation is equivalent to the result of Son and Stephanov [98],

$$u^2 = \frac{f_\pi^2}{\int_0^\beta dx_0 \, G_A(x_0, T, \mathbf{0})} \qquad (m = 0). \tag{6.2.35}$$

The axial susceptibility appearing in the denominator of (6.2.35) however contains an ultraviolet divergence at any non-vanishing quark mass. It is therefore not practical to use in lattice calculations.

6.3   Lattice calculation (I): the scans C1 and D1

In this section we describe the numerical lattice QCD calculation of the temperature dependent parameters u and m_π that characterize the pion dispersion relation; see Eq. (6.2.25). All finite temperature correlation functions are measured on a set of dynamical gauge ensembles with two mass degenerate quark flavors covering a temperature range $150 \leq T \leq 235\,\text{MeV}$. We use the plaquette gauge action and the $O(a)$ improved Wilson fermion action with a non-perturbatively determined c_{sw} coefficient [43]. The configurations were generated using the MP-HMC algorithm [105,106] following the implementation described in [107] based on Lüscher's DD-HMC package [108].

Two scans in temperature were carried out on lattices of size 16×32^3, where the short direction is interpreted as time and therefore $T = 1/(16a)$ and the spatial extent is $L = 32a$. The gluon fields have periodic boundary conditions in all directions, while the quark fields are periodic in space and antiperiodic in time. The temperature is varied by varying the bare coupling g_0^2, which amounts to varying the lattice spacing at fixed 'aspect ratio' $LT = 2$. The scale setting was done via the Sommer parameter [46]. We use a quadratic interpolation of $\log(r/a)$ based on the data given in [50] to relate the lattice spacings at two values

of the bare coupling. The absolute scale setting, a/fm, is done using the value $r_0 = 0.503(10)\,\text{fm}$ [50].

6.3.1   The PCAC mass: line of constant physics

The two scans correspond to two quark masses of respectively about 8MeV and 15MeV, where the bare quark mass is tuned to keep the renormalized quark mass constant (see Fig. 6.3). The quark mass is given in the $\overline{\text{MS}}$ scheme at a scale $\mu = 2\text{GeV}$ for which we used the renormalization factors $Z_A(g_0^2)$ and $Z_P = 0.5184(53)$ from [50] as well as the conversion factor from the Schrödinger Functional (SF) to the $\overline{\text{MS}}$ scheme, which is $0.968(20)$ [50].

We use the standard definition for the quark mass that comes from the PCAC relation [109, 110]

$$m_{\text{PCAC}}(x_3) = \frac{1}{2} \frac{\int dx_0 d^2 x_\perp \left\langle \partial_3^{\text{imp}} A_3^{a,\text{imp}}(x) P^a(0) \right\rangle}{\int dx_0 d^2 x_\perp \left\langle P^b(x) P^b(0) \right\rangle}, \qquad x_\perp = (x_1, x_2), \qquad (6.3.1)$$

where in the improvement process

$$A_\mu^a \longrightarrow A_\mu^{a,\text{imp}} = A_\mu^a + ac_A \partial_\mu^{\text{imp}} P^a. \qquad (6.3.2)$$

The derivative $\partial_\mu^{\text{imp}}$ is the improved lattice discretized version of the derivative following [49]. The non-perturbatively calculated coefficient c_A was taken from [111]. Notice that since the PCAC relation is an operator identity, we are free to choose the direction in which we define the quark mass – any dependence on the direction must therefore amount to a discretization error. On our lattices, the spatial direction is longer, so measuring along these directions we obtain a longer plateau and thus, smaller errors. The extraction is carried out by performing a fit to a constant in the range where a plateau is observed. Within errors the PCAC masses measured in the time and in spatial directions agree.

The two scans, called C1 and D1, have respectively pseudocritical temperatures of $T_c = 211(5)\,\text{MeV}$ and $T_c = 193(7)\,\text{MeV}$ [99]. For instance, in Fig. 6.3, we observe that in scan C1, our renormalized quark mass in physical units is approximately constant up to $T = 211\text{MeV}$ where the phase transition to the deconfined phase is estimated to occur. This means that the ensembles presented in Tabs. 6.2 and 6.3
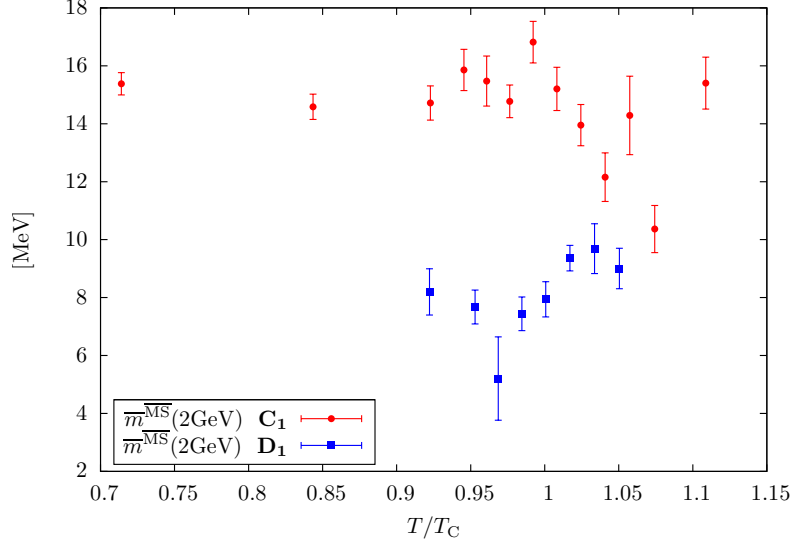
Figure 6.3: Renormalized quark mass in physical units in the $\overline{\text{MS}}$ scheme for both temperature scans (C1 and D1). For the C1 scan, $T_c = 211(5)\,\text{MeV}$, and for D1, $T_c = 193(7)\,\text{MeV}$.

follow to a good approximation 'lines of constant physics' and can be interpreted as temperature scans at fixed quark mass.

Statistical errors on the observables are calculated using the jackknife method. In plots, only the statistical error from our simulations are displayed; the error from renormalization factors and the scale setting uncertainty should be added in quadrature to obtain the full uncertainty.

6.3.2   Basic observables

In this section we describe the calculation of the following observables:

- the midpoint of the axial charge correlator in the time direction, $G_{\text{A}}(\beta/2, T, \mathbf{0})$;

- the midpoint of the pseudoscalar correlator in the time direction, $G_{\text{P}}(\beta/2, T, \mathbf{0})$;

- the screening pion mass m_π;

- the screening pion decay constant f_π.

The values of the correlators $G_{\text{A}}(\beta/2, T, \mathbf{0})$ and $G_{\text{P}}(\beta/2, T, \mathbf{0})$ at $x_0 = \beta/2$ are displayed in Fig. 6.4. While the former only exhibits a mild temperature dependence, the latter quantity is strongly temperature dependent. Since $\partial_0^2 G_{\text{A}}(x_0) =$

$-4m^2 G_{\mathrm{P}}(x_0)$, this observation means that the axial charge correlator becomes flatter as a function of x_0. It shows that the spectral density $\rho_{\mathrm{A}}(\omega, T, \mathbf{0})$ must concentrate around the origin as the temperature rises.

Extraction of m_π

In order to extract the 'screening' pion mass, we compute the symmetrized pseudoscalar-pseudoscalar screening Euclidean correlator along a spatial direction,

$$\delta^{ab}\, G_{\mathrm{P}}^{\mathrm{s}}(x_3) = \int dx_0 d^2 x_\perp \left\langle P^a(x) P^b(0) \right\rangle, \qquad G_{\mathrm{P}}^{\mathrm{s}}(x_3) \stackrel{|x_3| \to \infty}{\sim} e^{-m_\pi |x_3|} \qquad (6.3.3)$$

At long distances, it is dominated by the lowest lying state with pseudoscalar quantum numbers, which we call the 'screening pion'. In practice, a two state fit to the correlation function via Levenberg-Marquardt's method [56] is performed using an ansatz of the form

$$G_{\mathrm{P}}^{\mathrm{s}}(x_3) = A_1^P \cosh[m_1^P(x_3 - L/2)] + A_2^P \cosh[m_2^P(x_3 - L/2)]. \qquad (6.3.4)$$

To initialize the fit-routine we use as input parameter for $m_1^P \doteq m_\pi$ an averaged value of the 'coshmass' $m_{\mathrm{cosh}}(x_3)$ defined as the positive root of the following equation,

$$\frac{G_{\mathrm{P}}^{\mathrm{s}}(x_3)}{G_{\mathrm{P}}^{\mathrm{s}}(x_3 + a)} = \frac{\cosh[m_{\mathrm{cosh}}(x_3 + a/2)(x_3 - L/2)]}{\cosh[m_{\mathrm{cosh}}(x_3 + a/2)(x_3 + a - L/2)]} \; ; \qquad (6.3.5)$$

In order to be sure that the ground state is isolated one can repeat the fit to the correlation function for different fit windows, leaving out points that are furthest away from the middle point $x_3 = L/2$ of the correlator. We choose for the m_π result quoted in table 6.5 a value corresponding to a small $\chi^2/\mathrm{d.o.f}$ which is stable under small variations of the fit window. The result for m_π obtained in this way is close, in value and in its uncertainty, to m_{cosh} around $x_3 = L/2$; see Fig. 6.5.

The temperature dependence of m_π is illustrated in the left panel of Fig. 6.6. We observe that the correlation length in the thermal medium becomes shorter as the temperature increases, and is about half as long at the crossover as it is at zero-temperature.
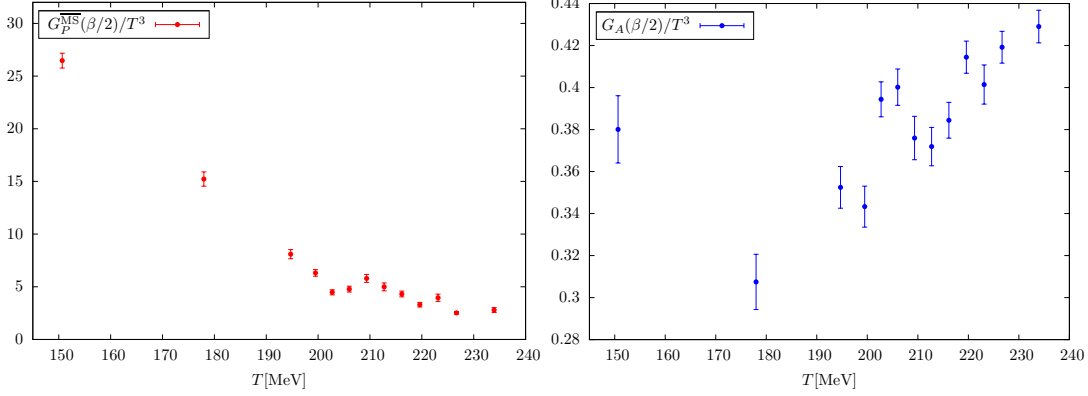
Figure 6.4: Midpoints of the renormalized correlators $G_{\mathrm{A}}(x_0)$ and $G_{\mathrm{P}}(x_0)$. The former was renormalized via multiplication with Z_{A}^2, the latter via multiplication with Z_{P}^2 as well as the conversion factor from the SF to the $\overline{\mathrm{MS}}$ scheme at the scale $\mu = 2\,\mathrm{GeV}$. All data from the C1 temperature scan.

Extraction of f_π

We extract f_π from the correlation function

$$\delta^{ab}\, G_A^{\mathrm{s}}(x_3) = \int dx_0 d^2x_\perp \left\langle A_3^{a,\mathrm{imp}}(x) A_3^{b,\mathrm{imp}}(0) \right\rangle \stackrel{|x_3|\to\infty}{=} \frac{\delta^{ab}}{2} f_\pi^2 m_\pi e^{-m_\pi x_3} \qquad (6.3.6)$$

Because of the noisier behavior of this correlator, it turns out that the fit to this correlation function is more stable using a 1-state-fit rather than a 2-state-fit. Since G_A^{s} is symmetric around $x_3 = L/2$ we use an ansatz of the form

$$G_A^{\mathrm{s}}(x_3) = A_1^A \cosh[m_1^A(x_3 - L/2)]. \qquad (6.3.7)$$

For stability reasons we put $m_1^A = m_\pi$ by hand since this quantity is already known from the $G_{\mathrm{P}}^{\mathrm{s}}$-fit. This reduces the number of parameters to one. By repeating the procedure for different fit windows as explained above, we select the final value for A_1^A by choosing a fit which has a low $\chi^2/\mathrm{d.o.f.}$ The relation between A_1^A and f_π reads

$$f_\pi^2 = \frac{2\,A_1^A \sinh(m_\pi L/2)}{m_\pi}. \qquad (6.3.8)$$

The temperature dependence of f_π in the C1 temperature scan is displayed in the right panel of Fig. 6.6. We observe a reduction of f_π as the temperature increases, reaching a value of about one third its zero-temperature value around the crossover.
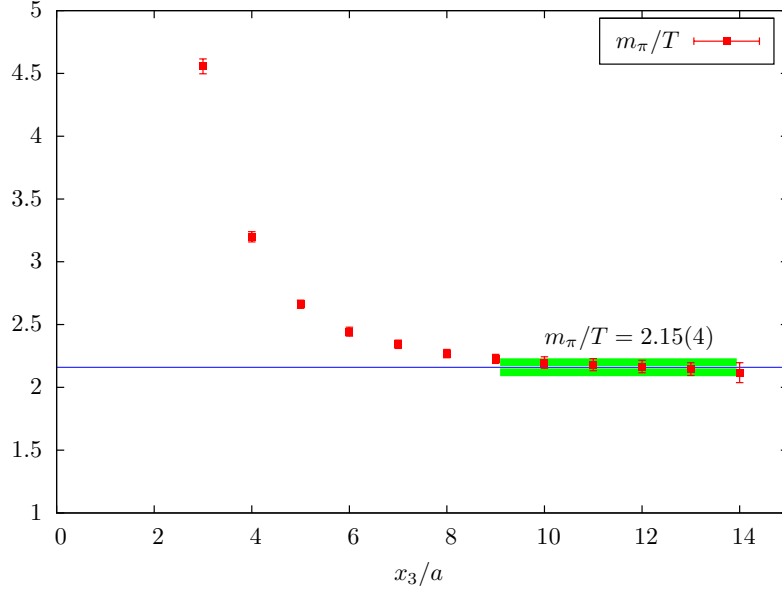
Figure 6.5: Example of an effective-mass plot showing $m_{\mathrm{cosh}}(x_3 + a/2)$ for the pseudoscalar density two-point function in the x_3-direction in the C1 scan at $T = 150\,\mathrm{MeV}$. The result of the fit to the correlation function is represented by a (1σ) band. Here the chosen fit-window was 26, which corresponds to ignoring the three points closest to each operator, and the (uncorrelated) $\chi^2/\mathrm{d.o.f}$ amounts to 0.05.

Chiral condensate $\langle \bar{\psi}\psi \rangle$

Using the Gell-Mann–Oakes–Renner relation [112], one can define an effective chiral condensate as follows (see Eq. (6.1.4)),

$$\langle \bar{\psi}\psi \rangle^{\overline{\mathrm{MS}}}_{\mathrm{GOR}} = -\frac{f_\pi^2 m_\pi^2}{\overline{m}^{\overline{\mathrm{MS}}}}. \tag{6.3.9}$$

Since $m_\pi \sim T$ and $f_\pi \sim m$ above T_c, $\langle \bar{\psi}\psi \rangle^{\overline{\mathrm{MS}}}_{\mathrm{GOR}}$ is of order m above T_c; at high temperatures, it is expected to grow as mT^2.

The behavior of the effective chiral condensate is displayed in Fig. 6.7. We find it to be weakly temperature dependent around T_c. It illustrates how smooth the crossover is at the quark mass used in the temperature scan C1: around $T = 200\,\mathrm{MeV}$, $|\langle \bar{\psi}\psi \rangle^{\overline{\mathrm{MS}}}_{\mathrm{GOR}}|^{1/3}$ only appears to be about 10% lower than at zero temperature.
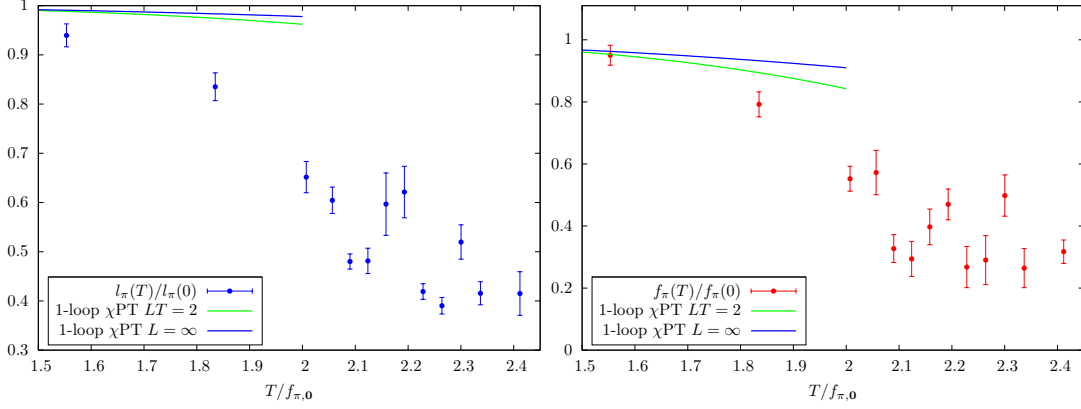
Figure 6.6: Inverse screening mass $l_\pi \equiv m_\pi^{-1}$ (left) and screening pion 'decay constant' (right) in the C1 scan, divided by the same quantity at $T \simeq 0$ extracted from the A5 ensemble. The displayed error bars represent the statistical errors originating from the ensembles of the C1 scan and from ensemble A5.

6.3.3   Lattice estimators for the pion velocity

We showed that, at sufficiently small quark mass, the axial charge correlator is dominated by a light quasiparticle and that its mass $\omega_\mathbf{0}$ is given by Eq. (6.2.32). With $\omega_\mathbf{0} = u m_\pi$, the following estimator for u can be defined,

$$u_m^2 = -\frac{4m^2}{m_\pi^2} \left.\frac{G_\mathrm{P}(x_0, T, \mathbf{0})}{G_\mathrm{A}(x_0, T, \mathbf{0})}\right|_{x_0=\beta/2}. \tag{6.3.10}$$

We introduce a second estimator for u based on Eq. (6.2.34),

$$u_f \sinh(u_f m_\pi \beta/2) = \frac{f_\pi^2 m_\pi}{2G_\mathrm{A}(\beta/2, T, \mathbf{0})}. \tag{6.3.11}$$

It should be noticed that the pion velocity is a renormalization group invariant quantity and thus, does not require any renormalization. The results for u_f and u_m are shown in Fig. 6.8. We observe a significant reduction of both quantities from unity, pointing to a pion 'velocity' well below the speed of light. However, whether the interpretation is valid for $T \gtrsim 160\,\mathrm{MeV}$ is questionable.

One way to test the validity of the chiral effective theory predictions is the following. The chiral EFT makes a prediction for $G_\mathrm{P}(\beta/2)$ in terms of f_π, m_π and $G_\mathrm{A}(\beta/2)$; see Eq. (6.2.32)–Eq. (6.2.33). Testing whether $u_f/u_m = 1$ is equivalent to testing this prediction. The estimator u_m is based on the dominance of the pion
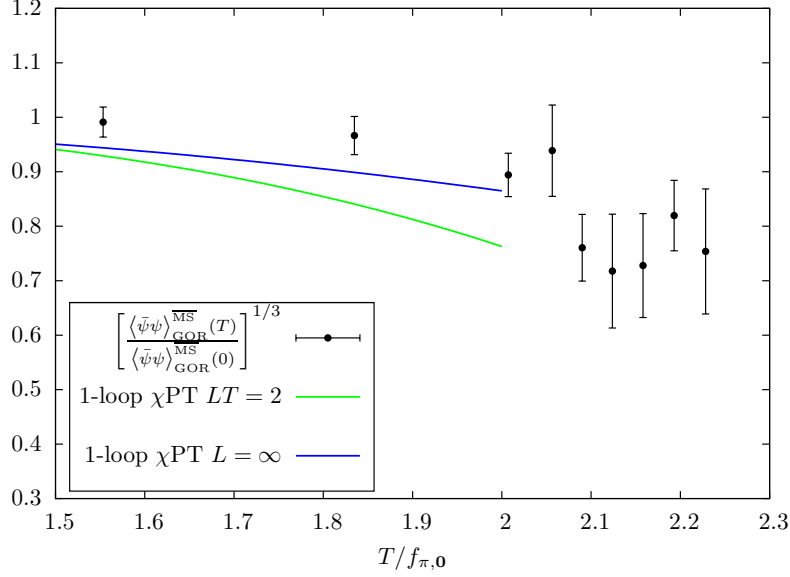
Figure 6.7:   Effective chiral condensate defined from the GOR relation, divided by its $T = 0$ counterpart, in the temperature scan C1. In addition, the predictions of [113] both for the infinite volume limit and for our finite lattice volume are displayed. The temperature is given in units of the zero-temperature decay constant $f_{\pi,\mathbf{0}}$.

contribution in the correlators G_A and G_P at $x_0 = \beta/2$; the estimator u_f is based on assuming that the residue is given by the screening quantities (as predicted by the chiral effective theory), $\mathrm{Res}(\omega_{\mathbf{0}}) = f_\pi^2 m_\pi^2$, and the dominance of the pion contribution in G_A only. The dominance in G_A is less strong an assumption than the assumption that the pion dominates G_P, since their spectral functions are related by $\rho_P(\omega) = -\frac{\omega^2}{4m^2}\rho_A(\omega)$ at zero spatial momentum. It is worth noting that at high temperatures, well in the deconfined phase, $u_m = \mathrm{O}(m^2/T^2)$, while $u_f = \mathrm{O}(m/T)$, so that u_f/u_m is expected to grow with temperature. In the lattice data displayed in the right panel of Fig. 6.8 we indeed observe that u_f/u_m grows above unity. Thus it is at the lowest-temperature ensemble in the C1 temperature scan that we are most confident in the interpretation of u_f as the pion quasiparticle velocity.

Figure 6.8: Left: The two estimators of the pion velocity in the C1 scan. Right: Ratio of the estimators, which serves as a test of the chiral prediction (6.2.33).

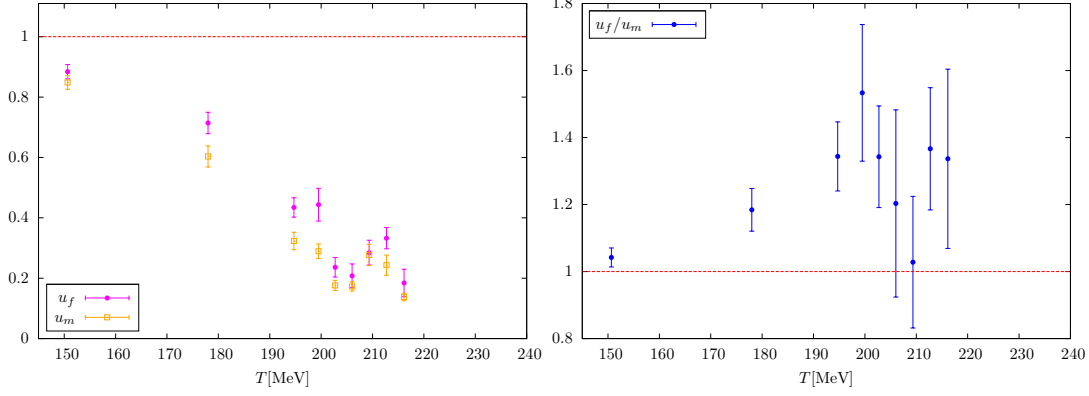## 6.3.4   The $T \simeq 0$ ensemble A5 and test of chiral perturbation theory predictions

In addition to the analysis of thermal ensembles, it is interesting to compute the same observables on a corresponding zero-temperature ensemble. One reason is that we obtain the reference values of $\omega_{\mathbf{0}}$, m_π and f_π at $T = 0$; the thermal modification of these quantities can be compared with the predictions of chiral perturbation theory [113, 114]. A second, practical reason is to check the validity of our estimators for $u(T)$, since $\lim_{T \to 0} u(T) = 1$. We therefore analyze the CLS ensemble labelled A5 in [50]. All ensemble parameters coincide with the lowest-temperature ensemble in the C1 scan; the only difference is the lattice extent in the time direction, which is 64 instead of 16. The bare parameters and the computed observables are summarized in Table 6.4.

In contrast to the thermal ensembles, here we are able to directly extract the mass of the pion propagating in the temporal direction, which we denote by $\omega_{\mathbf{0}}$. It is extracted by fitting to a constant the coshmass of the pseudoscalar-pseudoscalar correlator, where a clear plateau is observed. The pion decay constant $f_{\pi,\mathbf{0}}$ is calculated by fitting the amplitude of the axial charge correlator $G_{\mathrm{A}}(x_0)$. The effective quark condensate $|\langle \bar{\psi}\psi \rangle^{\overline{\mathrm{MS}}}_{\mathrm{GOR},\mathbf{0}}|^{1/3}$ given in Table 6.4 follows the definition (6.3.9), except that m_π was replaced by $\omega_{\mathbf{0}}$ and f_π by $f_{\pi,\mathbf{0}}$.

We find that the extraction of the pseudoscalar mass in the spatial and in the temporal direction give the same answer within two standard deviations. The esti-

mators u_f and u_m are both compatible with unity within two standard deviations; this adds to our confidence that the estimators work as expected in practice.

We use m_π and f_π to normalize the corresponding quantities at finite temperature in Fig. 6.6. This allows for the most natural comparison of the predictions of one-loop chiral perturbation theory [113], an expansion around $(T = 0, m = 0)$, with the lattice data. We display both the prediction for the infinite-volume system and for the finite-volume system; details are given in appendix G. At the lowest temperature in the C1 scan ($T \simeq 150\,\text{MeV}$), the prediction agrees very well with the lattice result for f_π. The central value of the correlation length m_π^{-1} lies somewhat lower than the corresponding chiral prediction, but still within two standard deviations. However, on the next ensemble, at $T \simeq 177\,\text{MeV}$, the lattice data clearly deviates from the chiral prediction. From this temperature onwards, both m_π and f_π deviate substantially from their $T = 0$ counterparts. One-loop chiral perturbation theory predictions at $T \gtrsim 170\,\text{MeV}$ appear to be unreliable.

We remark that the prediction for $f_\pi(T)/f_\pi(0)$ does not involve directly the relation between the quark mass and the pion screening mass. The GOR-condensate, however, does; it is compared to the chiral prediction in Fig. 6.7. Here the quantities combine to give a result which is only mildly temperature-dependent. Correspondingly the chiral prediction lies numerically quite close to the data points. The prediction for the GOR condensate seems to be more robust than the predictions for m_π and f_π taken separately; it works, at our current level of accuracy, essentially up to the transition temperature.

We can in principle compare the pion quasiparticle mass, computed as $\omega_{\mathbf{0}}(T) = u(T)m_\pi(T)$, with the two-loop predictions of chiral perturbation theory [94, 95]. At $T = 150\,\text{MeV}$ in the C1 scan, we find

$$\frac{\omega_{\mathbf{0}}(T)}{\omega_{\mathbf{0}}(0)} = 0.97(4), \tag{6.3.12}$$

where $\omega_{\mathbf{0}}(T = 0) = 294(4)\,\text{MeV}$. Thus the thermal shift of the pion quasiparticle mass appears to be very small. At the same temperature, but at the physical quark mass, the corresponding quantity is predicted to be about 0.86 at the two-loop level [94]; we note that there is a change in the sign of $\frac{\omega_{\mathbf{0}}(T)}{\omega_{\mathbf{0}}(0)} - 1$ between the one-loop and the two-loop result at this temperature. Clearly one expects the thermal effect on $\omega_{\mathbf{0}}$ to be smaller at heavier quark masses. Thus the lattice

results are not obviously inconsistent with the chiral prediction. We postpone a more detailed comparison of lattice results for the quantity $\omega_\mathbf{0}$ (and indeed $\omega_\mathbf{p}$) with chiral perturbation theory to a future study.

The relative success of the one-loop chiral prediction for the thermal effect on the 'chiral' quantities m_π, f_π and $\langle\bar\psi\psi\rangle_{\mathrm{GOR}}$ at

$$T = 150\,\mathrm{MeV} \simeq 0.7 T_c \qquad (\overline{m}^{\overline{\mathrm{MS}}} \simeq 15\,\mathrm{MeV}) \tag{6.3.13}$$

is somewhat unexpected when one considers that the energy density, say, for physical quark masses is completely dominated by hadrons more massive than pions [87, 114]. The surprise at the quark mass used here is, in a sense, that chiral quantities are still affected below the 10% level by the thermal effects. However, the effect of the thermal medium increases rapidly above $T = 150\,\mathrm{MeV}$.

6.3.5 Quark mass dependence of m_π and f_π around the pseudocritical temperature

The scan D1 at the light quark mass is more concentrated around the pseudocritical temperature. Therefore we can only discuss the quark mass dependence of the observables discussed so far in the crossover region; see Fig. 6.9. We find that, if m_π/T and f_π/T are viewed as a function of T/T_c, where T_c is the quark-mass dependent pseudocritical temperature, the quark mass dependence is very mild. In this respect we are far from the deeply chiral regime where the screening pion mass exhibits a sudden steep rise at T_c, from a low value below T_c of order $\sqrt{m}$.

A look at Table 6.5–6.6 shows that the effective condensate appears to be quite insensitive to the quark mass up to $T = 195\,\mathrm{MeV}$, which corresponds to the pseudocritical temperature at the lower quark mass. In other words, the GOR relation is satisfied within the uncertainties, in spite of the fact that, at fixed temperature, the pion mass m_π does not decrease with the quark mass between scan C1 and scan D1.
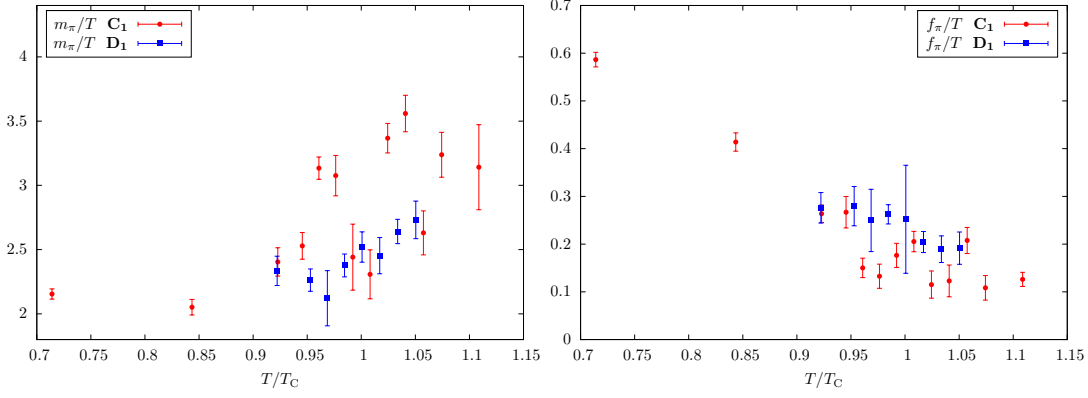
Figure 6.9: Temperature dependence of the pion screening mass and the associated decay constant, for two quark masses (C1 and D1 scans). The temperature is given in units of the pseudocritical temperature at the corresponding quark mass.

6.4   Axial Form factors at non-zero momentum and its residues

In appendix E.2, we provide a decomposition in momentum space of the Lorentz structure of the two-point functions of the axial current. For a general momentum p, they are entirely described by four 'form factors', which in the rest frame of the thermal medium are functions of p_0 and $\mathbf{p}^2$. At zero-temperature, the four functions reduce to two functions of p^2, one longitudinal and one transverse. The partially-conserved axial current (PCAC) relation relates the two-point function $\langle P^a(x) P^b(0) \rangle$ of the pseudoscalar density, as well as the $\langle A^a_\mu(x) P^b(0) \rangle$ correlation functions to the aforementioned form factors. They are related by Fourier transformations to the form factors defined in appendix E.2, for instance

$$G^{\mathrm{s}}_A(x_3, T) = \int \frac{dp_3}{2\pi} \, e^{-ip_3 x_3} \, \Pi^{\mathrm{L,l}}(0, p_3^2). \tag{6.4.1}$$

The correlators $G_A(x_0, T, \mathbf{0})$ and $G^{\mathrm{s}}_A(x_3, T)$ are only sensitive to the longitudinal form factor $\Pi^{\mathrm{L,l}}$; these were the cases considered so far. At non-vanishing momentum however, the correlator $G_A(x_0, T, \mathbf{p})$ is sensitive to three independent form factors $\Pi^{\mathrm{T,l}}$, Π^{M} and $\Pi^{\mathrm{L,l}}$.

At long distances, the screening correlator $G^{\mathrm{s}}_A(x_3, T)$ is given by

$$G^{\mathrm{s}}_A(x_3, T) \stackrel{|x_3| \to \infty}{=} \frac{1}{2} f_\pi^2 m_\pi \, e^{-m_\pi |x_3|}, \tag{6.4.2}$$

which defines the screening pion mass m_π and the associated decay constant[5] f_π. The Gell-Mann–Oakes–Renner relation

$$f_\pi^2 m_\pi^2 = -m\langle\bar\psi\psi\rangle \tag{6.4.3}$$

holds to leading order in the chiral expansion. From Eqs. (6.4.1) and (6.4.2), the low-momentum analytic structure of the longitudinal form factor $\Pi^{\mathrm{L,l}}$ reads

$$\Pi^{\mathrm{L,l}}(0,\mathbf{p}^2) = \frac{f_\pi^2 m_\pi^2}{\mathbf{p}^2 + m_\pi^2}, \qquad \mathbf{p}\to 0. \tag{6.4.4}$$

More generally, expanding the denominator in the frequency,

$$\mathbf{p}^2 + m_\pi^2 \quad \longrightarrow \quad \mathbf{p}^2 + m_\pi^2 + \frac{1}{u^2}\omega_n^2 + \dots, \tag{6.4.5}$$

it follows that a quasiparticle (pole in the retarded correlator as a function of frequency) with the dispersion relation [97, 98]

$$\omega_{\mathbf{p}} = u(T)\sqrt{m_\pi^2 + \mathbf{p}^2} \tag{6.4.6}$$

exists at low momenta as already pointed out in Eq. (6.1.2)[6]. The remarkable aspect is that the parameter u determines both the (real part of the) dispersion relation of the quasiparticle and the ratio of the quasiparticle mass to the screening mass. A graphical interpretation of the dual role of the parameter u is given in Fig. 6.10. Here the trajectory in the frequency-momentum plane of a pole in the retarded correlator of the pseudoscalar density[7] corresponds to a static screening state at $\mathbf{p}^2 = -m_\pi^2$, and to a real-time quasiparticle at small positive $\mathbf{p}^2$. So far, good agreement was found between the estimators u_f and u_m at $T \simeq 150\,\mathrm{MeV}$ for a zero-temperature pion mass of $305\,\mathrm{MeV}$. Any departure of u from unity clearly represents a breaking of Lorentz invariance due to thermal effects. The next goal is to test whether the parameter u determined from the ratio of the quasiparticle to the screening mass, as in [12], really does predict the dispersion

---

[5]The normalization convention is such that at zero temperature $f_\pi \approx 92\,\mathrm{MeV}$.

[6]In this argument, the imaginary part of the frequency-pole is neglected. A more sophisticated argument is required to show that the damping rate of the pion quasiparticle is indeed parametrically subleading [98].

[7] Recall that the momentum-space Euclidean correlator $G_E(\omega_n, \mathbf{p})$ is related to the retarded correlator via $G_R(i\omega_n, \mathbf{p}) = G_E(\omega_n, \mathbf{p})$ for $\omega_n \geq 0$ [12] as already stated in Eq. (2.3.30).
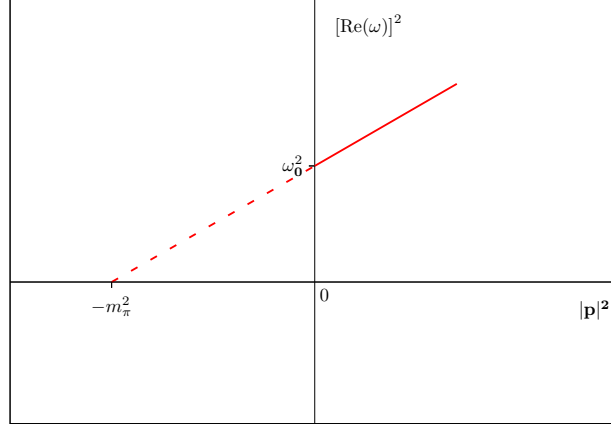
Figure 6.10: Trajectory in $(\omega, \mathbf{p})$-plane of the pion pole in the pseudoscalar re-tarded correlator. At negative $\mathbf{p}^2$ the pole corresponds to the pion screening mass, at positive $\mathbf{p}^2$ it corresponds to the pion quasiparticle. The slope is the value of $u^2(T)$.

relation of the quasiparticle, as in Eq. (6.1.2). In order to carry out this goal, we perform an analysis of the time-dependent Euclidean correlator $G_A(x_0, T, \mathbf{p})$ at non-zero momentum in terms of the spectral function ρ_A. As already pointed out in Eq. (6.2.20), they are related as follows,

$$G_A(x_0, T, \mathbf{p}) = \int_0^\infty d\omega \, \rho_A(\omega, T, \mathbf{p}) \frac{\cosh(\omega(\beta/2 - x_0))}{\sinh(\omega\beta/2)}. \tag{6.4.7}$$

First we recall that at zero temperature, the Lorentz structure of the axial-current two-point function implies the following momentum dependence of the pion pole contribution,

$$G_A(x_0, T = 0, \mathbf{p}) \overset{|x_0| \to \infty}{\sim} \operatorname{Res}(\omega_{\mathbf{p}}^0) \frac{e^{-\omega_{\mathbf{p}}^0 |x_0|}}{2\omega_{\mathbf{p}}^0} \tag{6.4.8}$$

where the residue is here given by

$$\operatorname{Res}(\omega_{\mathbf{p}}^0) = (f_\pi^0 \omega_{\mathbf{p}}^0)^2, \qquad \omega_{\mathbf{p}}^0 = (\mathbf{p}^2 + (\omega_{\mathbf{0}}^0)^2)^{1/2}. \tag{6.4.9}$$

In terms of the spectral functions, this correlator corresponds to

$$\rho_A(\omega, T = 0, \mathbf{p}) = \operatorname{Res}(\omega_{\mathbf{p}}^0) \, \delta(\omega^2 - (\omega_{\mathbf{p}}^0)^2) + \dots \tag{6.4.10}$$

At the other end of the spectrum, in the high frequency region, a leading-order perturbative calculation (see for instance [14]) yields

$$\rho_{\text{A}}(\omega, T, \mathbf{p}) = \theta(\omega^2 - 4m^2 - \mathbf{p}^2)\frac{N_c}{24\pi^2}(\mathbf{p}^2 + 6m^2), \qquad \omega \to \infty. \tag{6.4.11}$$

We note that at non-zero momentum, the correlator $G_A(x_0, T = 0, \mathbf{p})$ receives contributions from axial vector mesons via the transverse form factor (see appendix E.2),

$$G_A(x_0, T = 0, \mathbf{p}) = \int \frac{dp_0}{2\pi} e^{-ip_0 x_0} \left[\frac{\mathbf{p}^2}{p_0^2 + \mathbf{p}^2}\Pi^{\text{T}}(p_0^2 + \mathbf{p}^2) + \frac{p_0^2}{p_0^2 + \mathbf{p}^2}\Pi^{\text{L}}(p_0^2 + \mathbf{p}^2) \right]. \tag{6.4.12}$$

The spectral functions associated with the form factors Π^{T} and Π^{L} are measured experimentally in τ decays [115]. The most prominent excitation in the transverse spectral function is the $a_1(1260)$ meson, while the longitudinal spectral function is dominated by the pion. Since Π^{T} describes by itself the two-point function of spatial components of the axial current at vanishing spatial momentum, it cannot contain the pion pole. The latter is entirely contained in the form factor Π^{L}.

At finite temperature, the pion pole appears in all three form factors contributing to $G_A(x_0, T, \mathbf{p})$; they are given explicitly in appendix (E.2). In the limit $T \to 0$, one of the three form factors turns into Π^{T}, one turns into Π^{L} and the third one vanishes (sec. E.2.2). Therefore the pion contribution to the first form factor must vanish in the limit $T \to 0$, in view of the remarks above, and indeed, we find it to be proportional to $(1 - u^2)$ (recall that $\lim_{T \to 0} u(T) = 1$ by Lorentz symmetry). Altogether, the pion contribution to the spectral function ρ_{A} is predicted to have the form $\rho_{\text{A}}(\omega, T, \mathbf{p}) = \text{Res}(\omega_{\mathbf{p}})\delta(\omega^2 - \omega_{\mathbf{p}}^2)$, with the dispersion relation given by Eq. (6.1.2) and the residue by (see appendix E.3)

$$\text{Res}(\omega_{\mathbf{p}}) = f_\pi^2(m_\pi^2 + \mathbf{p}^2). \tag{6.4.13}$$

For later use we also define the pion quasiparticle decay constant f_π^t via

$$\text{Res}(\omega_{\mathbf{0}}) = (f_\pi^t \, \omega_{\mathbf{0}})^2. \tag{6.4.14}$$

The contribution to the Euclidean correlator then reads

$$G_A(x_0, T, \mathbf{p}) = \frac{\text{Res}(\omega_{\mathbf{p}})}{2\omega_{\mathbf{p}}} \frac{\cosh(\omega_{\mathbf{p}}(\beta/2 - x_0))}{\sinh(\omega_{\mathbf{p}}\beta/2)} + \dots . \qquad (6.4.15)$$

Whether the residue determined through fits to lattice correlation functions agrees with Eq. (6.4.13) provides a cross-check that the low-energy effective description is working.

6.5   Lattice calculation (II): a fine thermal ensemble at $T = 170\text{MeV}$

In order to study the impact of systematic errors in our lattice calculations, we performed the analysis concerning the non-vanishing momentum euclidean correlators on a superior ensemble in terms of cut-off effects and finite volume corrections (compared to the calculation presented in Sec. 6.3). We describe the analysis performed on a finite temperature ensemble of size 24×64^3 with two degenerate dynamical light flavors. The short direction is interpreted as time and therefore the temperature is $T = 1/24a = 169(3)\text{MeV}$ while the spatial extent amounts to $L = 64a = 3.1\,\text{fm}$.

Like in the previous Lattice calculation (see Sec. 6.3) we use the Wilson plaquette action [36] and the O(a) improved Wilson fermion action with a non-perturbatively determined c_{sw} coefficient [43]. Again, the configurations were generated using the MP-HMC algorithm [105] following the implementation described in [107] based on Lüscher's DD-HMC package [108]. In addition, we use a 128×64^3, effectively zero temperature ensemble that was made available to us through the CLS effort (labelled as O7 in [50]) with all bare parameters identical to our finite temperature ensemble. The pion mass takes a value of $m_\pi = 270\text{MeV}$ [50] such that $m_\pi L = 4.2$. This represents an advantage concerning the validity of the chiral expansion since we move to slighter smaller values of the quark mass. This additional zero temperature test ensemble allows us to compare thermal observables in a straightforward manner with their corresponding "effective zero-temperature" value calculated in the O7 ensemble (see Sec. 6.5.2).

In order to check that our thermal ensemble indeed yields the same physical quark mass as its corresponding zero-temperature counterpart (O7), we use the

definition of the quark mass based on the PCAC (partially conserved axial current) relation already defined in Eq. (6.3.1) and Eq. (6.3.2). The extraction can be carried out by performing a fit to a constant in the range where a plateau is observed. Its central value and error, given in Table 6.7, are in very good agreement with the independent determination quoted in [116].
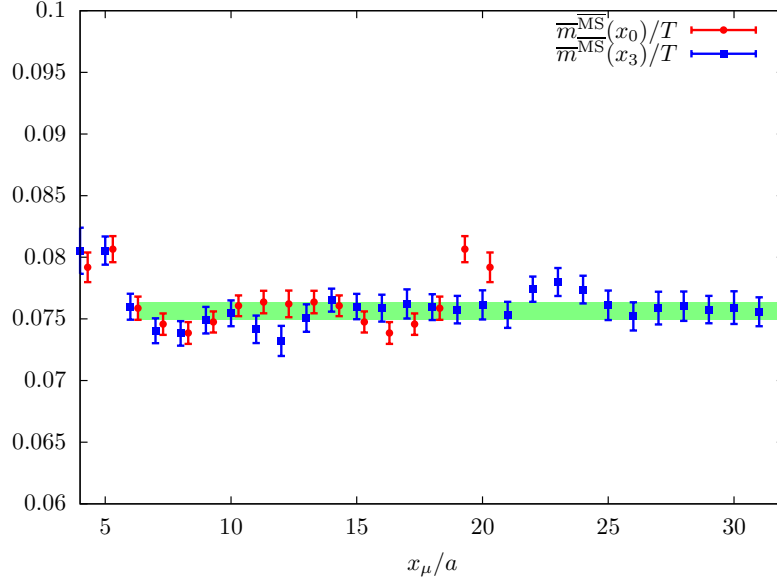
Figure 6.11: The PCAC mass for the 24×64^3 thermal ensemble. The renormalization factors Z_A and Z_P are included, as well as the conversion factor from the SF to $\overline{\text{MS}}$ at a scale of $\mu = 2\text{GeV}$, which amounts to 0.968(20) [50]. We also plot the result along the x_0-direction to show that indeed both are compatible. This can be interpreted as a check that cutoff effects are indeed small for this value of the lattice spacing.

6.5.1 Pseudoscalar and axial-vector correlators at $\mathbf{p} \neq 0$

In the thermal ensemble we are analyzing here, we have $\overline{m}^{\overline{\text{MS}}}(\mu = 2\text{GeV}) = 12.8(1)\text{MeV}$ (see Table 6.7), and therefore expect a slightly lower value of the transition temperature. Nevertheless, this should not affect the applicability of the chiral expansion around $(T, m = 0)$ with $T < T_C$.

We use the correlators $G_A(x_0, T, \mathbf{p})$ and $G_P(x_0, T, \mathbf{p})$ as well as the corresponding screening correlators $G_A^s(x_3, T)$ and $G_P^s(x_3, T)$ already introduced in previous
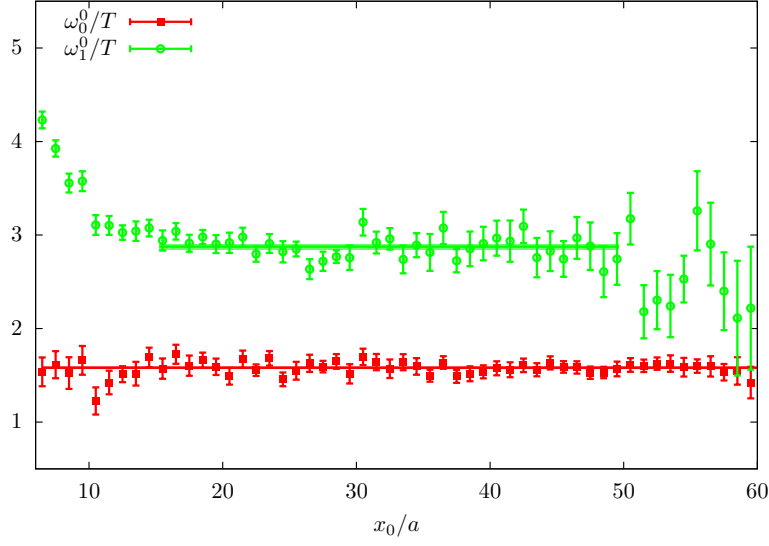
Figure 6.12: Effective 'cosh' masses for the O7 zero-temperature ensemble in the $\langle A_0 A_0 \rangle$ channel for $n = 0, 1$. The values of $\omega_n^0 \equiv \omega_{\mathbf{p}_n}^0$ are given in units of the temperature $T = 1/24a$ corresponding to our thermal ensemble.

sections with the spatial momenta given by

$$\mathbf{p} = \mathbf{p}_n \equiv (0, 0, 2\pi n/L). \tag{6.5.1}$$

Note that since all two-point functions belong to the adjoint (or *isovector*) representation of $\mathrm{SU}(N_f)$ ($N_f = 2$), the contributions of quark disconnected diagrams cancel out. The renormalization program is carried out such that

$$G_A(x_0, T, \mathbf{p}) = (Z_A(g_0^2))^2 G_A(x_0, g_0^2, T, \mathbf{p}) \tag{6.5.2}$$

$$G_P(x_0, T, \mathbf{p}) = (Z_P(g_0^2))^2 G_P(x_0, g_0^2, T, \mathbf{p}) \tag{6.5.3}$$

and similarly for the screening correlators; the value of the coefficients Z_A and Z_P can be found in Table 6.7.

6.5.2   The $T \simeq 0$ ensemble O7

As a benchmark we analyze zero-temperature data on the O7 ensemble. Here we are able to obtain the pion energy $\omega_{\mathbf{p}}^0$ by fitting a constant to the effective mass. The pion energy corresponding to $\mathbf{p} = 0$ and $\mathbf{p} = (0, 0, 2\pi/L)$ can be read off from

the plot in Fig. 6.12. The dominance of the pion contribution, particularly in the zero-momentum case, is clearly very strong. Performing a linear fit to $(\omega_{\mathbf{p}}^0)^2$ as a function of $\mathbf{p}^2$, we obtain for the slope $u^2(T \simeq 0) = 1.01(6)$, consistently with Lorentz invariance. The decay constant f_π^0, defined by Eq. (6.4.9), indeed turns out to be independent of the momentum.

Once the ground state dominates the correlator $G_A(x_0, T \simeq 0, \mathbf{p})$, one-state cosh fits of the form $A_1 \cosh(\omega_{\mathbf{p}}^0(T/2 - x_0))$ with $T = 128a$ are applied and the results are summarized in Table 6.9. The values for $\omega_{\mathbf{0}}^0$ and f_π^0 are in very good agreement with the ones quoted in [116].
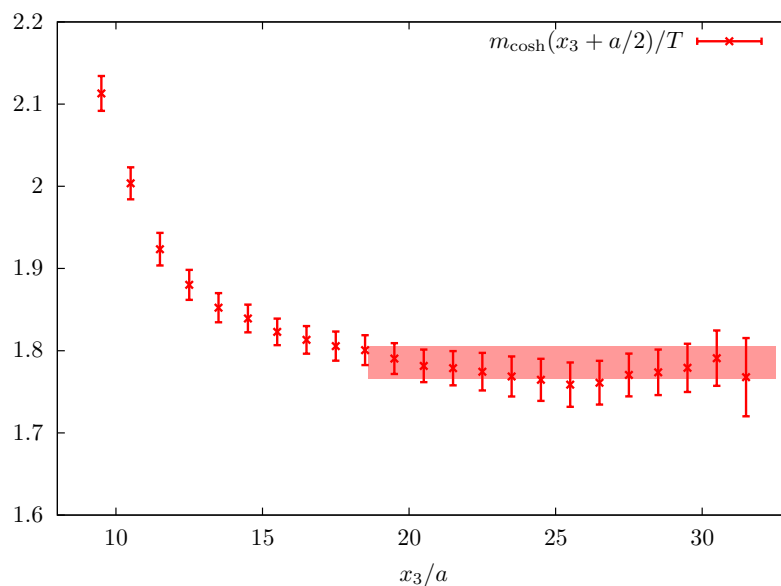
Figure 6.13: Effective 'cosh' mass plot for the screening mass m_π for the 24×64^3 thermal ensemble. The plateau has been chosen to begin at $x_3/a = 19$.

6.5.3   The estimators u_f and u_m at 170 MeV

The chiral expansion around $(T, m = 0)$ proposed in [98] assumes that one is sufficiently close to the chiral limit. In this limit, the screening pion mass m_π vanishes and the coefficient $u(T)$ is indeed the velocity of a massless pion quasiparticle in the presence of a thermal bath. A deviation from unity corresponds to a violation of boost invariance. At finite but small quark mass, we showed that the consistency of u_f and u_m serves as an indicator for the applicability of the chiral expansion. Based on the results of Table 6.8, we conclude that they are indeed consistent.
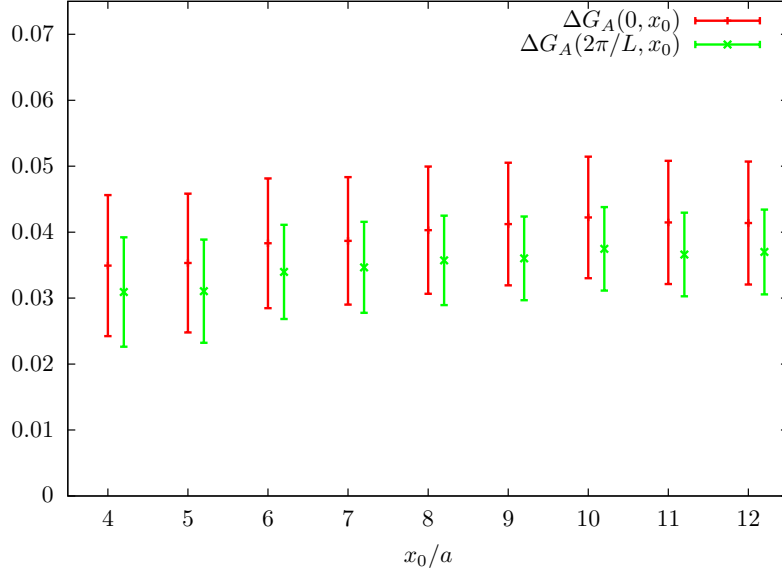
Figure 6.14: The difference $\Delta G_A(|\mathbf{p}|, x_0) \equiv [G_A(x_0, T, \mathbf{p}) - G_A^{\text{rec}}(x_0, T, \mathbf{p})]/T^3$ of the thermal correlator and the reconstructed correlator for $|\mathbf{p}| = 0$ and $2\pi/L$.

The results, in particular for u_f, are in good agreement with the results obtained in the scan C1 in view of Fig. 6.15 (ensembles with a coarser lattice spacing and a slightly heavier quark mass.) Note that to leading order, u is expected to be independent of the quark mass.

6.5.4   The reconstructed correlator $G_A^{\text{rec}}(x_0, T, \mathbf{p})$

The 'reconstructed' correlator G_A^{rec} is defined as the thermal Euclidean correlator that would be realized if the spectral function remained the zero-temperature one. We compute it following the method first proposed in [117]

$$G_A^{\text{rec}}(x_0, T, \mathbf{p}) = \sum_{m \in \mathbb{Z}} G_A(|x_0 + m\beta|, 0, \mathbf{p}). \qquad (6.5.4)$$

The previous equation is based on the identity of the kernel function

$$\frac{\cosh(\omega(\beta/2 - x_0))}{\sinh(\omega\beta/2)} = \sum_{m \in \mathbb{Z}} e^{-\omega|x_0 + m\beta|}. \qquad (6.5.5)$$

Figure 6.14 shows the difference between the thermal correlator and the reconstructed correlator. There is a statistically significant difference between the two
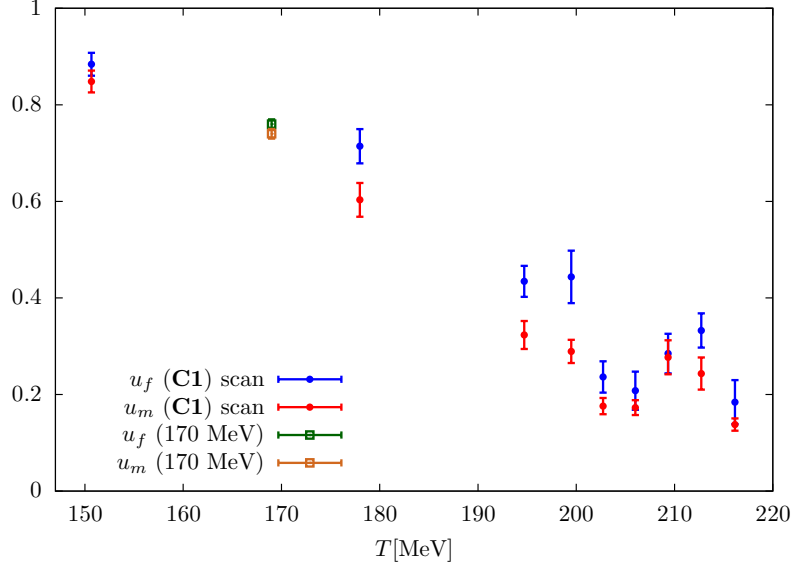
Figure 6.15: Comparison of the estimators u_f and u_m calculated in the thermal ensemble of size 24×64^3 with the ones from the C1 scan.

correlators, which shows that a change must take place in the spectral function. Because the difference is very weakly dependent on time, the change must take place in the low-frequency part of the spectral function. We expect from the thermal chiral effective theory that the change is due to a modification of the mass and/or the residue of the pion quasiparticle. Using the numbers of Table 6.8, the changes amount respectively to

$$\frac{\omega_{\mathbf{0}}}{\omega_{\mathbf{0}}^0} = 0.836(14), \qquad \frac{f_\pi^t}{f_\pi^0} = 1.03(2). \qquad (6.5.6)$$

We thus observe that while the pion decay constant remains unchanged at the precision level of a few percent, the pion mass decreases by 16%. Qualitatively, these results are consistent with the two-loop results in zero-temperature chiral perturbation theory given in [94, 95]. Future lattice calculations approaching the chiral limit would allow for a quantitative comparison.

6.5.5 The spectral function $\rho_{\mathrm{A}}(\omega, T, \mathbf{p})$ at non-zero momentum

As the next step, we test the functional form of Eq. (6.1.2) at non-zero momentum. The relevant real-time pion states with energy $\omega_{\mathbf{p}}$ have a non-zero overlap with the operator $\int d^3x \, e^{i\mathbf{p}\mathbf{x}} A_0(x)$; furthermore, the spectral function ρ_{A} becomes independent of ω in the ultraviolet, rather than growing like ω^2. We therefore expect to have the best sensitivity to the pion contribution in the correlator $G_A(x_0, T, \mathbf{p})$.

At finite temperature, the analysis of the correlator $G_A(x_0, T, \mathbf{p})$ is more involved than at zero temperature: only at sufficiently small quark masses and momenta, and not too small x_0 is the correlator parametrically dominated by the pion pole. Therefore we proceed by formulating a fit ansatz to take into account the non-pion contributions. The combination of Eqs. (6.4.10) and (6.4.11) motivates an ansatz for the spectral function reading

$$\rho_{\mathrm{A}}(\omega, \mathbf{p}) = A_1(\mathbf{p}) \sinh(\omega\beta/2)\delta(\omega - \omega_{\mathbf{p}}) + A_2(\mathbf{p})\frac{N_c}{24\pi^2}\left(1 - e^{-\omega\beta}\right)\theta(\omega - c). \quad (6.5.7)$$

The corresponding form of the correlation function then reads

$$G^A(x_0, T, \mathbf{p}) = A_1(\mathbf{p})\cosh(\omega_{\mathbf{p}}(\beta/2 - x_0)) + A_2(\mathbf{p})\frac{N_c}{24\pi^2}\left(\frac{e^{-cx_0}}{x_0} + \frac{e^{-c(\beta-x_0)}}{\beta - x_0}\right).$$
$$(6.5.8)$$

We fit $G_A(x_0, T, \mathbf{p})$ with the ansatz given in Eq. (6.5.8) for the momenta $\mathbf{p}_n = (0, 0, 2\pi n/L)$ with $n = 1, 2, 3, 4, 5$. The fit interval is chosen to be $x_0/a \in [5, 12]$ in order to avoid cutoff effects. There are four parameters involved, $A_1(\mathbf{p})$, $\omega_{\mathbf{p}}$, $A_2(\mathbf{p})$ and c. Leaving $\omega_{\mathbf{p}}$ as a fit parameter led to poorly constrained fits. Therefore we set the value of $\omega_{\mathbf{p}}$ to the prediction of Eq. (6.1.2) in order to test whether the data can be described in this way. Motivated by the expected large-ω behavior of the spectral function, we quote the rescaled parameter $\tilde{A}_2 = A_2/\mathbf{p}^2$. Note that the quark mass is negligible compared to all the non-vanishing $|\mathbf{p}|$ values considered here. The expected value of $\tilde{A}_2$ is of order unity, in view of Eq. (6.4.11). Eq. (6.4.15) allows us to establish the relation between the fit parameter $A_1(\mathbf{p})$ and the residue itself,

$$\mathrm{Res}(\omega_{\mathbf{p}}) \quad = \quad 2A_1(\mathbf{p})\omega_{\mathbf{p}}\sinh(\omega_{\mathbf{p}}\beta/2). \quad (6.5.9)$$

One may further convert the result for the residue into a parameter $b(\mathbf{p})$, defined by

$$\text{Res}(\omega_{\mathbf{p}}) = f_\pi^2(m_\pi^2 + \mathbf{p}^2)(1 + b(\mathbf{p})). \tag{6.5.10}$$

From the chiral prediction Eq. (6.4.13), we thus expect $b(\mathbf{p})$ to be small compared to unity if the effective description is working. The results are summarized in Table 6.10.

The fits provide a good description of the data; see the $\chi^2/\text{d.o.f}$ values and Fig. 6.16. We observe that at the smallest momentum, $|\mathbf{p}| \simeq 400\,\text{MeV}$, $b(\mathbf{p})$ really is small, pointing to a successful check of the chiral prediction. At higher momenta, the negative, order unity value of $b(\mathbf{p})$ indicates that the residue of the pion pole is reduced. It should also be remembered that at higher momenta, neglecting the width of the quasiparticle is bound to be an increasingly poor approximation. The coefficient $\tilde{A}_2$ is expected to be of order unity from the treelevel prediction Eq. (6.4.11). Indeed the numbers in Table 6.10 are of order unity. One reason for the relatively large value of the coefficient at the smallest momentum could be that axial-vector excitations are contributing around the threshold c, thus adding spectral weight. The value of the threshold at $|\mathbf{p}| \simeq 400\,\text{MeV}$, is about 1.1GeV, a value we consider to be reasonable given that the mass of the lightest axial-vector meson in nature is $m_{a_1} \approx 1.2\text{GeV}$.

In order to gauge the discriminative power of the test, it is interesting to ask whether a rather different model is consistent with the lattice data on $G_A(x_0, \mathbf{p}, T)$. We assume for this purpose that the dispersion relation and the residue have the same $\mathbf{p}$-dependence as at zero temperature. We therefore set $\omega_{\mathbf{p}} = \sqrt{\omega_0^2 + \mathbf{p}^2}$, and obtain for $n = 1$ an equally good description of the data, with a value of the residue $\text{Res}(\omega_{\mathbf{p}}) = 3.01(4)$ not too different from $(f_\pi^t)^2(\omega_0^2 + \mathbf{p}^2) = 2.84(7)$. The other fit parameters take the values $\tilde{A}_2 = 2.42(17)$ and $c/T = 10.2(4)$. While the perturbative coefficient and the threshold values seem less plausible to us, we cannot completely exclude this model on the basis of the lattice data.

To summarize, we have found that the dispersion relation of the pion quasiparticle is consistent with Eq. (6.1.2), the parameter u being determined at vanishing spatial momentum. In order to test the dependence of our results on the fit ansatz made, in the next section we apply the Backus-Gilbert method.
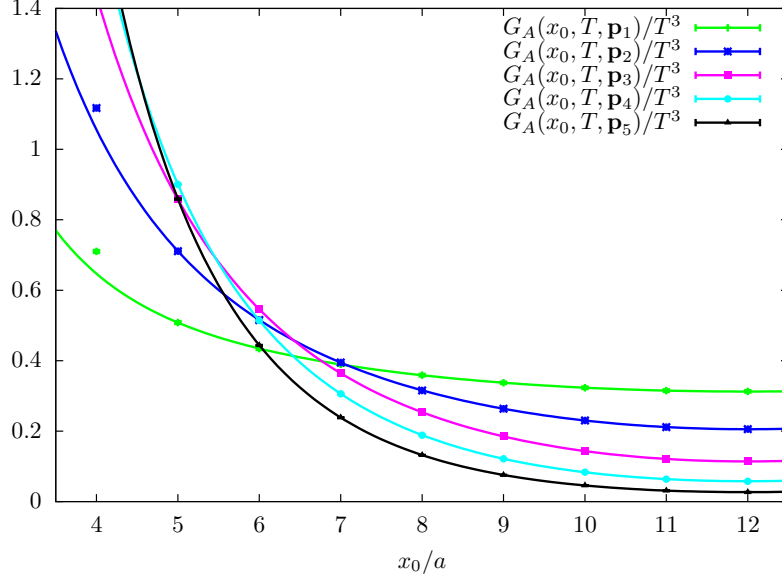
Figure 6.16: Correlation functions $G_A(x_0, T, \mathbf{p}_n)/T^3$ with $\mathbf{p}_n = (0, 0, 2\pi n/L)$, together with the fits resulting from the four-parameter Ansatz of Eq. (6.5.8). The corresponding parameter values are given in Table 6.10. All renormalization constants are included.

6.5.6　The Backus-Gilbert method for $\rho_{\mathrm{A}}(\omega, \mathbf{p})$

The Backus-Gilbert method is a method suitable for inverting integral equations like Eq. (6.4.7). It has been studied in many contexts (see e.g. [19–21,56,118,119]). While it has not been applied in lattice QCD, to our knowledge, the central notion of resolution function was used in [120]. We first describe the method in some generality. It is a completely model-independent approach since no ansatz needs to be made for the spectral function.

The goal is to solve the integral equation

$$G(x_i) = \int_0^\infty d\omega f(\omega) K(x_i, \omega) \qquad x_i \neq 0 \qquad \forall i \qquad (6.5.11)$$

for the unknown function $f(\omega)$, given the kernel $K(x_i, \omega)$ and given data on $G(x_i)$. The idea is to define an estimator $\hat{f}(\bar{\omega})$

$$\hat{f}(\bar{\omega}) = \int_0^\infty \hat{\delta}(\bar{\omega}, \omega) f(\omega) d\omega \qquad (6.5.12)$$

where $\hat{\delta}(\bar{\omega}, \omega)$ is called the resolution function or averaging kernel. It is a smooth function concentrated around some reference value $\bar{\omega}$, normalized according to $\int_0^\infty d\omega \hat{\delta}(\bar{\omega}, \omega) = 1$, and parametrized at fixed $\bar{\omega}$ by coefficients $q_i(\bar{\omega})$,

$$\hat{\delta}(\bar{\omega}, \omega) = \sum_i q_i(\bar{\omega}) K(x_i, \omega), \tag{6.5.13}$$

so that $\hat{f}$ is obtained according to

$$\hat{f}(\bar{\omega}) = \sum_{i=1}^n G(x_i) q_i(\bar{\omega}). \tag{6.5.14}$$

The goal is then to minimize the width of the resolution function. Minimizing the second moment of $\hat{\delta}(\bar{\omega}, \omega)^2$ in its second argument around its first argument yields

$$q_i(\bar{\omega}) = \frac{\sum_j W_{ij}^{-1}(\bar{\omega}) R(x_j)}{\sum_{k,l} R(t_k) W_{kl}^{-1}(\bar{\omega}) R(x_l)}, \tag{6.5.15}$$

where

$$W_{ij}(\bar{\omega}) = \int_0^\infty d\omega K(x_i, \omega)(\omega - \bar{\omega})^2 K(x_j, \omega), \tag{6.5.16}$$

$$R(x_i) = \int_0^\infty K(x_i, \omega) d\omega. \tag{6.5.17}$$

We remark that $\hat{f}(\omega)$ equals $f(\omega)$ if the latter is constant.

The matrix $W_{ij}(\bar{\omega})$ is very close to being singular. This is the reason why, when trying to use a data set with error bars, one needs to regulate the inverse problem, replacing the matrix W by

$$W_{ij} \rightarrow \lambda W_{ij} + (1 - \lambda) S_{ij}, \qquad 0 < \lambda < 1, \tag{6.5.18}$$

where S_{ij} is the covariance matrix of the data. The value of λ controls the trade-off between resolution and stability. For values of λ close to 1, we obtain the best possible resolution. However the results tend to be unstable since the matrix is poorly conditioned and large cancellations take place among the terms in Eq. (6.5.14). Reducing λ improves the stability of the result at the cost of deteriorating the frequency resolution. One may start from a value for λ near unity and decrease

it until the statistical error on $\hat{\rho}(\omega)$ drops to say 5%. Of all linear methods, the result $\hat{\rho}(\omega)$ then has the best possible frequency resolution (as measured by the second moment of $\delta(\bar{\omega}, \omega)^2$ in its second argument) for the given statistical uncertainty of 5%. It should be emphasized that, as a matter of principle, any choice of λ yields a correct result, in the sense that the relation between $\hat{\rho}(\omega)$ and $\rho(\omega)$ is given model-independently by the resolution function. However, in order to be useful, the result must have both a reasonable statistical uncertainty and a decent frequency-resolution. It is worth noting that if the statistics is increased so that S_{ij} is overall reduced by a factor $1/\xi$, then keeping λ constant will result in a better frequency resolution; instead, choosing a new value for λ so as to keep $(1-\lambda)S_{ij}$ constant will maintain the same resolution function and $\hat{\rho}(\omega)$ will have a reduced statistical uncertainty by $1/\sqrt{\xi}$. In particular, it is predictable by how much the statistics needs to be increased in order to achieve a certain frequency resolution at fixed statistical uncertainty.
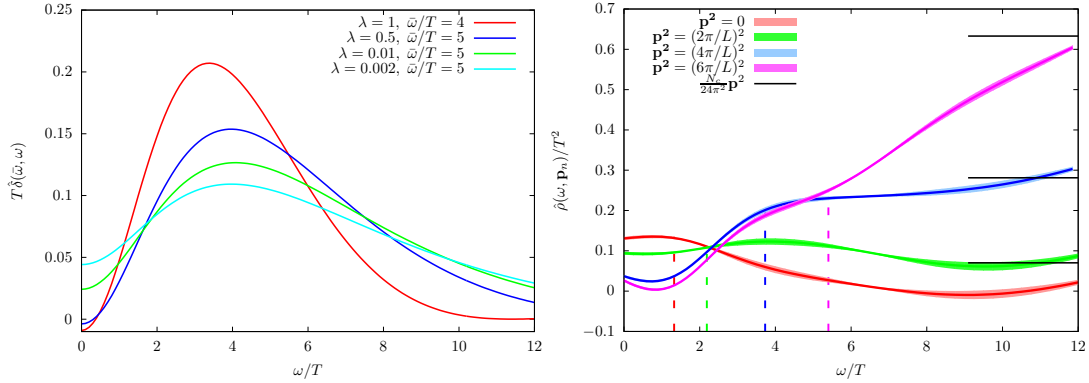
Figure 6.17: Left: Some examples of resolution functions for different values of λ centered at $\bar{\omega}/T$. Right: Estimators $\hat{\rho}(\omega, \mathbf{p}_n)/T^2$ for $n = 0, 1, 2, 3$ together with its error shown as a band. The vertical colored dashed lines correspond to the locations of the expected positions of the poles $\omega_{\mathbf{p}_n}$ according to Eq. (6.1.2) with $u(T) = u_m$. The black horizontal lines correspond to the treelevel asymptotic values of $\rho_A(\omega, \mathbf{p})$. All renormalization constants have been taken into account as well as the improvement program on the axial correlators. Dimensionful quantities have been made dimensionless by the appropriate power of $T = 1/24a$.

We apply this method to Eq. (6.4.7). In order to regularize the finite-temperature

kernel at $\omega = 0$ we rewrite the equation as

$$G_A(x_0, T, \mathbf{p}) = \int_0^\infty d\omega \left(\frac{\rho_A(\omega, \mathbf{p})}{\tanh(\omega/2)} \right) \underbrace{\left(\frac{\cosh(\omega(\beta/2 - x_0))}{\cosh(\omega\beta/2)} \right)}_{\doteq K(x_0, \omega)}. \qquad (6.5.19)$$

This defines our estimator $\hat{\rho}$ at $\omega = \bar{\omega}$,

$$\hat{\rho}(\bar{\omega}, \mathbf{p}) = \int_0^\infty d\omega \, \hat{\delta}(\bar{\omega}, \omega) \left(\frac{\rho_A(\omega, \mathbf{p})}{\tanh(\omega\beta/2)} \right). \qquad (6.5.20)$$

After regulating the problem via the covariance matrix S_{ij} as in Eq. (6.5.18), the inversion is carried out via Singular Value Decomposition. This offers the opportunity to diagnose how badly conditioned the matrix is. With all quantities made dimensionless by applying appropriate powers of the temperature, we choose $\lambda = 2 \cdot 10^{-3}$ in the following, so as to yield an error $\lesssim 5\%$ on $\hat{\rho}$. Typical condition numbers of the regularized matrix in Eq. (6.5.18) are $\sim 10^8$. The situation gets worse when λ approaches unity, as explained above. The results for zero momentum and the first three units of momentum are shown in the right panel of Fig. 6.17. As in the case of the fit, we included the points of the correlation in the interval $x_0/a = [5, 12]$ so $W_{ij}(\bar{\omega})$ is a $n \times n$ symmetric matrix with $n = 8$. With our chosen value of λ, we obtain a relative error on $\hat{\rho}$ of $\sim 3 - 5\%$, while the resolution function is displayed in the left panel of Fig. 6.17. One direct observation is the fact that the expected asymptotic behavior for large values of ω is reproduced very well.

The right panel of Fig. 6.17 also shows the expected positions of the poles that follow from Eq. (6.1.2) as vertical colored dashed lines. We now want to test the $\mathbf{p}$ dependence of the residue $\text{Res}(\omega_{\mathbf{p}})$ via the following argument. If we assume that, for a given value of ω, $\hat{\rho}(\omega, \mathbf{p})$ is dominated by the pion pole, we obtain the following estimator for the residue,

$$\text{Res}(\omega_{\mathbf{p}}, \omega)_{\text{BG}} = \frac{2\omega_{\mathbf{p}} \tanh(\omega_{\mathbf{p}}\beta/2)\hat{\rho}(\omega, \mathbf{p})}{\hat{\delta}(\omega, \omega_{\mathbf{p}})}. \qquad (6.5.21)$$

Here we treat $\omega_{\mathbf{p}}$ as input and calculate it using Eq. (6.1.2) with the value of $u = u_m = 0.74(1)$ determined at zero momentum. The result as a function of ω is shown in Fig. 6.18 for zero and one unit of momentum. The natural choice where
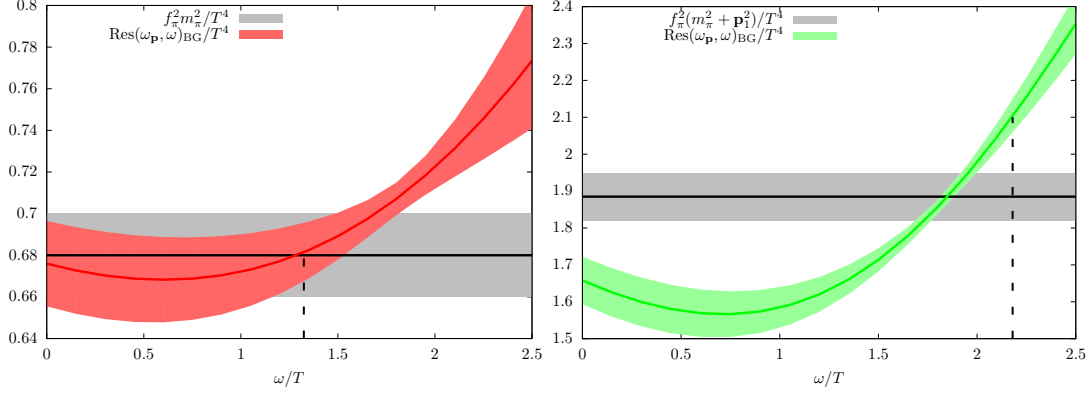
Figure 6.18: The effective residue $\mathrm{Res}(\omega_{\mathbf{p}}, \omega)_{\mathrm{BG}}$ as defined in Eq. (6.5.21). Left: No momentum induced, $\mathbf{p} = 0$. Right: One unit of momentum induced, $\mathbf{p}_1 = (0, 0, 2\pi/L)$. The grey band is the expectation in terms of screening quantities, Eq. (6.4.13). All renormalization factors are included. The errors arise from the statistical uncertainty. The values of $\omega_{\mathbf{p}}$ are indicated by dashed vertical lines.

$\mathrm{Res}(\omega_{\mathbf{p}}, \omega)_{\mathrm{BG}}$ is expected to be the best estimator of the residue is at $\omega \approx \omega_{\mathbf{p}}$. Looking at Fig. 6.18, one sees that approximately around this value the curve intercepts the grey band, which represents the prediction Eq. (6.4.13). The latter is particularly well verified at zero momentum, while the agreement at $|\mathbf{p}| = |\mathbf{p}_1| \approx 400\mathrm{MeV}$ is at the ten percent level. These observations provide a further test that the pion dispersion relation Eq. (6.1.2) predicted by the thermal chiral effective theory is consistent with the lattice two-point function of the axial charge density.

Comparing the method followed in this subsection with the previous method based on a global fit to the spectral function, the former has the advantage of not requiring an explicit parametrization of the non-pion contributions to the spectral function. This observation may be useful in other lattice studies of spectral functions.

6.6   Lattice calculation (III): finite volume effects at $T = 150\mathrm{MeV}$

Since in principle we are studying a relatively low-energy effect compared to the typical available probing scales on a common lattice calculation $1/L \ll \mu \ll 1/a$, finite volume effects may appear as the most dangerous source of systematic errors

(see Sec. 4.4). Therefore it is worth investing in the generation of additional ensembles to rule out any possible finite volume dependency. In this section we discuss the generation of a new ensemble and the measurements of some of the previously considered quantities. We focus on the lowest temperature in the C1 scan. It corresponds to $T = 150$MeV and is part of a fixed quark mass scan at $\overline{m}^{\overline{\mathrm{MS}}} \approx 15$MeV. It lies well below the transition region and our chiral effective theory appears to work best since e.g $u_f/u_m \simeq 1$. Although in Sec. 6.5 we already presented an ensemble with a larger three-dimensional volume than those of the C1 scan where no obvious evidence was found that finite-volume effects could affect our interpretation of the pion velocity estimators, it is always important to perform a systematic analysis of finite volume effects by comparing two ensembles with the same bare parameters and different volumes. Therefore, we generate an ensemble 16×48^3 at $T = 150$MeV with the same quark mass of 15MeV following the same recipe explained in Sec. 6.3 and Sec. 6.5 concerning the tuning of c_{sw}, κ and scale setting procedure.

A slight change in the value of κ may lead to huge modifications in the quark mass. Therefore, it is always a good practice to compute the PCAC mass in order to check that indeed the right quark mass was selected. Fig. 6.19 shows that $\overline{m}^{\overline{\mathrm{MS}}}(\mu = 2\mathrm{GeV}) = 14.8(3)$ MeV is in agreement with the value quoted in Table 6.2.

6.6.1   The correlator $G_A(x_0)$

In Sec. 6.3.3 we argued that the dominance of the pion in G_A is a crucial assumption for the applicability of the chiral effective theory. One crosscheck is given by the ratio of estimators u_f/u_m. Therefore we are particularly concerned about G_A. Nevertheless, in view of Fig. 6.20 one sees that finite volume effects are almost absent and both data sets agree within errors even at $x_0 = \beta/2$.

6.6.2   Finite volume dependency of f_π and m_π and the pion velocity

In view of Fig. 6.21, Table 6.12, and by comparing with the first row of Table 6.5 one can safely say that we are free of finite volume effects since all results agree within one standard sigma deviation. This adds confidence to the interpretation
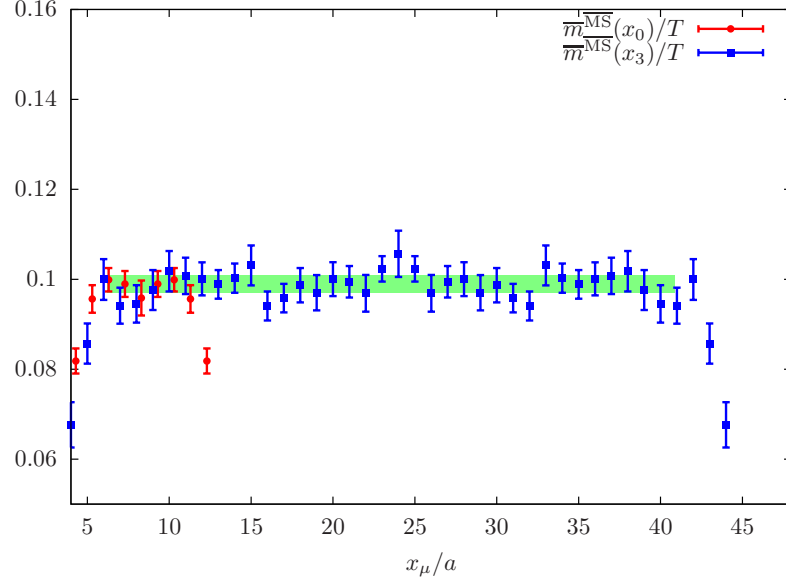
Figure 6.19: The PCAC mass for the 16×48^3 thermal ensemble. The renormalization factors Z_A and Z_P are included, as well as the conversion factor from the SF to $\overline{\text{MS}}$ at a scale of $\mu = 2\text{GeV}$, which amounts to 0.968(20) [50]. We also plot the result along the x_0-direction to show that indeed both are compatible.
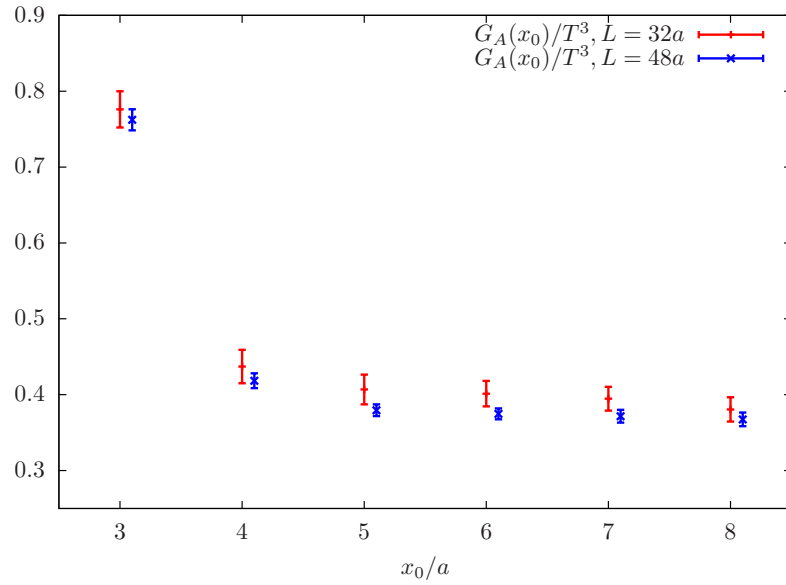
Figure 6.20: Axial charge euclidean correlator $G_A(x_0)$ at $T = 150\text{MeV}$ for two different volumina. All renormalization factors are included and $T = 1/16a$.
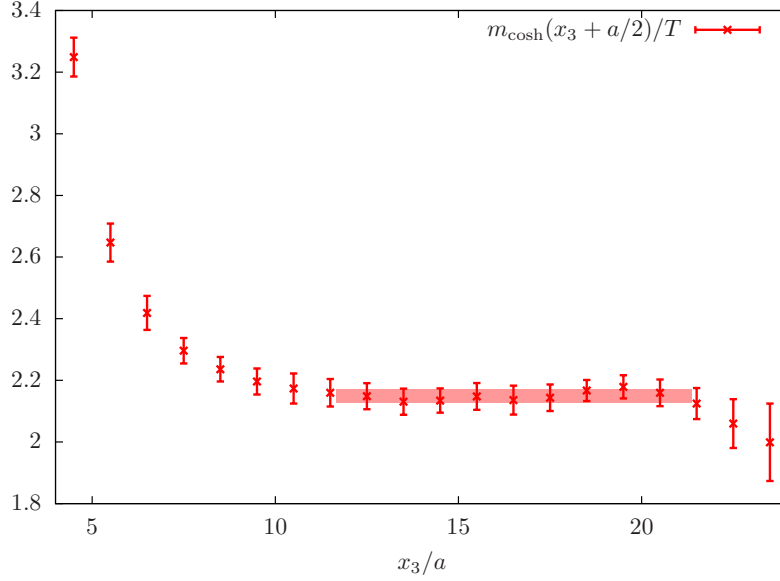
Figure 6.21: Effective 'cosh' mass plot for the screening mass m_π for the 16×48^3 thermal ensemble. The plateau has been chosen to begin at $x_3/a = 11$.

that our estimators would correspond to the pion velocity of a massless excitation in a thermal bath.

6.7 Conclusions

The results for two estimators of the pion velocity is displayed in Fig. 6.15 for the C1 scan and the fine thermal ensemble at $T = 170\text{MeV}$. The reasonable agreement of the two estimators observed up to $T \simeq 190\,\text{MeV}$ is a successful test of the validity of the chiral expansion. It therefore appears likely that the estimator $u_f(T \simeq 150\text{MeV}) = 0.88(2)$ for $\overline{m}^{\overline{\text{MS}}} = 15\,\text{MeV}$ and $u_f(T \simeq 170\text{MeV}) \sim 0.76(1)$ for $\overline{m}^{\overline{\text{MS}}} = 12.8\,\text{MeV}$ do indeed provide a valid estimate of the pion quasiparticle velocity. The finite volume analysis performed on the 16×48^3 ensemble consolidate our statements and guarantees that most of the systematics are under control. The fine lattice at $T = 170\text{MeV}$ indicates that also cut-off effects do not spoil the property of $u(T) < 1$ for $T > 0$. Both values for u show that there is a significant departure from unity, corresponding to a violation of boost invariance through the presence of the thermal medium. It shows that, although the hadron resonance gas model prediction for the thermodynamic potential $(e - 3p)/T^4$ [87] and the charge

fluctuations agree well with lattice results [86,88], the properties of the in-medium excitations can be shifted appreciably from their $T = 0$ counterparts.

The ability to extract the dispersion relation from Euclidean quantities rests on the dominance of the pion quasiparticle contribution in the axial charge correlator and in the pseudoscalar density correlator. We find that at $T \simeq 150\,\mathrm{MeV}$, the static screening pion mass and the associated decay constant f_π have changed only by about 5% from their $T = 0$ values. Also the mass of the pion quasiparticle turns out to be very close to the $T = 0$ pion mass. These observations are in agreement with the predictions of the chiral expansion around the point $(m = 0, T = 0)$ [113]. By contrast, at $T = 170\mathrm{MeV}$, we found that the pion quasiparticle mass is reduced significantly by thermal effects compared to its vacuum value – unlike the pion screening mass, which increases. At even higher temperatures, the decay constant f_π and the correlation length m_π^{-1} fall off rapidly, a behavior no longer described by the chiral expansion.

Fig. 6.7 shows the behavior of the effective condensate defined via the GOR relation. This quantity, in spite of being a chiral order parameter, varies remarkably slowly throughout the crossover region. Fig. 6.9 displays our results for m_π/T and f_π/T as a function of temperature for two different quark masses; the temperature has been rescaled in units of the quark-mass dependent crossover temperature. Within the accuracy of the data, hardly any quark mass dependence is observed. These observations indicate that we are still deep in the crossover region and far from the chiral regime, where one expects a rapid fall-off of the condensate when $T \stackrel{<}{\longrightarrow} T_c$ and an abrupt rise of m_π just above T_c.

Assuming the results hold to further scrutiny, one may wonder how much a modified mass and dispersion relation of the pion affects the predictions of the hadron resonance gas model for equilibrium properties. In answering the question, one must take into account that the modification of the pion dispersion relation is due to the presence of hadrons in the medium, and issues of double counting arise. However, the following estimates may provide a useful first idea of the size of the effect. At the temperature of 170MeV in the two-flavor theory with a zero-temperature pion mass of 270MeV, we estimate, using the hadron resonance gas model, an isovector quark number susceptibility[8] amounting to $\chi_s/T^2 = 0.42$. In

---

[8]The current is here normalized as $\sqrt{2}V_\mu^a(x)$.

the HRG model, the pion contributes[9] $\chi_s/T^2|_{\text{pions}} = 4\beta^3 \int \frac{d^3p}{(2\pi)^3} f_B(p)(1 + f_B(p)) = 0.28$. If the spatial-momentum integral in the pion contribution is cut off at $p_{\text{max}} = 400\,\text{MeV}$ (roughly the range of validity of the chiral effective theory that we found), the contribution is reduced to 0.11. If we instead use the modified dispersion relation with the lower quasiparticle mass $\omega_0 = 223\text{MeV}$ and $u = 0.74$, the contribution for $p < p_{\text{max}}$ amounts again to 0.28. It is unclear whether one should include a contribution from higher momenta, given that the thermal width of the pion may then not be negligible. The numbers above illustrate that the contribution of the pion to the quark number susceptibility might not be as strongly affected as one may at first think. However, the contribution comes from softer pions, which implies a reduced amplitude of the transport peak in the two-point function of the vector current $V_i^a(x)$, an effect that can be tested in lattice simulations.

---

[9]Here $f_B(p) = (e^{\beta\omega_p} - 1)^{-1}$ is the Bose distribution.

6.8   Tables

$6/g_0^2$	κ	c_{sw}	a [fm]	T [MeV]	$Z_A(g_0^2)$	$\overline{m}^{\overline{\mathrm{MS}}}$ [MeV]
5.20	0.13594	2.017147	0.0818(8)	150(1)	0.7703(57)	15.4(4)
5.30	0.13636	1.909519	0.0693(6)	177(2)	0.7784(52)	14.6(6)
5.355	0.13650	1.859618	0.0633(7)	194(2)	0.7826(49)	14.7(6)
5.37	0.13652	1.846965	0.0618(7)	199(2)	0.7838(48)	15.8(7)
5.38	0.13654	1.838739	0.0608(7)	203(2)	0.7845(48)	15.5(9)
5.39	0.13656	1.830676	0.0599(6)	206(2)	0.7853(48)	14.8(6)
5.40	0.13658	1.822771	0.0589(6)	209(2)	0.7860(47)	16.8(7)
5.41	0.13660	1.815019	0.0580(6)	213(2)	0.7868(47)	15.2(7)
5.42	0.13662	1.807416	0.0571(6)	216(2)	0.7875(46)	14.0(7)
5.43	0.13664	1.799958	0.0562(6)	219(2)	0.7882(46)	12.2(8)
5.44	0.13665	1.792642	0.0553(5)	223(2)	0.7889(45)	14.2(10)
5.45	0.13666	1.785462	0.0544(5)	226(2)	0.7896(45)	10.3(8)
5.47	0.13667	1.771499	0.0527(5)	234(2)	0.7910(44)	15.4(9)

Table 6.2: Lattice parameters for the scan C1. All our finite-temperature lattices are 16×32^3. The error on the lattice spacings and on the temperatures comes from interpolating a second order polynomial with the three known input values for r_0/a evaluated at $6/g_0^2 = 5.20, 5.30, 5.50$ [50]. The error shown on $\overline{m}^{\overline{\mathrm{MS}}}$ includes neither the uncertainty of the renormalization constants nor the error due to the scale setting. The latter two sources of error combine to be about 0.4-0.5 MeV in the whole range of $6/g_0^2$.

$6/g_0^2$	κ	c_{sw}	a [fm]	T [MeV]	$Z_A(g_0^2)$	$\overline{m}^{\overline{\text{MS}}}$ [MeV]
5.30	0.13640	1.909519	0.0693(6)	177(2)	0.7784(52)	8.2(8)
5.32	0.13646	1.890703	0.0671(7)	183(2)	0.7800(51)	7.7(5)
5.33	0.13649	1.881590	0.0660(7)	186(2)	0.7808(50)	5.2(10)
5.34	0.13651	1.872665	0.0649(7)	189(2)	0.7815(50)	7.4(6)
5.35	0.13653	1.863922	0.0639(7)	192(2)	0.7823(49)	7.9(6)
5.36	0.13655	1.855357	0.0628(7)	195(2)	0.7830(49)	9.3(4)
5.37	0.13657	1.846965	0.0618(6)	199(2)	0.7838(48)	9.7(9)
5.38	0.13659	1.838739	0.0608(7)	203(2)	0.7845(48)	9.0(7)

Table 6.3: Lattice parameters with lower quark mass (scan D1; the lattice size is 16×32^3 for each ensemble). The displayed errors have the same meaning as in Table 6.2.

$6/g_0^2$	5.20
κ	0.13594
c_{sw}	2.017147
T [MeV]	37.7(4)
a [fm]	0.0818(8)
Z_A	0.7703(57)
$\overline{m}^{\overline{\text{MS}}}(\mu = 2\text{GeV})$ [MeV]	14.7(3)
m_π [MeV]	305(5)
f_π [MeV]	93(2)
$\left| \langle \bar{\psi}\psi \rangle_{\text{GOR}}^{\overline{\text{MS}}} \right|^{1/3} (\mu = 2\text{GeV})$ [MeV]	364(7)
$\omega_{\mathbf{0}}$ [MeV]	294(4)
$f_{\pi,\mathbf{0}}$ [MeV]	97(3)
$\left| \langle \bar{\psi}\psi \rangle_{\text{GOR},\mathbf{0}}^{\overline{\text{MS}}} \right|^{1/3} (\mu = 2\text{GeV})$ [MeV]	368(9)
u_f	0.96(2)
u_m	0.92(6)
u_f/u_m	1.04(4)
$\omega_{\mathbf{0}}/m_\pi$	0.96(2)

Table 6.4: Summary of results for the 64×32^3 ensemble 'A5'.

$T[\mathrm{MeV}]$	$G_P^{\overline{\mathrm{MS}}}(\beta/2)/T^3$	$G_A(\beta/2)/T^3$	$m_\pi(T)/T$	$f_\pi(T)/T$	$\left|\langle\bar{\psi}\psi\rangle_{\mathrm{GOR}}^{\overline{\mathrm{MS}}}\right|^{1/3}/T$	u_f	u_m	u_f/u_m
150(1)	26.5(7)	0.38(2)	2.15(4)	0.59(2)	2.40(5)	0.88(2)	0.84(2)	1.04(3)
177(2)	15.2(7)	0.31(1)	2.05(6)	0.41(2)	1.98(6)	0.71(4)	0.60(3)	1.18(6)
194(2)	8.1(4)	0.35(1)	2.4(1)	0.26(2)	1.67(7)	0.43(3)	0.32(3)	1.3(1)
199(2)	6.3(3)	0.34(1)	2.5(1)	0.27(3)	1.7(1)	0.44(5)	0.29(2)	1.5(2)
203(2)	4.5(2)	0.394(8)	3.13(8)	0.15(2)	1.4(1)	0.24(3)	0.18(2)	1.3(2)
206(2)	4.8(3)	0.400(9)	3.1(2)	0.13(3)	1.3(2)	0.21(4)	0.17(2)	1.2(3)
209(2)	5.8(4)	0.38(1)	2.4(3)	0.18(3)	1.3(2)	0.28(4)	0.28(4)	1.0(2)
213(2)	5.0(4)	0.372(9)	2.3(2)	0.20(2)	1.4(1)	0.33(4)	0.24(3)	1.4(2)
216(2)	4.3(3)	0.384(8)	3.4(1)	0.12(3)	1.3(2)	0.18(5)	0.14(1)	1.3(2)
219(2)	3.3(2)	0.414(8)	3.6(1)	0.12(3)	1.4(3)	0.19(5)	0.09(1)	2.0(5)
223(2)	4.0(3)	0.401(9)	2.6(2)	0.21(3)	1.6(2)	0.32(4)	0.16(3)	2.0(3)
226(2)	2.5(1)	0.419(8)	3.2(2)	0.11(3)	1.3(2)	0.17(4)	0.074(9)	2.2(6)
234(2)	2.8(2)	0.429(7)	3.1(3)	0.13(1)	1.3(1)	0.19(2)	0.11(2)	1.6(3)

Table 6.5: Summary of numerical results for the temperature scan C1. All errors given here are statistical and the uncertainty from the renormalization constants is not included.

T[MeV]	$G_P^{\overline{\mathrm{MS}}}(\beta/2)/T^3$	$G_A(\beta/2)/T^3$	$m_\pi(T)/T$	$f_\pi(T)/T$	$\left\|\langle\bar{\psi}\psi\rangle_{\mathrm{GOR}}^{\overline{\mathrm{MS}}}\right\|^{1/3}/T$	u_f	u_m	u_f/u_m
177(2)	14.9(10)	0.36(2)	2.3(1)	0.28(3)	2.0(2)	0.45(5)	0.27(4)	1.6(3)
183(2)	11.5(9)	0.35(1)	2.26(9)	0.28(4)	2.0(2)	0.46(7)	0.22(2)	2.0(3)
186(2)	8.6(9)	0.41(1)	2.1(2)	0.25(7)	2.1(4)	0.38(9)	0.13(3)	3(1)
189(2)	9.9(9)	0.37(1)	2.38(9)	0.26(2)	2.1(1)	0.42(3)	0.18(2)	2.3(3)
192(2)	7.4(5)	0.385(9)	2.5(1)	0.25(11)	2.0(6)	0.4(2)	0.15(2)	2.6(11)
195(2)	8.9(5)	0.369(8)	2.5(1)	0.20(2)	1.6(1)	0.33(4)	0.21(2)	1.6(2)
199(2)	8.2(7)	0.37(1)	2.64(9)	0.19(3)	1.7(2)	0.31(5)	0.19(2)	1.6(3)
203(2)	7.1(5)	0.39(1)	2.7(1)	0.19(3)	1.8(2)	0.30(5)	0.15(2)	2.0(4)

Table 6.6: Summary of numerical results for the D_1 temperature scan. All errors given here are statistical and the uncertainty from the renormalization constants is not included.

$6/g_0^2$	5.50
κ	0.13671
c_{sw}	1.751496
$T_{N_\tau=24}$ [MeV]	169(3)
$T_{N_\tau=128}$ [MeV]	32(1)
a [fm] [50]	0.0486(4)(5)
Z_A [50]	0.793(4)
Z_P [50]	0.5184(53)
$\overline{m}^{\text{MS}}/T(\mu = 2\text{GeV})$	0.0757(7)

Table 6.7: Summary of the main parameters for the 24×64^3 finite temperature ensemble as well as for the 128×64^3 zero temperature ensemble labelled as O7 in [50]. The quark mass is computed at and normalized with the $T = 1/24a$ temperature. The statistics collected for two-point functions is respectively 360 and 149 configurations at $N_\tau = 24$ and $N_\tau = 128$, with respectively 64 and 16 point sources per configuration, exploiting the translational invariance of the system.

m_π/T	1.79(2)
f_π/T	0.46(1)
u_f	0.76(1)
u_m	0.74(1)
u_f/u_m	1.02(1)
ω_0/T	1.32(2)
f_π^t/T	0.62(1)
$\text{Res}(\omega_0)/T^4$	0.68(2)

Table 6.8: Summary of the results for the $N_\tau = 24$ thermal ensemble. All renormalization factors are included and the errors are purely statistical. The value of ω_0 is calculated using $\omega_0 = u_m m_\pi$. In the same way $f_\pi^t = f_\pi/u_m$. The value of the residue is obtained according to Eq. (6.4.13), $\text{Res}(\omega_0) = f_\pi^2 m_\pi^2$.

n	A_1/T^3	$\omega^0_{\mathbf{p}_n}/T$	$\chi^2/d.o.f$	f^0_π/T	$\mathrm{Res}(\omega_{\mathbf{p}})$
0	$8.4(3) \times 10^{-3}$	$1.579(12)$	0.05	$0.599(8)$	$0.89(3)$
1	$5.3(4) \times 10^{-4}$	$2.88(3)$	0.4	$0.629(12)$	$3.27(15)$

Table 6.9: Properties of the pion at zero temperature. The index n denotes the momentum $\mathbf{p}_n$ induced and $\omega^0_{\mathbf{p}_n}$ corresponds to the energy of the state (in particular, $\omega^0_{\mathbf{0}}$ is the pion mass). All errors are purely statistical, and all renormalization factors are included. The fit interval begins at $x_0/a = 6$ for the zero-momentum case and at $x_0/a = 15$ for one unit of momentum in view of the effective mass plot of Fig. 6.12. Dimensionful quantities are normalized with $T = 1/24a$.

n	A_1/T^3	$\omega_{\mathbf{p}_n}/T$	$\tilde{A}_2$	c/T	$\mathrm{Res}(\omega_{\mathbf{p}_n})/T^4$	b	$\chi^2/d.o.f$
1	$2.95(4) \times 10^{-1}$	$2.19(3)$	$1.78(8)$	$6.7(3)$	$1.72(6)$	$-0.08(3)$	0.06
2	$1.40(5) \times 10^{-1}$	$3.73(6)$	$1.26(2)$	$6.1(1)$	$3.3(2)$	$-0.39(4)$	0.15
3	$4.9(3) \times 10^{-2}$	$5.40(9)$	$1.19(1)$	$7.7(1)$	$3.9(5)$	$-0.65(4)$	0.35
4	$1.7(2) \times 10^{-2}$	$7.1(1)$	$1.15(1)$	$9.67(9)$	$4.21(7)$	$-0.78(3)$	0.49
5	$4(1) \times 10^{-3}$	$8.8(1)$	$1.12(1)$	$11.7(1)$	$3(1)$	$-0.89(3)$	1.04

Table 6.10: Results of fits to the axial-charge density correlator at non-vanishing momentum $\mathbf{p}_n$. All errors quoted are statistical, and all renormalization factors are included. The quantity $\omega_{\mathbf{p}}/T$ is not a fit parameter; rather it is set to the value predicted by Eq. (6.1.2) with $u(T) = u_m = 0.74(1)$.

x_0/a	$n=0$	$n=1$	$n=2$	$n=3$	$n=4$	$n=5$
0	$2.9921(9) \times 10^3$	$2.9962(9) \times 10^3$	$3.0079(9) \times 10^3$	$3.0260(9) \times 10^3$	$3.0496(9) \times 10^3$	$3.0774(9) \times 10^3$
1	$9.200(5) \times 10^1$	$9.335(5) \times 10^1$	$9.698(5) \times 10^1$	$1.0213(5) \times 10^2$	$1.0813(5) \times 10^2$	$1.1447(5) \times 10^2$
2	$5.65(1) \times 10^0$	$6.27(1) \times 10^0$	$7.83(1) \times 10^0$	$9.77(1) \times 10^0$	$1.171(1) \times 10^1$	$1.343(1) \times 10^1$
3	$1.566(6) \times 10^0$	$1.903(5) \times 10^0$	$2.681(5) \times 10^0$	$3.527(4) \times 10^0$	$4.222(4) \times 10^0$	$4.699(5) \times 10^0$
4	$5.19(5) \times 10^{-1}$	$7.10(4) \times 10^{-1}$	$1.117(3) \times 10^0$	$1.491(3) \times 10^0$	$1.721(3) \times 10^0$	$1.801(3) \times 10^0$
5	$4.02(5) \times 10^{-1}$	$5.08(4) \times 10^{-1}$	$7.11(3) \times 10^{-1}$	$8.58(2) \times 10^{-1}$	$9.00(2) \times 10^{-1}$	$8.59(2) \times 10^{-1}$
6	$3.84(5) \times 10^{-1}$	$4.34(4) \times 10^{-1}$	$5.16(3) \times 10^{-1}$	$5.46(2) \times 10^{-1}$	$5.14(1) \times 10^{-1}$	$4.44(1) \times 10^{-1}$
7	$3.77(5) \times 10^{-1}$	$3.90(4) \times 10^{-1}$	$3.95(3) \times 10^{-1}$	$3.64(2) \times 10^{-1}$	$3.06(1) \times 10^{-1}$	$2.386(7) \times 10^{-1}$
8	$3.72(5) \times 10^{-1}$	$3.59(4) \times 10^{-1}$	$3.16(2) \times 10^{-1}$	$2.54(1) \times 10^{-1}$	$1.887(9) \times 10^{-1}$	$1.319(6) \times 10^{-1}$
9	$3.68(5) \times 10^{-1}$	$3.37(4) \times 10^{-1}$	$2.64(2) \times 10^{-1}$	$1.85(1) \times 10^{-1}$	$1.217(8) \times 10^{-1}$	$7.55(5) \times 10^{-2}$
10	$3.66(5) \times 10^{-1}$	$3.23(4) \times 10^{-1}$	$2.30(2) \times 10^{-1}$	$1.44(1) \times 10^{-1}$	$8.35(8) \times 10^{-2}$	$4.59(5) \times 10^{-2}$
11	$3.65(5) \times 10^{-1}$	$3.15(4) \times 10^{-1}$	$2.11(2) \times 10^{-1}$	$1.21(1) \times 10^{-1}$	$6.37(7) \times 10^{-2}$	$3.11(5) \times 10^{-2}$
12	$3.65(5) \times 10^{-1}$	$3.13(4) \times 10^{-1}$	$2.06(2) \times 10^{-1}$	$1.14(1) \times 10^{-1}$	$5.77(8) \times 10^{-2}$	$2.67(6) \times 10^{-2}$

Table 6.11: Renormalized correlation function $G_A(x_0, T, \mathbf{p}_n)/T^3$ for the 24×64^3 finite-T ensemble, with T=1/24a. All errors quoted are statistical.

m_π/T	2.15(2)
f_π/T	0.57(2)
u_f	0.88(3)
u_m	0.848(15)
u_f/u_m	1.04(3)

Table 6.12: Summary of the main results for the thermal ensemble of size 16×48^3 at 150 MeV. All renormalization factors are included and the errors are purely statistical.

Chapter 7

Conclusions

This work represents a step towards understanding the degrees of freedom dictating the static correlations and the dynamical properties of QCD in its low-temperature phase. We have computed the two temperature-dependent parameters that determine the pion quasiparticle dispersion relation (see Eq. (6.1.2)) and tested its validity at non-vanishing momentum.

The energy cost of giving the pion quasiparticle a momentum is significantly reduced, since the 'velocity' is well below unity. We have tested that the pion indeed admits a modified dispersion relation, Eq. (6.4.6), by analyzing lattice two-point functions. The test is based on requiring the consistency with the lattice data of the combined chiral prediction for the dispersion relation and the residue of the pion pole in the two-point function of the axial-charge density.

The Backus-Gilbert Method has been proven to be a useful tool for spectral function reconstruction which to our knowledge was never applied to QCD before. The realistic Mock-data analysis of Appendix F shows that applying the method in a first step can be useful in narrowing down the region of frequency where a specific ansatz for the spectral function must be made. In addition, the procedure of calculating residues associated with single δ-type states appears to be very robust.

We have shown that shifted boundary conditions in time represent a substantial practical advantage that provides a way to perform fine temperature scans. We have used shifted boundary conditions to renormalize the energy-momentum-tensor in SU(3) Yang-Mills theory. The knowledge of this renormalization constant is crucial in order to determine transport coefficients from the slope of spectral

functions at the origin. Nevertheless, a full application of this method to a theory with fermions has not yet been done. It could be subject of future work.

All methods introduced can be applied to ensembles with a quark content closer to the real world: it would be very interesting to compute all observables considered here on QCD ensembles with up, down and strange quarks at their physical masses (see the recent [121]). In order to test the $T = 0$ chiral effective theory predictions more stringently, additional simulations at temperatures 100-150MeV are required at lighter quark masses. The comparisons with the available two-loops calculations in chiral perturbation theory [94, 95] could then be done systematically. Also determining the dispersion relation of a non-Goldstone hadron would be interesting to see whether the relatively strong change we have seen in the pion properties is specific to chiral dynamics. In general, a kinetic theory description allows one to use as primary degrees of freedom the quasiparticles specific to the temperature of interest. It is therefore much broader in applicability than the hadron resonance gas model, but requires input information on the quasiparticles. The problem treated here illustrates the importance of having guidance from an effective theory in reconstructing the gross features of the spectral function. Having a higher resolution in momentum could help in assessing the region of validity of the chiral effective theory; for example with twisted boundary conditions. Our conclusions could be strengthened further by repeating the calculation at smaller quark masses and with higher statistics.

In order to conclude, one can surely say that there is still a lot of room for ideas within the field of finite temperature strongly coupled systems. As far as systematic controllable errors are concerned, Lattice Gauge Theory appears to be the best tool to gain information about this systems. In relation to QCD, there are open problems that need better understanding: the picture of the phase diagram is still incomplete and the role of the axial anomaly around the phase transition is not well understood either. One should also work towards the definition of cleaner observables that can be measured accurately in experiments and compared to Lattice results at finite temperature in an easy manner. On the lattice side, a coordinated lattice simulation effort at finite temperature could represent a substantial step in the right direction.

Gamma matrices and conventions

Throughout this work natural units are used

$$\hbar = c = 1. \tag{A.0.1}$$

We use the euclidean version of the gamma matrices satisfying

$$\{\gamma_\mu, \gamma_\nu\} = 2\delta_{\mu\nu}\mathbb{I}. \tag{A.0.2}$$

In the chiral representation, γ_5 is diagonal and anti-commutes with all other gamma matrices. They read

$$\gamma_0 = \begin{pmatrix} 0 & 0 & 1 & 0 \\ 0 & 0 & 0 & 1 \\ 1 & 0 & 0 & 0 \\ 0 & 1 & 0 & 0 \end{pmatrix}, \gamma_1 = \begin{pmatrix} 0 & 0 & 0 & -i \\ 0 & 0 & -i & 0 \\ 0 & i & 0 & 0 \\ i & 0 & 0 & 0 \end{pmatrix}, \gamma_2 = \begin{pmatrix} 0 & 0 & 0 & -1 \\ 0 & 0 & 1 & 0 \\ 0 & 1 & 0 & 0 \\ -1 & 0 & 0 & 0 \end{pmatrix}, \gamma_3 = \begin{pmatrix} 0 & 0 & -i & 0 \\ 0 & 0 & 0 & i \\ i & 0 & 0 & 0 \\ 0 & -i & 0 & 0 \end{pmatrix},$$

$$\gamma_5 = \gamma_0\gamma_1\gamma_2\gamma_3 = \begin{pmatrix} 1 & 0 & 0 & 0 \\ 0 & 1 & 0 & 0 \\ 0 & 0 & -1 & 0 \\ 0 & 0 & 0 & -1 \end{pmatrix}. \tag{A.0.3}$$

For all 5 matrices it is true that

$$\gamma = \gamma^\dagger = \gamma^{-1}, \qquad \gamma^2 = \mathbb{I}. \tag{A.0.4}$$

Improved derivatives

Derivatives are at the origin of cutoff effects. Therefore a systematic improvement of differential operators is of key importance. One defines forward and backwards acting derivatives on some field $\phi(n)$ as

$$\partial_\mu \phi(n) = \frac{1}{a} \left(\phi(n + \hat{\mu}) - \phi(n) \right) + \mathcal{O}(a) \tag{B.0.1}$$

$$\partial_\mu^* \phi(n) = \frac{1}{a} \left(\phi(n) - \phi(n - \hat{\mu}) \right) + \mathcal{O}(a). \tag{B.0.2}$$

The symmetric derivative is free of $\mathcal{O}(a)$ effects

$$\overline{\partial}_\mu \phi(n) = \frac{1}{2} \left(\partial_\mu \phi(n) + \partial_\mu^* \phi(n) \right) = \frac{1}{2a} \left(\phi(n + \hat{\mu}) - \phi(n - \hat{\mu}) \right) + \mathcal{O}(a^2). \tag{B.0.3}$$

One can further improve the derivative to the next order by making the replacement [49]

$$\overline{\partial}_\mu \phi(n) \;\to\; \overline{\partial}_\mu \phi(n) \left(1 - \frac{1}{6} a^2 \partial_\mu^* \partial_\mu \phi(n) \right) \tag{B.0.4}$$

$$= \frac{1}{12a} \left(8\phi(n + \hat{\mu}) - 8\phi(n - \hat{\mu}) - \phi(n + 2\hat{\mu}) + \phi(n - 2\hat{\mu}) \right),$$

which has $\mathcal{O}(a^4)$ discretization errors. The same operation can be done for the second derivative which leads then to the laplacian (if summed over μ)

$$\partial_\mu^* \partial_\mu \;\to\; \partial_\mu^* \partial_\mu (1 - \frac{1}{12} a^2 \partial_\mu^* \partial_\mu) \tag{B.0.5}$$

$$= \frac{1}{12a^2} \left(16\phi(n + \hat{\mu}) - 30\phi(n) + 16\phi(n - \hat{\mu}) - \phi(n - 2\hat{\mu}) - \phi(n + 2\hat{\mu}) \right).$$

Notice how in every improvement step, more distant neighbors are involved in the definition of the derivative at point n. Therefore we are removing cutoff effects at the cost of reducing the locality property of the theory.

Appendix C

Error analysis

The mean value of any observable calculated on the lattice is

$$\bar{X} = \frac{1}{N} \sum_{j=1}^{N} X_j \tag{C.0.1}$$

where N is the number of configurations. The error is calculated via the jackknife procedure, where one first generates N jackknife replica x_i^J according to

$$x_i^J = \frac{1}{N-1} \sum_{j \neq i}^{N} X_j \tag{C.0.2}$$

All calculations are done on the mean value and on the jackknifed replica. In this way the error can be calculated simply as

$$\Delta f(\bar{X}) = \sqrt{\frac{N-1}{N} \sum_i (f(x_i^J) - f(\bar{X}))^2} \tag{C.0.3}$$

Notice the corrective factor of $(N-1)$ in the numerator. This appears in order to correct the effect that each x_i^J is much closer to $\bar{X}$ than the old values X_i. In this way we avoid working with the set $\{X_i\}$ that is much noisier.

C.1   Autocorrelation effects: binning

One should always study autocorrelation effects in the data. For this purpose one defines the autocorrelation function

$$\rho(t) = \frac{\Gamma(t)}{\Gamma(0)} = \frac{1}{\Gamma(0)} \left(\frac{1}{N-t} \sum_{i=1}^{N-t} (X_i - \bar{X})(X_{i+t} - \bar{X}) \right) \qquad \text{(C.1.1)}$$

where t represents Montecarlo time. The error on this function can be estimated according to Appendix E of [122] as

$$\Delta\rho(t) = \sqrt{\frac{1}{N} \sum_{i=1}^{t+\Lambda} (\rho(i+t) + \rho(i-t) - 2\rho(i)\rho(t))^2} \qquad \text{(C.1.2)}$$

where the choice of the cutoff Λ is not critical and values $\sim 10^2$ give consistent results. Typically, $\rho(t)$ is an exponentially decaying function with some correlation length τ, $\rho(t) \sim e^{-t/\tau}$. In the case that τ is large, autocorrelation effects are big which would lead to an underestimation of the error. A possible technique for taking those into account is binning. Before the generation of the jackknife replica one averages the data over some bin size length N_b

$$x_i^B = \frac{1}{N_b} \sum_{j=N_b(i-1)+1}^{iN_b} X_j \qquad i = 1, ..., N/N_b \qquad \text{(C.1.3)}$$

The set $\{x_i^B\}$ is used as input in Eq. (C.0.2) replacing X_i with X_i^B and N with N/N_b. The error dependence of some quantity with the bin size N_b is such that it grows until it reaches a saturation level at some critical bin size. This value of the bin size should be further used in the analysis for a conservative error estimation. A lot of useful information regarding error analysis can be found in [123].

C.2   An example of error analysis on $G_A(\beta/2)$

The tools presented in the previous section can be applied to a particular case. We choose the midpoint of the axial charge euclidean correlator in the C1 scan at a couple of temperatures since the dominance of the pion contribution at this point is a crucial assumption for the consistency of the effective theory used through-

out this work. In our analysis of Sec. 6.3 the data were prebinned by averaging over five consecutive configurations. We want to study in more detail the effect of autocorrelations. In Fig. C.1 the autocorrelation $\rho(t)$ is shown for a handful of temperatures. While at the lower temperatures autocorrelation effects are clearly small, as one approaches the phase transition the effect becomes bigger and becomes worst at $T = 209$MeV which happens to be the critical temperature quoted in [99]. It is clear then that the transition region has a clear effect on the autocorrelations produced by the algorithm we employed. One should be aware of this fact for the future generation of configurations.

In Fig. C.2 we illustrate the dependence of the estimated error bars on the bin size. Disregarding binsize 20 which is already quite uncertain since the number of jackknife bins is ≈ 15, we see no significant effect at the two lower temperatures which points to the evidence that the saturation level is reached. In contrast, between 194-209 MeV a systematic trend of growing error bars is visible. Nevertheless, we cannot resolve due to lack of statistics whether the error quoted with bin size 5 is close to the saturation level. This does not affect any physics conclusion since we do not make any claim concerning the pion and its properties deep in the transition region.
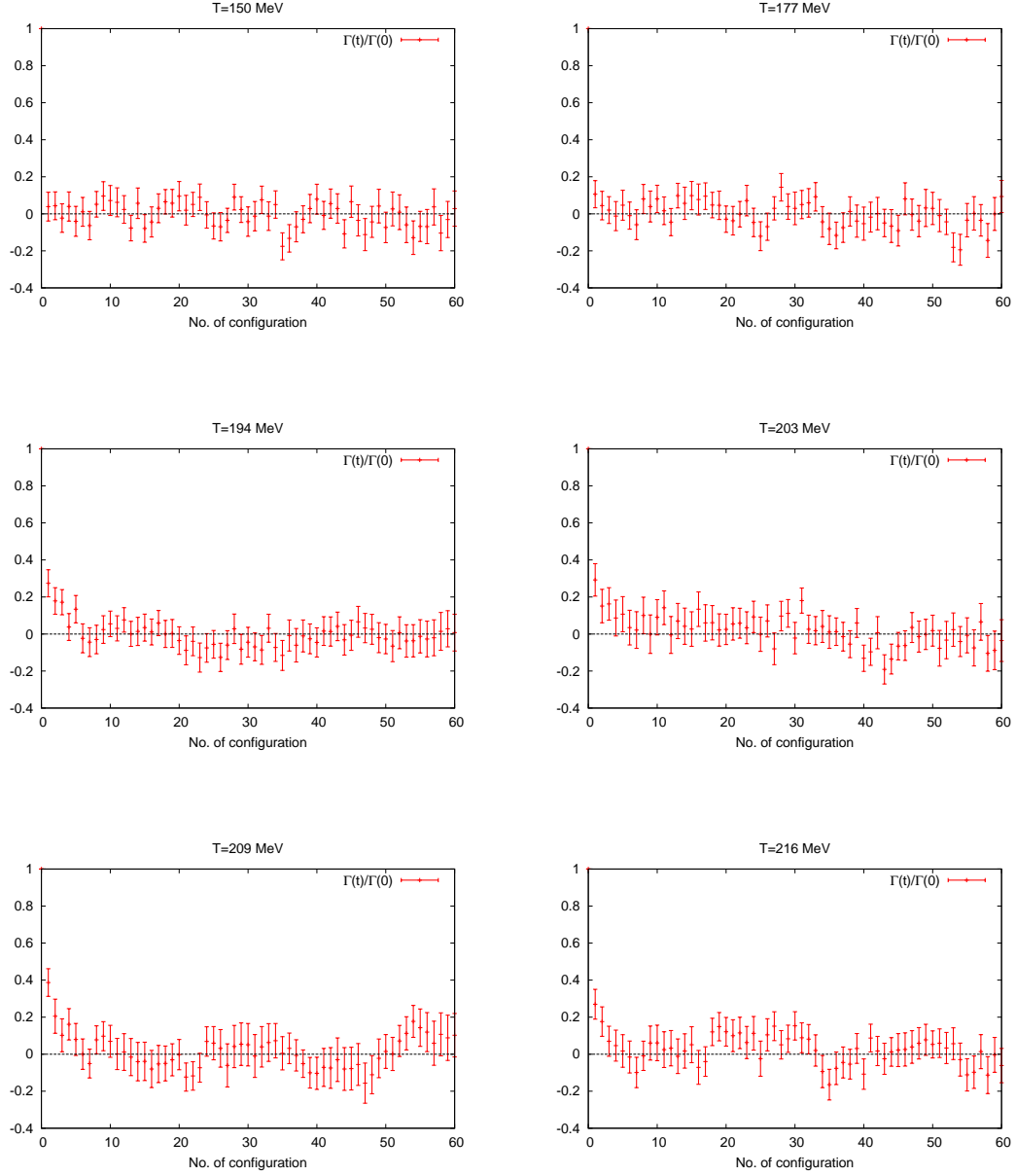
Figure C.1: The autocorrelation function $\rho(t)$ of the observable $G_A(\beta/2)$ for six ensembles of the temperature scan C1 as a function of the configuration number. Consecutive configurations are separated by 10 units of molecular dynamics time. The uncertainty on $\rho(t)$ was estimated using the formula written in Eq. (C.1.2).
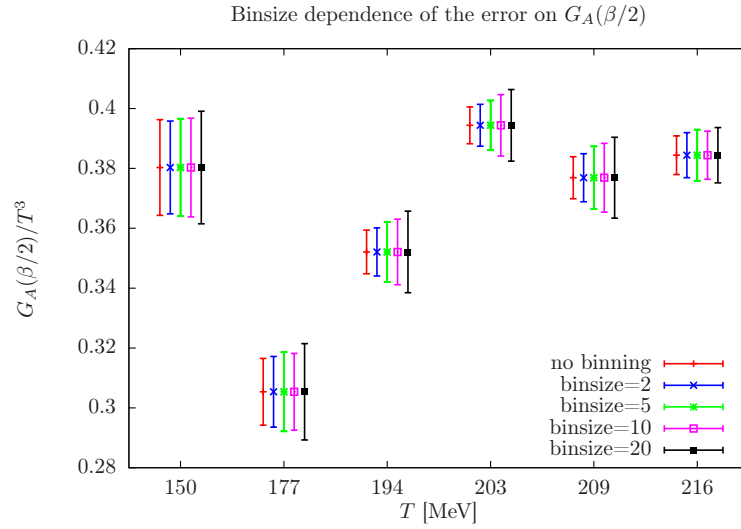
Figure C.2: Effects on the estimated uncertainty of the observable $G_A(\beta/2)$ on the scan C1 of binning the data before applying the jackknife method.

Appendix D

Fitting correlation functions

After having produced configurations and calculated mesonic 2pt-functions, extracting physical information from these correlation functions is usually done via fits.

D.1 Calculating amplitudes

Using the spectral decomposition we know that a given state n contributes to a generic 2pt-correlation function as

$$\int d^3x \, \langle O_1(x)O_2(0)\rangle = \langle 0| \, O_1(x) \, |n\rangle \, \langle n| \, O_2(0) \, |0\rangle \, e^{-tE_n} \tag{D.1.1}$$

(see Eq. (4.8.4)). In practical situations the finiteness of the time extension, although periodic, gives rise to a backwards propagating state with the same energy. Therefore, a common practice is to average the correlation functions around the midpoint enforcing the property $f(t) = f(\beta - t)$ and consequently one uses data points in the range $[0, \beta/2]$. Restricting our discussion to the ground state at zero momentum which has the lowest energy and therefore decays slower than any other state, a valid fit ansatz is

$$f(t) = |A_0|^2 e^{-m_0 t} = B_0 \cosh(m_0(\beta/2 - t)) \tag{D.1.2}$$

where $|A_0|^2 = \langle 0| \, O_1(x) \, |n\rangle \, \langle n| \, O_2(0) \, |0\rangle$ and in most cases of interest $O_1 = O_2 = O = \pm O^\dagger$. The relation between $|A_0|^2$ and B_0 is then easily derived. Dividing

Eq. (D.1.2) by $\sinh(m_0\beta/2)$ we arrive at

$$\frac{|A_0|^2 e^{-m_0 t}}{\sinh(m_0\beta/2)} = B_0 e^{-m_0 t} + O(e^{-m_0\beta}) \qquad \text{(D.1.3)}$$

and if $m_0\beta \gg 1$ we arrive at the master equation

$$|A|^2 = B_0 \sinh(m_0\beta/2). \qquad \text{(D.1.4)}$$

D.2   Effective mass-plots: coshmass

For calculating m_0 we make use of the "coshmass". We can write the identity

$$\frac{f(t)}{f(t+a)} = \frac{\cosh(m_0(t-\beta/2))}{\cosh(m_0(t+a-\beta/2))} \qquad \text{(D.2.1)}$$

where the constant B_0 drops out. The positive root of the previous equation defines a function $m_0^{\mathrm{cosh}}(t+a/2)$ that eventually, for big values of t, will reach a constant value (within statistical uncertainty). The plateau is observed as soon as all excited states have died out and the single ground state remains. A fit to a constant in the plateau range leads then to the extraction of m_0. This plot is also useful for estimating the optimal fit window that needs to be considered when a direct fit to the correlation function is done (for example for calculating the amplitude $|A_0|^2$ as in Sec. D.1.) Throughout the thesis we have used the Levenberg-Marquardt method for fitting purposes which is explained in detail in [56].

Chiral Ward identities for two-point functions

The isovector vector and axial-vector currents, as well as the pseudoscalar density were defined in Eq. (6.2.1). We use the Euclidean field theory method to derive the axial Ward identities [100]. We assume that all chemical potentials are set to zero. It is useful to recall some of the space-time transformation properties of these local operators. Under the Euclidean time reversal tranformation $(x_0' = -x_0,\ \vec{x}' = \vec{x})$, we have

$$A_0^{a\prime}(x') = A_0^a(x), \qquad A_k^{a\prime}(x') = -A_k^a(x), \qquad P^{a\prime}(x') = -P^a(x), \tag{E.0.1}$$

while under $(x' = -x)$

$$A_\mu^{a\prime}(x') = -A_\mu^a(x), \qquad P^{a\prime}(x') = P^a(x). \tag{E.0.2}$$

We also note that V_μ is odd under charge conjugation C, while P and A_μ are even.

The variations of the quark and antiquark fields under an infinitesimal, isovector, axial phase rotation read

$$\delta_A^a \psi(x) \ = \tfrac{1}{2}\tau^a \gamma_5 \psi(x), \qquad\qquad \delta_A^a \bar\psi(x) \ = \bar\psi(x)\gamma_5 \tfrac{1}{2}\tau^a. \tag{E.0.3}$$

They lead to the following transformation of the composite operators,

$$\delta_A^a A_\mu^b(x) = -i\epsilon^{abc} V_\mu^c(x), \qquad \delta_A^a P^b(x) = \frac{\delta^{ab}}{2}\bar\psi\psi, \tag{E.0.4}$$

For an axial transformation parameter $\alpha^a(x)$, the variation of the action is given by [57]

$$\delta S = \int d^4x \left(\partial_\mu \alpha(x)^a A^a_\mu(x) + \alpha(x)^a 2m \, P^a(x) \right). \qquad \text{(E.0.5)}$$

In the path integral, the invariance of the integration measure under the transformation above leads to $\langle \delta \mathcal{O} \rangle = \langle \mathcal{O} \delta S \rangle$. In particular, if $\mathcal{O}$ consists of one local field located at the point y,

$$\alpha(y) \langle \delta^a_A \mathcal{O}(y) \rangle = \langle \mathcal{O}(y) \int d^4x \left(\partial_\mu \alpha(x) A^a_\mu(x) + \alpha(x) 2m \, P^a(x) \right) \rangle \qquad \text{(E.0.6)}$$

In the following we set $\alpha(x) = e^{ikx}$ and consider several choices for $\mathcal{O}$. Choosing $\mathcal{O} = A^b_\nu$, we obtain

$$0 = ik_\mu \langle A^b_\nu(0) \int d^4x \, e^{ikx} A^a_\mu(x) \rangle + 2m \int d^4x \, e^{ikx} \langle A^b_\nu(0) P^a(x) \rangle. \qquad \text{(E.0.7)}$$

Choosing instead $\mathcal{O} = P^b$, we obtain

$$\frac{1}{2} \delta^{ab} \langle \bar{\psi}\psi \rangle = ik_\mu \langle P^b(0) \int d^4x \, e^{ikx} A^a_\mu(x) \rangle + 2m \langle P^b(0) \int d^4x \, e^{ikx} P^a(x) \rangle. \qquad \text{(E.0.8)}$$

These are the momentum-space versions of the Ward identities, while Eq. (6.2.3)–Eq. (6.2.4) are the position-space versions.

E.1 A sum rule for the spectral function of the axial charge density

Combining Eq. (E.0.7) and Eq. (E.0.8), one finds

$$k_\mu k_\nu \int d^4x \, e^{ikx} \, \langle A^b_\nu(0) A^a_\mu(x) \rangle = -m \delta^{ab} \langle \bar{\psi}\psi \rangle + 4m^2 \int d^4x \, e^{ikx} \, \langle P^b(0) P^a(x) \rangle. \qquad \text{(E.1.1)}$$

Next we consider the difference of this relation at finite temperature and at zero temperature. The operator-product expansion indicates that the most singular contributions arise from dimension four operators. By power counting, all the correlators appearing in (E.1.1) are then expected to be finite. More precisely, for large k_0 and finite quark mass, all correlators in (E.1.1) are of order k_0^{-2}. The

left-hand side of the equation has a finite contribution when $k_0 \to \infty$ given by the $\int d^4x \, e^{ikx} \langle A_0 A_0 \rangle|_0^T$ correlator, since it is multiplied by k_0^2. On the right-hand side, the only surviving term is given by the condensate. The coefficient of the $\mathrm{O}(k_0^{-2})$ term of the $\int d^4x \, e^{ikx} \langle A_0^a(0) A_0^b(x) \rangle|_0^T$ correlator must thus equal $-m\delta^{ab}\langle \bar{\psi}\psi \rangle|_0^T$ and it cannot contain logarithms of k_0. To convert this statement into a property of the spectral function, we use the spectral representation (see for instance [12])

$$\int d^4x \, e^{ikx} \left. \langle A_0^b(0) A_0^a(x) \rangle \right|_0^T = \delta^{ab} \int_{-\infty}^{\infty} d\omega \, \frac{\omega}{\omega^2 + k_0^2} \left. \rho_{\mathrm{A}}(\omega, k) \right|_0^T. \tag{E.1.2}$$

The absence of logarithms in the coefficient of k_0^{-2} on the left-hand side of Eq. (E.1.2) indicates that $\omega \rho_{\mathrm{A}}(\omega, \vec{k})|_0^T$ is integrable [124]. Expanding the integrand on the right-hand side of Eq. (E.1.2) to order k_0^{-2} we then obtain

$$\int_{-\infty}^{\infty} d\omega \, \omega \, \left. \rho_{\mathrm{A}}(\omega, \vec{k}) \right|_0^T = -m \langle \bar{\psi}\psi \rangle \Big|_0^T. \tag{E.1.3}$$

E.2 Tensor structure of the axial current two-point functions

We work in the Euclidean field theory and define the correlation function in momentum space as

$$\delta^{ab} \Pi_{\mu\nu}^{\mathrm{A}}(\hat{\epsilon}, k) \equiv \int d^4x \, e^{ik\cdot x} \langle A_\mu^a(x) A_\nu^b(0) \rangle_{\hat{\epsilon}}. \tag{E.2.1}$$

The unit vector $\hat{\epsilon}$ points in the direction that defines the thermal boundary condition. It is $\hat{\epsilon} = (1, 0, 0, 0)$ in the rest frame of the thermal system. By doing the change of integration variables $x \to -x$ and using translation invariance

$$\langle A_\mu(-x) A_\nu(0) \rangle_{\hat{\epsilon}} = \langle A_\nu(x) A_\mu(0) \rangle_{\hat{\epsilon}} \tag{E.2.2}$$

and symmetry under the O(4) rotation $x \to -x$,

$$\langle A_\mu(-x) A_\nu(0) \rangle_{\hat{\epsilon}} = \langle A_\mu(x) A_\nu(0) \rangle_{-\hat{\epsilon}}, \tag{E.2.3}$$

we have the symmetries

$$\Pi^{\mathrm{A}}_{\mu\nu}(\hat{\epsilon}, k) = \Pi^{\mathrm{A}}_{\nu\mu}(\hat{\epsilon}, -k) = \Pi^{\mathrm{A}}_{\mu\nu}(-\hat{\epsilon}, -k). \tag{E.2.4}$$

To write down the tensor decomposition, we have the building blocks $\delta_{\mu\nu}$, k_μ and $\hat{\epsilon}_\mu$ at our disposal. We can write down four structures that respect the symmetries (E.2.4),

$$\delta_{\mu\nu}, \qquad \frac{k_\mu k_\nu}{k^2}, \qquad \frac{\hat{\epsilon} \cdot k}{k^2}(\hat{\epsilon}_\mu k_\nu + k_\mu \hat{\epsilon}_\nu), \qquad \hat{\epsilon}_\mu \hat{\epsilon}_\nu. \tag{E.2.5}$$

We can form one projector to the subspace orthogonal to both $\hat{\epsilon}$ and k,

$$C^{\mathrm{T,t}}_{\mu\nu} = \delta_{\mu\nu} - \frac{1}{1 - (\hat{\epsilon} \cdot k)^2/k^2}\left(\hat{\epsilon}_\mu \hat{\epsilon}_\nu + \frac{k_\mu k_\nu}{k^2} - \frac{1}{k^2}(\hat{\epsilon} \cdot k)(\hat{\epsilon}_\mu k_\nu + k_\mu \hat{\epsilon}_\nu)\right), \tag{E.2.6}$$

and one projector onto the component of $\hat{\epsilon}$ which is orthogonal to k,

$$C^{\mathrm{T,l}}_{\mu\nu} = \delta_{\mu\nu} - \frac{k_\mu k_\nu}{k^2} - C^{\mathrm{T,t}}_{\mu\nu} = \frac{1}{1 - (\hat{\epsilon} \cdot k)^2/k^2}\left(\hat{\epsilon}_\mu - \frac{(\hat{\epsilon} \cdot k)k_\mu}{k^2}\right)\left(\hat{\epsilon}_\nu - \frac{(\hat{\epsilon} \cdot k)k_\nu}{k^2}\right). \tag{E.2.7}$$

Two possible non-transverse combinations are

$$C^{\mathrm{L,l}}_{\mu\nu} = \frac{k_\mu k_\nu}{k^2}, \qquad C^{\mathrm{M}}_{\mu\nu} = \frac{1}{1 - (\hat{\epsilon} \cdot k)^2/k^2}\left(\hat{\epsilon}_\mu \hat{\epsilon}_\nu - (\hat{\epsilon} \cdot k)^2 \frac{k_\mu k_\nu}{(k^2)^2}\right). \tag{E.2.8}$$

The first one is the projector onto the direction of k_μ. The second tensor, while not a projector, has the properties

$$C^{\mathrm{M}}_{\mu\mu} = 1, \qquad C^{\mathrm{T,t}}_{\mu\alpha} C^{\mathrm{M}}_{\alpha\nu} = C^{\mathrm{L,l}}_{\mu\alpha} C^{\mathrm{M}}_{\alpha\nu} = 0. \tag{E.2.9}$$

In summary, we can write

$$\Pi^{\mathrm{A}}_{\mu\nu}(\hat{\epsilon}, k) = C^{\mathrm{T,t}}_{\mu\nu} \Pi^{\mathrm{T,t}} + C^{\mathrm{T,l}}_{\mu\nu} \Pi^{\mathrm{T,l}} + C^{\mathrm{L,l}}_{\mu\nu} \Pi^{\mathrm{L,l}} + C^{\mathrm{M}}_{\mu\nu} \Pi^{\mathrm{M}}. \tag{E.2.10}$$

The argument of the C's is $(\hat{\epsilon}, k)$, while the argument of the form factors Π is $(\hat{\epsilon} \cdot k, k^2)$.

It is helpful to be able to invert the relation Eq. (E.2.10) in order to project

out the form factors individually. We find

$$\Pi^{\mathrm{L},\mathrm{l}} \;=\; \frac{k_\mu k_\nu}{k^2}\Pi^A_{\mu\nu}, \tag{E.2.11}$$

$$\Pi^{\mathrm{M}} \;=\; \frac{1}{\hat{\epsilon}\cdot k}\,k_\mu\Pi^A_{\mu\nu}(\hat{\epsilon}_\nu - \frac{\hat{\epsilon}\cdot k}{k^2}k_\nu), \tag{E.2.12}$$

$$\Pi^{\mathrm{T},\mathrm{l}} = \frac{1}{1-(\hat{\epsilon}\cdot k)^2/k^2}\left[\hat{\epsilon}_\mu\Pi^A_{\mu\nu}\hat{\epsilon}_\nu - \frac{(\hat{\epsilon}\cdot k)^2}{(k^2)}\Pi^{\mathrm{L},\mathrm{l}} - (1+(\hat{\epsilon}\cdot k)^2/k^2)\,\Pi^{\mathrm{M}}\right], \tag{E.2.13}$$

$$\Pi^{\mathrm{T},\mathrm{t}} = \frac{1}{2}\left\{\Pi^A_{\mu\mu} - \left[\Pi^{\mathrm{T},\mathrm{l}} + \Pi^{\mathrm{M}} + \Pi^{\mathrm{L},\mathrm{l}}\right]\right\}. \tag{E.2.14}$$

E.2.1   Special kinematics

When $(\hat{\epsilon}\cdot k)^2 = k^2$, corresponding to vanishing spatial momentum in the rest frame of the thermal system, the projectors $C^{\mathrm{T},\mathrm{t}}_{\mu\nu}$ and $C^{\mathrm{T},\mathrm{l}}_{\mu\nu}$ as well as $C^{\mathrm{M}}_{\mu\nu}$ become singular. Therefore we will define the value of the form factors in this limit by continuity. When $\hat{\epsilon}$ and k are collinear, there are only two independent tensor structures,

$$\Pi^{A,\mathrm{col}}_{\mu\nu}(\hat{\epsilon}, k) = \left(\delta_{\mu\nu} - \frac{k_\mu k_\nu}{k^2}\right)\hat{\Pi}_{\mathrm{T}}(k^2) + \frac{k_\mu k_\nu}{k^2}\hat{\Pi}_{\mathrm{L}}(k^2). \tag{E.2.15}$$

Applying the relevant projectors as in Eqs. (E.2.11–E.2.14), one finds that

$$\Pi^{\mathrm{T},\mathrm{t}} = \Pi^{\mathrm{T},\mathrm{l}} = \hat{\Pi}_{\mathrm{T}}, \qquad \Pi^{\mathrm{L},\mathrm{l}} = \hat{\Pi}_{\mathrm{L}}, \qquad \Pi^{\mathrm{M}} = 0. \tag{E.2.16}$$

When $\hat{\epsilon}\cdot k = 0$, corresponding to the static correlators, $C^{\mathrm{T},\mathrm{l}}_{\mu\nu}$ becomes equal to $C^{\mathrm{M}}_{\mu\nu}$. Therefore, in that situation the Euclidean correlator is only sensitive to the sum of the two corresponding form factors, $(\Pi^{\mathrm{M}} + \Pi^{T,l})$. Eq. (E.2.12) nonetheless provides an unambiguous definition of Π^{M} if, expressed in the rest frame, $\lim_{k_0\to 0}\Pi^A_{0i}/k_0$ is known. The latter limit, however, requires an analytic continuation of the Euclidean correlator.

E.2.2   The zero-temperature limit

At zero temperature, it is natural to parametrize the correlation function as

$$\Pi^A_{\mu\nu}(k) = \left(\delta_{\mu\nu} - \frac{k_\mu k_\nu}{k^2}\right)\Pi^{\mathrm{T}}(k^2) + \frac{k_\mu k_\nu}{k^2}\Pi^{\mathrm{L}}(k^2). \tag{E.2.17}$$

Applying the same projectors as in Eqs. (E.2.11–E.2.14) onto the correlation function (E.2.17), and requiring that the same result be obtained in the zero-temperature limit, we obtain

$$\Pi^{\mathrm{L,l}}(\hat{\epsilon}\cdot k, k^2) \;\longrightarrow\; \Pi^{\mathrm{L}}(k^2), \tag{E.2.18}$$

$$\Pi^{\mathrm{M}}(\hat{\epsilon}\cdot k, k^2) \;\longrightarrow\; 0, \tag{E.2.19}$$

$$\Pi^{\mathrm{T,l}}(\hat{\epsilon}\cdot k, k^2) \;\longrightarrow\; \Pi^{\mathrm{T}}(k^2), \tag{E.2.20}$$

$$\Pi^{\mathrm{T,t}}(\hat{\epsilon}\cdot k, k^2) \;\longrightarrow\; \Pi^{\mathrm{T}}(k^2). \tag{E.2.21}$$

E.2.3   Relation to the correlators of the pseudoscalar density

We define

$$\delta^{ab}\mathcal{A}_\mu(\hat{\epsilon}, k) \;=\; \int d^4x\; e^{ikx}\, \langle A_\mu^a(x)\, P^b(0)\rangle, \tag{E.2.22}$$

$$\delta^{ab}\mathcal{P}(\hat{\epsilon}, k) \;=\; \int d^4x\; e^{ikx}\, \langle P^a(x)\, P^b(0)\rangle. \tag{E.2.23}$$

We note the symmetry relations

$$\mathcal{A}_\mu(\hat{\epsilon}, k) = -\mathcal{A}_\mu(-\hat{\epsilon}, -k), \tag{E.2.24}$$

$$\int d^4x\; e^{ikx}\, \langle P(x)\, A_\nu(0)\rangle_{\hat{\epsilon}} = \mathcal{A}_\nu(\hat{\epsilon}, -k), \tag{E.2.25}$$

respectively from O(4) invariance and from translation invariance.

In [18], Eq. (A7) and (A8), taking into account Eq. (E.2.25) and Eq. (E.2.4), the Ward identities

$$2m\,\mathcal{A}_\mu(\hat{\epsilon}, k) \;=\; ik_\alpha\, \Pi^{\mathrm{A}}_{\mu\alpha}(\hat{\epsilon}, k), \tag{E.2.26}$$

$$4m^2\,\mathcal{P}(\hat{\epsilon}, k) \;=\; k_\mu \Pi^{\mathrm{A}}_{\mu\alpha}(\hat{\epsilon}, k)k_\alpha + m\langle\bar{\psi}\psi\rangle \tag{E.2.27}$$

were derived. Inserting our tensor decomposition of $\Pi^{\mathrm{A}}_{\mu\alpha}(\hat{\epsilon}, k)$, we find

$$2m\,\mathcal{A}_\mu(\hat{\epsilon}, k) = ik_\mu\, \Pi^{\mathrm{L,l}}(\hat{\epsilon}\cdot k, k^2) + i(\hat{\epsilon}\cdot k)\frac{\hat{\epsilon}_\mu - (\hat{\epsilon}\cdot k/k^2)\, k_\mu}{1 - (\hat{\epsilon}\cdot k)^2/k^2}\, \Pi^{\mathrm{M}}(\hat{\epsilon}\cdot k, k^2), \tag{E.2.28}$$

$$4m^2\,\mathcal{P}(\hat{\epsilon}, k) = k^2\, \Pi^{\mathrm{L,l}}(\hat{\epsilon}\cdot k, k^2) + m\,\langle\bar{\psi}\psi\rangle. \tag{E.2.29}$$

E.3   On the residue of the pion pole

In this appendix, we use the general results of the previous section in the rest frame of the thermal system, $\hat{\epsilon}_\mu = (1, 0, 0, 0)$. The form factors are thus functions of k_0 and k^2 and the dependence on $\hat{\epsilon}$ is no longer indicated explicitly. All expressions for correlation functions in this section refer exclusively to the pion contribution.

In [18], it was shown that the residue of the pion pole in the two-point function of A_0 at vanishing spatial momentum is $\mathrm{Res}(\omega_{\mathbf{0}}) = f_\pi^2 m_\pi^2$. In order to determine the form of the residue at finite momentum, we parametrize the residue as

$$\mathrm{Res}(\omega_{\mathbf{k}}) = f_\pi^2 (m_\pi^2 + \lambda \mathbf{k}^2). \tag{E.3.1}$$

To determine the parameter λ, we will exploit the fact that the spectral representation of the two-point function of A_0 in terms of real-time excitations must agree with the spectral representation in terms of screening states. From the former point of view, the pion contribution to the correlator in momentum space takes the form

$$\Pi_{00}^A(k) = \frac{f_\pi^2 (m_\pi^2 + \lambda \mathbf{k}^2)}{k_0^2 + \omega_{\mathbf{k}}^2}, \tag{E.3.2}$$

with $\omega_{\mathbf{k}}$ given in Eq. (6.4.6). From the 'screening' point of view, the residue must be proportional to k_0^2 at small k_0^2 (here we invoke the analytic continuation in the frequency, away from the Matsubara values $k_0 = 2\pi T n$). This is so because the screening pion is odd under the Euclidean time reversal $x_0 \to -x_0$, while A_0 is even. Thus we can write

$$\Pi_{00}^A(k) = \frac{-|F|^2 k_0^2}{\mathbf{k}^2 + \frac{k_0^2}{u^2} + m_\pi^2} \tag{E.3.3}$$

for some parameter F to be determined. Equations (E.3.2) and (E.3.3) must agree when the numerators are evaluated at the pole, $k_0^2 = -\omega_{\mathbf{k}}^2$. From here we learn the following,

$$|F| = \frac{f_\pi}{u^2}, \qquad \lambda = 1. \tag{E.3.4}$$

This shows in particular that the residue has the form given in Eq. (6.4.13). Essentially the same argument was already used in [18] to determine the residue of

the pion pole in the two-point function of the pseudoscalar density,

$$\mathcal{P}(k) = -\frac{\langle\bar{\psi}\psi\rangle^2 u^2}{4f_\pi^2}\frac{1}{k_0^2 + \omega_{\mathbf{k}}^2}.$$

(E.3.5)

We note that for a one-pole contribution, factorization relations such as

$$|\mathcal{A}_0(k)|^2 = |\mathcal{P}(k)|\,|\Pi_{00}^A(k)|$$

(E.3.6)

hold. The phase of $\mathcal{A}_0$ can then be determined through its form at vanishing spatial momentum given in [18].

E.3.1 The pion contribution to $\Pi_{\mu\nu}^A$

Having found the residue of the pion pole in the various two-point functions of the axial current, we give for completeness the pion contribution to the form factors defined in Eqs. (E.2.11–E.2.14),

$$\Pi^{\mathrm{L,l}}(k_0, k^2) = -\frac{f_\pi^2 m_\pi^4 u^2}{k^2(k_0^2 + \omega_{\mathbf{k}}^2)},$$

(E.3.7)

$$\Pi^{\mathrm{M}}(k_0, k^2) = \frac{f_\pi^2 m_\pi^2 \mathbf{k}^2(1 - u^2)}{k^2(k_0^2 + \omega_{\mathbf{k}}^2)},$$

(E.3.8)

$$\Pi^{\mathrm{T,l}}(k_0, k^2) = \frac{f_\pi^2 \mathbf{k}^2(1 - u^2)}{k_0^2 + \omega_{\mathbf{k}}^2},$$

(E.3.9)

$$\Pi^{\mathrm{T,t}}(k_0, k^2) = 0.$$

(E.3.10)

The first is obtained from Eq. (E.2.29), then the second from Eq. (E.2.28), the third by using Eq. (E.2.13) and the first two results. Via Eq. (E.2.10), the form factors allow one to obtain the entire tensor $\Pi_{\mu\nu}^A$.

These calculations could be greatly expedited by using an effective Lagrangian, as written down in [98]. However it is also instructive to derive the results above directly within QCD.

Mock-data study of the Backus-Gilbert method

In this appendix, we study the performance of the Backus-Gilbert method in a realistic lattice QCD application. We apply the method on mock data, where the underlying spectral function is known. Our goal is to validate the method used in section 6.5.6.

Our procedure is the following:

1. We start from a real lattice correlator computed on the 'zero' temperature ensemble O7 introduced in Sec. 6.5 and Table 6.7.

2. In order to construct a realistic model, a spectral function with sufficiently many free parameters is fitted to the lattice data.

3. The original correlator data is now replaced by mock data, namely the correlator obtained by integrating the fitted spectral function, with Gaussian noise added (using the original covariance matrix of the correlator).

4. The mock data is now fed into the Backus-Gilbert method, which generates a filtered spectral function $\hat{\rho}_{\mathrm{BG}}(\bar{\omega})$ and the resolution function $\delta(\bar{\omega}, \omega)$. The former is compared to the input spectral function.

5. The final step, as in section 6.5.6, is to assume that the true spectral function is dominated at low frequencies by the contribution of a stable particle (the pion), and we determine its residue in the correlator from $\hat{\rho}_{\mathrm{BG}}(\omega)$ and $\delta(\bar{\omega}, \omega)$. The result is compared with the input value.

F.1   Construction of realistic mock data

We use the Euclidean pseudo scalar density correlator projected onto zero momentum due to its good signal to noise ratio,

$$G_P(x_0)\delta^{ab} = -\int d^3x \left\langle P^a(x)P^b(0)\right\rangle. \tag{F.1.1}$$

In a first step, we want to obtain a fit function $G_P^{\text{fit}}(x_0)$ which describes the data. We employ the following fit ansatz for the spectral function,

$$\rho_P(\omega) = \frac{A_1}{2}e^{\omega_0\beta/2}\delta(\omega-\omega_0) + \frac{A_2 N_c}{(4\pi)^2}\theta(\omega-3\omega_0)\omega^2. \tag{F.1.2}$$

It contains a δ-type pion contribution at a low frequency ω_0 and a continuum of multi particle states beginning at threshold $\omega = 3\omega_0$ due to the negative parity of the pseudoscalar density operator. The corresponding correlator is given by[1]

$$
\begin{aligned}
G_P^{\text{fit}}(x_0) &= \int_0^\infty d\omega\rho_P(\omega)\left(e^{-\omega x_0} + e^{-\omega(\beta-x_0)}\right) \tag{F.1.3}\\
&= A_1\cosh(\omega_0(\beta/2-x_0))\\
&\quad + \frac{A_2 N_c}{(4\pi)^2}\left[\frac{e^{-3\omega_0 x_0}}{x_0^3}(2+6\omega_0 x_0+9\omega_0^2 x_0^2) + (x_0\to\beta-x_0)\right]. \tag{F.1.4}
\end{aligned}
$$

The fit to the data was performed in the interval $x_0/a \in [5,64]$ in order to avoid cut-off effects present a small distances. In view of Fig. F.1 one clearly sees that $G_P^{\text{fit}}(x_0)$ describes the data in a satisfactory way yielding an (uncorrelated) χ^2/d.o.f. $\sim 10^{-2}$ with fit parameters shown in Table F.1. Note that we do not quote statistical errors on the parameters A_1,ω_0 and A_2 since our goal is merely to construct realistic mock data.

The next step is to generate the correlator $G_P^{\text{fit}}(x_0)$ that corresponds to the fitted spectral function via the integral transform (F.1.3). In order to be as realistic as possible, we add Gaussian noise $\delta G_P^{\text{fit}}(x_0)$ to the correlator in order to obtain the mock data $\tilde{G}_P^{\text{fit}}$,

$$\tilde{G}_P^{\text{fit}}(x_0) = G_P^{\text{fit}}(x_0) + \delta G_P^{\text{fit}}(x_0). \tag{F.1.5}$$

The noise is generated by using the covariance matrix S_{ij} of the real data $G_P(x_0^i)$

---

[1]The integrand in Eq. (F.1.3) should really be divided by $(1+\exp(-\beta\omega))$, but we neglect this effect because $\omega_0\beta \simeq 8.8$.

A_1/T^3	463.911
ω_0/T	8.394
A_2	5.727

Table F.1: Fit parameters corresponding to $G_P^{\text{fit}}(x_0)$. Dimensionful quantities are made dimensionless by dividing with $T = 1/128a$. No renormalization constants are included.
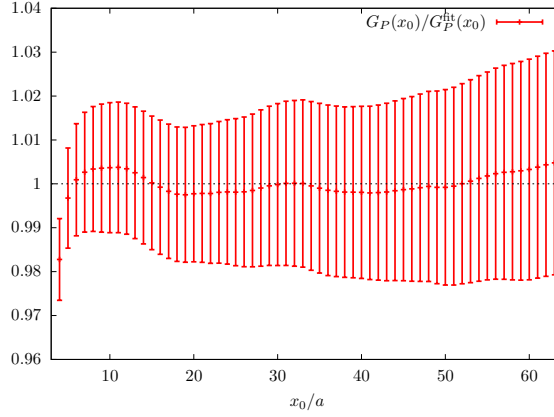

Figure F.1: Euclidean correlator $G_P(x_0)$ divided by its fit function $G_P^{\text{fit}}(x_0)$.

where i and j label the discrete lattice points. The eigenvalues and eigenvectors of S are obtained by solving the eigenvalue equation

$$Sv^{(i)} = (\sigma^2)^{(i)}v^{(i)}. \tag{F.1.6}$$

The statistically independent observables $U^{(i)}$ with squared variance $(\sigma^2)^{(i)}$ are linear combinations of the points $G_P(x_0^i)$,

$$U^{(i)} = (V^T)_{ij}G_P(x_0^j), \tag{F.1.7}$$

where the orthogonal matrix V carries the eigenvectors written in columns and diagonalizes S via $V^TSV = D$. Random values $\delta U^{(i)}$ are generated according to the normalized gaussian probability distribution

$$P(\delta U^{(i)}) = \frac{1}{\sqrt{2\pi(\sigma^2)^{(i)}}}e^{-\frac{(\delta U^{(i)})^2}{2(\sigma^2)^{(i)}}} \tag{F.1.8}$$

and by back-substitution we obtain the random noise

$$\delta G_P^{\text{fit}}(x_0^i) = (V)_{ij}\,\delta U^{(j)}. \tag{F.1.9}$$

F.2   The Backus-Gilbert method applied to $\tilde{G}_P^{\text{fit}}(x_0)$

We now use the Backus-Gilbert algorithm on the mock-data $\tilde{G}_P^{\text{fit}}(x_0)$ with the goal to 'reproduce' the spectral function $\rho_P(\omega)$ with parameters in Table F.1. We write the following identity based on Eq. F.1.3

$$\tilde{G}_P^{\text{fit}}(x_0) = \int_0^\infty d\omega\,\left(\frac{\rho_P(\omega)}{\omega^2}\right)\underbrace{\omega^2\left(e^{-\omega x_0} + e^{-\omega(\beta - x_0)}\right)}_{\doteq K(x_0,\omega)}. \tag{F.2.1}$$

so that the output $\hat{\rho}_{\text{BG}}(\omega)$ of the Backus-Gilbert method is a 'filtered' version of $\frac{\rho_P(\omega)}{\omega^2}$,

$$\hat{\rho}_{\text{BG}}(\bar{\omega}) = \int_0^\infty d\omega\,\hat{\delta}(\bar{\omega},\omega)\left(\frac{\rho_P(\omega)}{\omega^2}\right). \tag{F.2.2}$$

The results are shown in the left panel of Fig. F.2, which corresponds to a value of the regulating parameter $\lambda = 0.25$, and the points considered in the Backus-Gilbert method belong to the interval $x_0^i/a \in [5, 20]$. Consequently, the dimension of all matrices and vectors defined previously is $M = 16$. In view of Fig. F.2 one sees that the location of the pion pole agrees with the value quoted in Table F.1. The same is true for the height of the threshold, whose expectation is $\frac{A_2 N_c}{(4\pi)^2}$ and its flatness is consistent with the assumed ω^2-growth of $\rho_P(\omega)$.

λ	a_{BG}/T^3
0.25	$1.540(28) \times 10^4$
0.05	$1.536(23) \times 10^4$
0.005	$1.540(20) \times 10^4$

Table F.2: The estimator a_{BG}/T^3 as defined in Eq. F.3.1 with $T = 1/128a$ for different values of λ evaluated at $\omega = \omega_0$. The expected value $\frac{A_1}{2}e^{\omega_0\beta/2} = 1.54255 \times 10^4$.
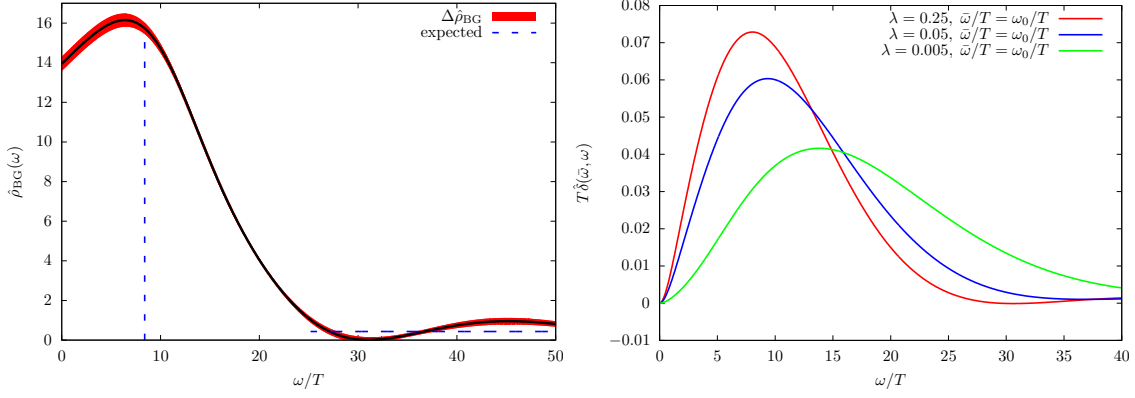
Figure F.2: Left: Estimator $\hat{\rho}_{\mathrm{BG}}(\omega)$ with $\lambda = 0.25$. Expected values are shown as dashed blue lines. Left: Resolution functions $\hat{\delta}(\omega_0, \omega)$ for different values of λ.
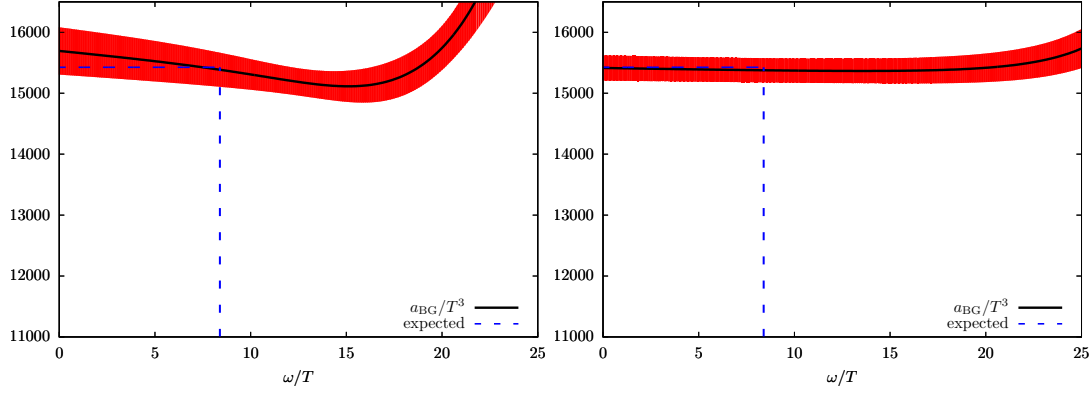

Figure F.3: The estimator a_{BG}/T^3 as defined in Eq. F.3.1 with $T = 1/128a$ as a function of ω Left: $\lambda = 0.25$. Right: $\lambda = 0.005$.

F.3 Extraction of the pion residue

We now extract the residue of the pion in the correlator from the output of the Backus-Gilbert method. As in Eq. (6.5.21), we assume that at small frequencies $\hat{\rho}$ is dominated by the pion and therefore $\rho_P(\omega) = a_{\mathrm{BG}}\delta(\omega - \omega_0) + \dots$. Using Eq. F.2.2, we define an estimator $a_{\mathrm{BG}}(\omega)$,

$$a_{\mathrm{BG}}(\omega) = \frac{\hat{\rho}_{\mathrm{BG}}(\omega)\omega_0^2}{\hat{\delta}(\omega, \omega_0)}, \tag{F.3.1}$$

which we expect in view of Eq. F.1.2 to be equal to $\frac{A_1}{2}e^{\omega_0\beta/2}$ at $\omega = \omega_0$. Table F.2 and Fig. F.3 show that the agreement is excellent and stable as a function of ω.

This study adds to our confidence that the Backus-Gilbert method is a viable approach for spectral function reconstruction in lattice QCD.

To summarize, the interpretation of $\hat{\rho}_{\mathrm{BG}}(\omega)$ in terms of the spectral function is model-independent and determined solely by the resolution function $\hat{\delta}(\bar{\omega}, \omega)$. The latter in turn depends on the regulating parameter λ, which is chosen to balance good resolution in frequency against the statistical precision of $\hat{\rho}_{\mathrm{BG}}(\omega)$. Prior knowledge on the spectral function, such as the existence of a sharp excitation, can be used a posteriori to extract its amplitude in the correlator.

Appendix G

Chiral perturbation theory predictions for finite-T observables

The one-loop results of [113] for the finite-temperature and finite-size effects on the chiral observables can be written as

$$\frac{\mathcal{O}(T,L)}{\mathcal{O}(0,\infty)} = 1 - \nu_{\mathcal{O}} \frac{m_\pi^2}{f_\pi^2} \tilde{g}_1(m_\pi/T, m_\pi L), \tag{G.0.1}$$

$$\nu_{f_\pi} = 1, \qquad \nu_{m_\pi} = -\frac{1}{4}, \qquad \nu_{\langle \bar{\psi}\psi \rangle} = \frac{3}{2}, \tag{G.0.2}$$

$$\tilde{g}_1(x,y) = \frac{1}{(4\pi)^2} \sum_{n_1,n_2,n_3,n_4} \int_0^\infty d\lambda \lambda^{-2} \exp\left[-\lambda - \frac{1}{4\lambda}(y^2(n_1^2 + n_2^2 + n_3^2) + x^2 n_4^2)\right]. \tag{G.0.3}$$

On the right-hand side, m_π and f_π are understood to be the zero-temperature, infinite-volume quantities. The sum runs over four integers, where the term $(n_1, n_2, n_3, n_4) = (0,0,0,0)$ is to be omitted. In addition to showing

$$\frac{f_\pi(T,\infty)}{f_\pi(0,\infty)}, \qquad \frac{m_\pi(T,\infty)}{m_\pi(0,\infty)}, \qquad \frac{\langle \bar{\psi}\psi \rangle (T,\infty)}{\langle \bar{\psi}\psi \rangle (0,\infty)}, \tag{G.0.4}$$

as a function of T, we also display the curves

$$\frac{f_\pi(T, 2/T)}{f_\pi(0, L_{\text{ref}})}, \qquad \frac{m_\pi(T, 2/T)}{m_\pi(0, L_{\text{ref}})}, \qquad \frac{\langle \bar{\psi}\psi \rangle (T, 2/T)}{\langle \bar{\psi}\psi \rangle (0, L_{\text{ref}})} \tag{G.0.5}$$

153

in Fig. 6.6, Fig. 6.7), where L_{ref} corresponds to the spatial linear size of the A_5 ensemble. In this way the finite size ($L = 2/T$) of the spatial volume in our thermal ensembles are taken into account in the comparison with the predictions of chiral perturbation theory.

We want to show how to derive these equations starting with the ChPT Lagrangian written in Eq. (3.3.8) for the two flavor theory with degenerate quark masses focusing only on the temperature corrections.

G.1   Quark condensate

When matching QCD to ChPT, the first step is always to find the corresponding operator in ChPT in terms of the matrices U and $U^\dagger$ and its derivatives that corresponds to the desired operator in QCD. For this purpose, one couples both the QCD and ChPT lagrangian densities to external sources (a detailed derivation on the generating functional can be found in [33]) which then are used to take functional derivatives with respect to them so as to truly match all Green Functions. The Quark condensate $\langle \bar{\psi}\psi \rangle$ in QCD can be derived in ChPT by taking one functional derivative with respect to the scalar source s^0 with $s = \sum_{a=0}^{3} s^a \tau^a$ and $\tau^0 = \delta^{ab}$. In this way we obtain the following correspondence

$$\frac{F^2\Sigma}{2}\text{Tr}\{U(x) + U^\dagger(x)\} = -\bar{\psi}(x)\psi(x). \tag{G.1.1}$$

The next step is to expand the U matrices in terms of the fields $\phi(x) = \phi^a(x)\tau^a$ to next to leading order and we get

$$\langle \bar{\psi}\psi \rangle = -2F^2\Sigma \left\{ 1 - \frac{1}{4F^2} \left\langle \text{Tr}\{\tau^a\tau^b\}\phi^a(x)\phi^b(x) \right\rangle \right\} \tag{G.1.2}$$

Evaluating the trace yields $\text{Tr}\{\tau^a\tau^b\} = 2\delta^{ab}$ and we define the thermal propagator in euclidean metric

$$\Delta^T(x - y)\delta^{ab} = \left\langle \phi^a(x)\phi^b(y) \right\rangle = \delta^{ab}T \sum_{p_0} \int \frac{d^3p}{(2\pi)^3} \frac{e^{ip(x-y)}}{p_0^2 + E_{\mathbf{p}}^2} \tag{G.1.3}$$

with $E_{\mathbf{p}}^2 = \mathbf{p}^2 + M^2$, $p_0 = 2\pi n_0 T$ and $n \in \mathbb{Z}$. The final formula then reads

$$\langle \bar{\psi}\psi \rangle = -2F^2 \Sigma \left\{ 1 - \frac{3}{2F^2} \Delta^T(0) \right\} + \text{higher orders.} \qquad (\text{G.1.4})$$

We will mention how to convert the thermal propagator into the g_1 function at the end of this chapter.

G.2 Screening pion mass

The screening mass m_π can be calculated by looking at the spatial dependence of the axial two-point function. It was first introduced in Eq. (6.2.16) and plays an important role in the analysis presented in Chapter 6

$$G_A^{\text{s}}(x_3)\delta^{ab} = \int dx_0 \, d^2x_\perp \langle A_3^a(x) A_3^b(0) \rangle \sim e^{-m_\pi |x_3|}. \qquad (\text{G.2.1})$$

Following the same strategy as in the previous section, one derives by taking functional derivatives, the form of the axial current operator in ChPT which reads

$$A_\mu^a(x) = -\frac{F^2}{4} \text{Tr} \left\{ \tau^a \{ U(x), \partial_\mu U^\dagger(x) \} \right\}. \qquad (\text{G.2.2})$$

Expanding the U matrices to leading order one arrives

$$A_\mu^a(x) = -\frac{F^2}{4} \text{Tr} \left\{ \tau^a \left\{ -\frac{2i}{F} \partial_\mu \phi(x) \right\} \right\}. \qquad (\text{G.2.3})$$

The lowest order corresponds to two insertions of the field ϕ. This terms contributes as ($\mu = 3$)

$$\left(\frac{F^2}{4} \right)^2 \left(\frac{-2i}{F} \right)^2 4\delta^{ac}\delta^{bd} \langle \partial_3 \phi^c(x) \partial_3 \phi^d(0) \rangle. \qquad (\text{G.2.4})$$

Performing the integral over the perpendicular space to x_3, $\int_0^{1/T} dx_0 \int dx_1 dx_2$ yields for the previous expectation value

$$
\int_0^{1/T} dx_0 \int dx_1 dx_2 \left\langle \partial_3 \phi^c(x) \partial_3 \phi^d(0) \right\rangle = T \int_0^{1/T} dx_0 \int dx_1 dx_2 \sum_{p_0} \int \frac{d^3 p}{(2\pi)^3} \, p_3^2 \frac{e^{ipx}}{p_0^2 + E_{\mathbf{p}}^2}
$$
$$
= -\frac{M}{2} e^{-Mx_3} \tag{G.2.5}
$$

and we get the leading order term

$$
G_A^{\text{rs}}(x_3)_{\text{LO}} \delta^{ab} = \delta^{ab} \frac{F^2 M}{2} e^{-Mx_3}. \tag{G.2.6}
$$

A correction to the exponent mass can only appear from a one-loop self-energy graph. For doing this, the 4-pion-interaction-vertex $V^{abcd}(p_a, p_b, p_c, p_d)$ coming from the lowest order chiral Lagrangian is needed (see [33] or Appendix of [125]). We expect a linear term in x_3 since the mass appearing in the exponent will be corrected as $m_\pi = M(1 + a\epsilon)$ and consequently we will obtain a term

$$
\delta^{ab} \frac{F^2 M}{2} e^{-Mx_3} (1 - aMx_3\epsilon) + \text{other terms} + \mathcal{O}(\epsilon^2). \tag{G.2.7}
$$

The expression one needs to evaluate coming from the self-energy diagram with all prefactors included is

$$
\left(\frac{F^2}{4}\right)^2 \left(\frac{-2i}{F}\right)^2 \left(\frac{1}{2}\right) 4T^2 \sum_{k_0, p_0} \int \frac{d^3 k}{(2\pi)^3} \int \frac{d^3 p}{(2\pi)^3} \frac{p_3^2 e^{ipx}}{(p^2 + M^2)^2} \frac{V^{ab}(p, k)}{k^2 + M^2} \tag{G.2.8}
$$

with $V^{ab}(p, k) = \frac{\delta^{ab}}{3F^2}(5M^2 + (p-k)^2)$. The factor of $1/2$ is the symmetry factor of the diagram. The integrals over the perpendicular space project onto $p_0 = p_1 = p_2 = 0$. Linear terms in k vanish and the single term linear in x_3 appears because of the derivative one needs to take in order calculate the residue coming from the double pole in p_3. The linear term in x_3 appears as

$$
-\frac{M^2}{8} e^{-Mx_3} \Delta^T(0) x_3 \tag{G.2.9}
$$

Adding the free result we obtain

$$\delta^{ab}\frac{F^2 M}{2}e^{-Mx_3}\left(1-\frac{\Delta^T(0)}{4F^2}Mx_3\right) \tag{G.2.10}$$

from which we conclude that $a=\frac{1}{4}$ and $\epsilon=\frac{\Delta^T(0)}{F^2}$. Consequently

$$m_\pi = M(1+\frac{\Delta^T(0)}{4F^2})+\text{higher orders.} \tag{G.2.11}$$

G.3   Screening pion decay constant

Once the chiral condensate correction and the screening mass have been calculated, we can make use of the GOR relation. It was first introduced in Eq. (6.1.4). It is a relation valid at leading order in the quark mass expansion. At this order of the temperature expansion the GOR relation still holds. Therefore we can just solve for f_π by performing a Taylor expansion of the corrections to the quark condensate and of the screening mass. In this way we get

$$f_\pi = \left(-\frac{m\left\langle\bar\psi\psi\right\rangle}{m_\pi^2}\right)^{1/2}. \tag{G.3.1}$$

Inserting the previously calculated expression we manage to obtain

$$f_\pi = F(1-\frac{\Delta^T(0)}{F^2})+\text{higher orders.} \tag{G.3.2}$$

G.4   The function $\Delta^T(0)$ at finite volume

We will consider the case where not only the time component of the momentum vector is quantized in units of $2\pi\beta$ but also the spatial components appear proportional to $2\pi/L$. The starting point is the function

$$\Delta^T(0) = \frac{T}{L^3}\sum_{p_0,p_1,p_2,p_3}\frac{1}{p_0^2+E_{\mathbf{p}}^2} \tag{G.4.1}$$

We use Poisson summation formula on all four variables together with the Schwinger representation of the propagator $\frac{1}{a^2+b^2} = \int_0^\infty d\lambda e^{-\lambda(a^2+b^2)}$

$$\sum_{n_0,n_1,n_2,n_3} \int_0^\infty d\lambda \int \frac{d^4p}{(2\pi)^4} \exp\left(-\lambda(p_0^2 + E_{\mathbf{p}}^2) + i(p_0 n_0 \beta + p_1 n_1 L + p_2 n_2 L + p_3 n_3 L)\right)$$

(G.4.2)

Completing squares and doing the change of variables

$$p_0' = p_0 - i\frac{n_0\beta}{2\lambda} \tag{G.4.3}$$

$$p_i' = p_i - i\frac{n_i L}{2\lambda} \tag{G.4.4}$$

yields

$$\int_0^\infty d\lambda \int \frac{d^4p'}{(2\pi)^4} \exp\left(-\lambda(p_0'^2 + p_i'p_i') - \lambda(\frac{\mathbf{n}^2}{4\lambda} + \lambda M^2)\right) \tag{G.4.5}$$

with $\mathbf{n} = (n_0\beta, n_1 L, n_2 L, n_3 L)$. The four gaussian integrals can be calculated straightforwardly giving a factor $\left(\frac{\pi}{\lambda}\right)^2$ and we obtain

$$\Delta^T(0) = \frac{1}{(4\pi)^2} \sum_{n_0,n_1,n_2,n_3} \int_0^\infty d\lambda \frac{1}{\lambda^2} \exp\left(-\lambda M^2 - \frac{\mathbf{n}^2}{4\lambda}\right). \tag{G.4.6}$$

Simple algebra manipulations lead to the form written in Eq. (G.0.3). The term $\mathbf{n} = (0,0,0,0)$ is to be omitted since it corresponds to the infinite volume and zero temperature contribution. This integral form is specially suited for numerical implementation since the integral will converge fast because of the damping term in the exponent. Therefore, only a couple of terms in the sum are needed to approximate the function (e.g. from $-10 \leq n_\mu \leq 10$, $\mu = 0, ..., 3$). In addition a Table can be produced with all possible norms of the vector $\mathbf{n}$ and its corresponding degeneracy. In this way, one reduces the 4-dimensional sum to a simple sum over norms times each degeneracy.

Bibliography

[1] **CMS** Collaboration, S. Chatrchyan *et. al.*, *Observation of a new boson at a mass of 125 GeV with the CMS experiment at the LHC*, Phys. Lett. **B716** (2012) 30–61, [`arXiv:1207.7235`].

[2] **ATLAS** Collaboration, G. Aad *et. al.*, *Observation of a new particle in the search for the Standard Model Higgs boson with the ATLAS detector at the LHC*, Phys. Lett. **B716** (2012) 1–29, [`arXiv:1207.7214`].

[3] P. W. Higgs, *Broken Symmetries and the Masses of Gauge Bosons*, Phys. Rev. Lett. **13** (1964) 508–509.

[4] F. Englert and R. Brout, *Broken Symmetry and the Mass of Gauge Vector Mesons*, Phys. Rev. Lett. **13** (1964) 321–323.

[5] **RENO** Collaboration, J. K. Ahn *et. al.*, *Observation of Reactor Electron Antineutrino Disappearance in the RENO Experiment*, Phys. Rev. Lett. **108** (2012) 191802, [`arXiv:1204.0626`].

[6] **HotQCD** Collaboration, A. Bazavov *et. al.*, *The chiral transition and $U(1)_A$ symmetry restoration from lattice QCD using Domain Wall Fermions*, Phys.Rev. **D86** (2012) 094503, [`arXiv:1205.3535`].

[7] S. Borsanyi, S. Durr, Z. Fodor, C. Hoelbling, S. D. Katz, *et. al.*, *QCD thermodynamics with continuum extrapolated Wilson fermions I*, JHEP **1208** (2012) 126, [`arXiv:1205.0440`].

159

[8] D. Teaney, *Finite temperature spectral densities of momentum and R-charge correlators in N = 4 Yang Mills theory*, Phys. Rev. **D74** (2006) 045025, [`hep-ph/0602044`].

[9] S. Durr *et. al.*, *Ab-Initio Determination of Light Hadron Masses*, Science **322** (2008) 1224–1227, [`arXiv:0906.3599`].

[10] H. Lehmann, K. Symanzik, and W. Zimmermann, *On the formulation of quantized field theories*, Nuovo Cim. **1** (1955) 205–225.

[11] J. I. Kapusta and C. Gale, *Finite-temperature field theory: Principles and applications.* Cambridge University Press, 2006. 428.

[12] H. B. Meyer, *Transport Properties of the Quark-Gluon Plasma: A Lattice QCD Perspective*, Eur.Phys.J. **A47** (2011) 86, [`arXiv:1104.3708`].

[13] G. Aarts and J. M. Martinez Resco, *Transport coefficients, spectral functions and the lattice*, JHEP **04** (2002) 053, [`hep-ph/0203177`].

[14] G. Aarts and J. M. Martinez Resco, *Continuum and lattice meson spectral functions at nonzero momentum and high temperature*, Nucl. Phys. **B726** (2005) 93–108, [`hep-lat/0507004`].

[15] Y. Nakahara, M. Asakawa, and T. Hatsuda, *Hadronic spectral functions in lattice QCD*, Phys. Rev. **D60** (1999) 091503, [`hep-lat/9905034`].

[16] M. Asakawa, T. Hatsuda, and Y. Nakahara, *Maximum entropy analysis of the spectral functions in lattice QCD*, Prog. Part. Nucl. Phys. **46** (2001) 459–508, [`hep-lat/0011040`].

[17] **CP-PACS** Collaboration, T. Yamazaki *et. al.*, *Spectral function and excited states in lattice QCD with maximum entropy method*, Phys. Rev. **D65** (2002) 014501, [`hep-lat/0105030`].

[18] B. B. Brandt, A. Francis, H. B. Meyer, and D. Robaina, *Chiral dynamics in the low-temperature phase of QCD*, Phys.Rev. **D90** (2014) 054509, [`arXiv:1406.5602`].

[19] A. Kirsch, B. Schomburg, and G. Berendt, *The backus-gilbert method*, Inverse Problems **4** (1988), no. 3 771.

[20] H. Haarioa and E. Somersalo, *The backus-gilbert method revisited: background, implementation and examples*, Numerical Functional Analysis and Optimization **9** (1987) 917–943.

[21] B. Schomburg and G. Berendt, *On the convergence of the backus-gilbert algorithm*, Inverse problems **3** (1987), no. 2 341.

[22] J. C. Ward, *An Identity in Quantum Electrodynamics*, Phys. Rev. **78** (1950) 182.

[23] Y. Takahashi, *On the generalized Ward identity*, Nuovo Cim. **6** (1957) 371.

[24] A. Vladikas, *Three Topics in Renormalization and Improvement*, in *Modern perspectives in lattice QCD: Quantum field theory and high performance computing. Proceedings, International School, 93rd Session, Les Houches, France, August 3-28, 2009*, pp. 161–222, 2011. `arXiv:1103.1323`.

[25] E. Noether, *Invariante variationsprobleme*, Nachr. D. König. Gesellsch. D. Wiss. Zu Göttingen, Math-phys. Klasse (1918) 235–257.

[26] D. J. Gross and F. Wilczek, *Ultraviolet Behavior of Non-Abelian Gauge Theories*, Phys. Rev. Lett. **30** (1973) 1343–1346.

[27] M. Srednicki, *Quantum field theory*. Cambridge University Press, 2007.

[28] **Particle Data Group** Collaboration, K. A. Olive *et. al.*, *Review of Particle Physics*, Chin. Phys. **C38** (2014) 090001.

[29] S. L. Adler, *Axial vector vertex in spinor electrodynamics*, Phys.Rev. **177** (1969) 2426–2438.

[30] J. Bell and R. Jackiw, *A PCAC puzzle: $\pi_0 \to \gamma\gamma$ in the sigma model*, Nuovo Cim. **A60** (1969) 47–61.

[31] J. Goldstone, *Field Theories with Superconductor Solutions*, Nuovo Cim. **19** (1961) 154–164.

[32] J. Goldstone, A. Salam, and S. Weinberg, *Broken Symmetries*, Phys. Rev. **127** (1962) 965–970.

[33] S. Scherer, *Introduction to chiral perturbation theory*, Adv. Nucl. Phys. **27** (2003) 277, [`hep-ph/0210398`].

[34] R. P. Feynman and M. Gell-Mann, *Theory of Fermi interaction*, Phys. Rev. **109** (1958) 193–198.

[35] S. Weinberg, *Phenomenological Lagrangians*, Physica **A96** (1979) 327.

[36] K. G. Wilson, *Confinement of quarks*, Phys. Rev. **D10** (1974) 2445–2459.

[37] M. Creutz, L. Jacobs, and C. Rebbi, *Monte Carlo Study of Abelian Lattice Gauge Theories*, Phys. Rev. **D20** (1979) 1915.

[38] M. Creutz, *Monte Carlo Study of Quantized SU(2) Gauge Theory*, Phys. Rev. **D21** (1980) 2308–2315.

[39] W. Bietenholz, U. Gerber, M. Pepe, and U.-J. Wiese, *Topological Lattice Actions*, JHEP **1012** (2010) 020, [`arXiv:1009.2146`].

[40] K. Symanzik, *Continuum Limit and Improved Action in Lattice Theories. 1. Principles and phi**4 Theory*, Nucl. Phys. **B226** (1983) 187.

[41] K. Symanzik, *Continuum Limit and Improved Action in Lattice Theories. 2. O(N) Nonlinear Sigma Model in Perturbation Theory*, Nucl. Phys. **B226** (1983) 205.

[42] B. Sheikholeslami and R. Wohlert, *Improved Continuum Limit Lattice Action for QCD with Wilson Fermions*, Nucl. Phys. **B259** (1985) 572.

[43] **ALPHA** Collaboration, K. Jansen and R. Sommer, *O(α) improvement of lattice QCD with two flavors of Wilson quarks*, Nucl.Phys. **B530** (1998) 185–203, [`hep-lat/9803017`].

[44] S. Sint, *On the Schrödinger functional in QCD*, Nucl. Phys. **B421** (1994) 135–158, [`hep-lat/9312079`].

[45] S. Sint, *One loop renormalization of the QCD Schrödinger functional*, Nucl. Phys. **B451** (1995) 416–444, [`hep-lat/9504005`].

[46] R. Sommer, *A New way to set the energy scale in lattice gauge theories and its applications to the static force and alpha-s in SU(2) Yang-Mills theory*, *Nucl. Phys.* **B411** (1994) 839–854, [`hep-lat/9310022`].

[47] T. Bhattacharya, R. Gupta, W. Lee, S. R. Sharpe, and J. M. S. Wu, *Improved bilinears in lattice QCD with non-degenerate quarks*, *Phys. Rev.* **D73** (2006) 034504, [`hep-lat/0511014`].

[48] G. Martinelli, C. Pittori, C. T. Sachrajda, M. Testa, and A. Vladikas, *A General method for nonperturbative renormalization of lattice operators*, *Nucl.Phys.* **B445** (1995) 81–108, [`hep-lat/9411010`].

[49] **ALPHA** Collaboration, M. Guagnelli *et. al.*, *Nonperturbative results for the coefficients b(m) and b(a) - b(P) in O(a) improved lattice QCD*, *Nucl.Phys.* **B595** (2001) 44–62, [`hep-lat/0009021`].

[50] P. Fritzsch, F. Knechtli, B. Leder, M. Marinkovic, S. Schaefer, *et. al.*, *The strange quark mass and Lambda parameter of two flavor QCD*, *Nucl.Phys.* **B865** (2012) 397–429, [`arXiv:1205.5380`].

[51] L. Giusti and H. B. Meyer, *Thermal momentum distribution from path integrals with shifted boundary conditions*, *Phys.Rev.Lett.* **106** (2011) 131601, [`arXiv:1011.2727`].

[52] L. Giusti and H. B. Meyer, *Thermodynamic potentials from shifted boundary conditions: the scalar-field theory case*, *JHEP* **1111** (2011) 087, [`arXiv:1110.3136`].

[53] L. Giusti and H. B. Meyer, *Implications of Poincare symmetry for thermal field theories in finite-volume*, *JHEP* **1301** (2013) 140, [`arXiv:1211.6669`].

[54] C. Sachrajda and G. Villadoro, *Twisted boundary conditions in lattice simulations*, *Phys.Lett.* **B609** (2005) 73–85, [`hep-lat/0411033`].

[55] D. H. Weingarten and D. N. Petcher, *Monte Carlo Integration for Lattice Gauge Theories with Fermions*, *Phys. Lett.* **B99** (1981) 333.

[56] W. H. Press, S. A. Teukolsky, W. T. Vetterling, and B. P. Flannery, *Numerical Recipes: The Art of Scientific Computing*, . Cambridge, UK: Univ. Pr. (2007).

[57] M. Lüscher, *Advanced lattice QCD*, `hep-lat/9802029`.

[58] M. Lüscher, *Deflation acceleration of lattice QCD simulations*, *JHEP* **0712** (2007) 011, [`arXiv:0710.5417`].

[59] C. Gattringer and C. B. Lang, *Quantum chromodynamics on the lattice*, *Lect. Notes Phys.* **788** (2010) 1–211.

[60] H. J. Rothe, *Lattice gauge theories: An Introduction*, *World Sci. Lect. Notes Phys.* **43** (1992) 1–381.

[61] M. Della Morte and L. Giusti, *Symmetries and exponential error reduction in Yang-Mills theories on the lattice*, *Comput. Phys. Commun.* **180** (2009) 819–826, [`arXiv:0806.2601`].

[62] M. Della Morte and L. Giusti, *A novel approach for computing glueball masses and matrix elements in Yang-Mills theories on the lattice*, *JHEP* **1105** (2011) 056, [`arXiv:1012.2562`].

[63] D. Robaina and H. B. Meyer, *Renormalization of the momentum density on the lattice using shifted boundary conditions*, *PoS* **LATTICE2013** (2014) 323, [`arXiv:1310.6075`].

[64] M. Gockeler, R. Horsley, E.-M. Ilgenfritz, H. Perlt, P. E. Rakow, *et. al.*, *Lattice operators for moments of the structure functions and their transformation under the hypercubic group*, *Phys.Rev.* **D54** (1996) 5705–5714, [`hep-lat/9602029`].

[65] S. Caracciolo, P. Menotti, and A. Pelissetto, *Analytic determination at one loop of the energy momentum tensor for lattice QCD*, *Phys. Lett.* **B260** (1991) 401–406.

[66] **ALPHA** Collaboration, S. Schaefer, R. Sommer, and F. Virotta, *Critical slowing down and error analysis in lattice QCD simulations*, *Nucl.Phys.* **B845** (2011) 93–119, [`arXiv:1009.5228`].

[67] N. Cabibbo and E. Marinari, *A New Method for Updating SU(N) Matrices in Computer Simulations of Gauge Theories*, *Phys. Lett.* **B119** (1982) 387–390.

[68] S. Necco and R. Sommer, *The N(f) = 0 heavy quark potential from short to intermediate distances*, *Nucl. Phys.* **B622** (2002) 328–346, [`hep-lat/0108008`].

[69] G. Boyd *et. al.*, *Thermodynamics of SU(3) Lattice Gauge Theory*, *Nucl. Phys.* **B469** (1996) 419–444, [`hep-lat/9602007`].

[70] L. Giusti and M. Pepe, *Energy-momentum tensor on the lattice: Nonperturbative renormalization in Yang-Mills theory*, *Phys. Rev.* **D91** (2015) 114504, [`arXiv:1503.0704`].

[71] M. Lüscher and S. Schaefer, *Lattice QCD with open boundary conditions and twisted-mass reweighting*, *Comput.Phys.Commun.* **184** (2013) 519–528, [`arXiv:1206.2809`].

[72] Compressed Baryonic Matter (CBM) Experiment at the Facility for Antiproton and Ion Research (FAIR) at GSI Darmstadt *http://www.gauss-centre.eu/gauss-centre/EN/Projects/ElementaryParticlePhysics/2015/philipsen_PDNM.html?nn=1361054*.

[73] J. B. Kogut and M. A. Stephanov, *The phases of quantum chromodynamics: From confinement to extreme environments*, *Camb. Monogr. Part. Phys. Nucl. Phys. Cosmol.* **21** (2004) 1–364.

[74] R. D. Pisarski and F. Wilczek, *Remarks on the Chiral Phase Transition in Chromodynamics*, *Phys. Rev.* **D29** (1984) 338–341.

[75] **tmfT** Collaboration, F. Burger, E.-M. Ilgenfritz, M. Kirchner, M. P. Lombardo, M. Mller-Preussker, O. Philipsen, C. Urbach, and L. Zeidlewicz, *Thermal QCD transition with two flavors of twisted mass fermions*, *Phys. Rev.* **D87** (2013), no. 7 074508, [`arXiv:1102.4530`].

[76] V. Bornyakov, R. Horsley, S. Morozov, Y. Nakamura, M. Polikarpov, *et. al.*, *Probing the finite temperature phase transition with Nf = 2 nonperturbatively improved Wilson fermions*, *Phys.Rev.* **D82** (2010) 014504, [`arXiv:0910.2392`].

[77] A. Andronic, P. Braun-Munzinger, and J. Stachel, *Hadron production in central nucleus nucleus collisions at chemical freeze-out, Nucl. Phys.* **A772** (2006) 167–199, [`nucl-th/0511071`].

[78] J. Casalderrey-Solana, H. Liu, D. Mateos, K. Rajagopal, and U. A. Wiedemann, *Gauge/String Duality, Hot QCD and Heavy Ion Collisions*, `arXiv:1101.0618`.

[79] P. Braun-Munzinger, K. Redlich, and J. Stachel, *Particle production in heavy ion collisions*, `nucl-th/0304013`.

[80] A. Bazavov *et. al.*, *Equation of state and QCD transition at finite temperature, Phys. Rev.* **D80** (2009) 014504, [`arXiv:0903.4379`].

[81] D. Teaney, J. Lauret, and E. V. Shuryak, *A Hydrodynamic description of heavy ion collisions at the SPS and RHIC*, `nucl-th/0110037`.

[82] G. Policastro, D. T. Son, and A. O. Starinets, *The shear viscosity of strongly coupled N = 4 supersymmetric Yang-Mills plasma, Phys. Rev. Lett.* **87** (2001) 081601, [`hep-th/0104066`].

[83] B. B. Brandt, A. Francis, H. B. Meyer, and D. Robaina, *Pion quasiparticle in the low-temperature phase of QCD, Phys. Rev.* **D92** (2015), no. 9 094510, [`1506.05732`].

[84] B. B. Brandt, A. Francis, H. B. Meyer, and D. Robaina, *Chiral dynamics in the low-temperature phase of QCD, PoS* **LATTICE2014** (2015) 234, [`arXiv:1410.5981`].

[85] B. B. Brandt, A. Francis, H. B. Meyer, and D. Robaina, *The pion quasiparticle in the low-temperature phase of QCD, PoS* **CD 2015** (2015) [`1509.06241`].

[86] **HotQCD** Collaboration, A. Bazavov *et. al.*, *Fluctuations and Correlations of net baryon number, electric charge, and strangeness: A comparison of lattice QCD results with the hadron resonance gas model, Phys.Rev.* **D86** (2012) 034509, [`arXiv:1203.0784`].

[87] S. Borsanyi, Z. Fodor, C. Hoelbling, S. D. Katz, S. Krieg, *et. al.*, *Full result for the QCD equation of state with 2+1 flavors*, *Phys.Lett.* **B730** (2014) 99–104, [`arXiv:1309.5258`].

[88] S. Borsanyi, Z. Fodor, S. D. Katz, S. Krieg, C. Ratti, *et. al.*, *Fluctuations of conserved charges at finite temperature from lattice QCD*, *JHEP* **1201** (2012) 138, [`arXiv:1112.4416`].

[89] P. Braun-Munzinger, B. Friman, F. Karsch, K. Redlich, and V. Skokov, *Net-charge probability distributions in heavy ion collisions at chemical freeze-out*, *Nucl.Phys.* **A880** (2012) 48–64, [`arXiv:1111.5063`].

[90] J. Stachel, A. Andronic, P. Braun-Munzinger, and K. Redlich, *Confronting LHC data with the statistical hadronization model*, `arXiv:1311.4662`.

[91] E. V. Shuryak, *Physics of the pion liquid*, *Phys.Rev.* **D42** (1990) 1764–1776.

[92] J. Goity and H. Leutwyler, *On the Mean Free Path of Pions in Hot Matter*, *Phys.Lett.* **B228** (1989) 517.

[93] A. Schenk, *Absorption and dispersion of pions at finite temperature*, *Nucl.Phys.* **B363** (1991) 97–116.

[94] A. Schenk, *Pion propagation at finite temperature*, *Phys.Rev.* **D47** (1993) 5138–5155.

[95] D. Toublan, *Pion dynamics at finite temperature*, *Phys.Rev.* **D56** (1997) 5629–5645, [`hep-ph/9706273`].

[96] R. D. Pisarski and M. Tytgat, *Propagation of cool pions*, *Phys.Rev.* **D54** (1996) 2989–2993, [`hep-ph/9604404`].

[97] D. T. Son and M. A. Stephanov, *Pion propagation near the QCD chiral phase transition*, *Phys. Rev. Lett.* **88** (2002) 202302, [`hep-ph/0111100`].

[98] D. T. Son and M. A. Stephanov, *Real-time pion propagation in finite-temperature QCD*, *Phys. Rev.* **D66** (2002) 076011, [`hep-ph/0204226`].

[99] B. B. Brandt, A. Francis, H. B. Meyer, O. Philipsen, and H. Wittig, *QCD thermodynamics with O(a) improved Wilson fermions at Nf=2*, `arXiv:1310.8326`.

[100] M. Lüscher, S. Sint, R. Sommer, and H. Wittig, *Nonperturbative determination of the axial current normalization constant in O(a) improved lattice QCD, Nucl.Phys.* **B491** (1997) 344–364, [`hep-lat/9611015`].

[101] H. B. Meyer, *Energy-momentum tensor correlators and viscosity, PoS* **LAT08** (2008) 017, [`arXiv:0809.5202`].

[102] D. Bernecker and H. B. Meyer, *Vector Correlators in Lattice QCD: Methods and applications, Eur.Phys.J.* **A47** (2011) 148, [`arXiv:1107.4388`].

[103] B. B. Brandt, A. Francis, H. B. Meyer, and H. Wittig, *Thermal Correlators in the rho channel of two-flavor QCD, JHEP* **1303** (2013) 100, [`arXiv:1212.4200`].

[104] J. I. Kapusta and E. V. Shuryak, *Weinberg type sum rules at zero and finite temperature, Phys. Rev.* **D49** (1994) 4694–4704, [`hep-ph/9312245`].

[105] M. Hasenbusch, *Speeding up the hybrid Monte Carlo algorithm for dynamical fermions, Phys.Lett.* **B519** (2001) 177–182, [`hep-lat/0107019`].

[106] M. Hasenbusch and K. Jansen, *Speeding up lattice QCD simulations with clover improved Wilson fermions, Nucl.Phys.* **B659** (2003) 299–320, [`hep-lat/0211042`].

[107] M. Marinkovic and S. Schaefer, *Comparison of the mass preconditioned HMC and the DD-HMC algorithm for two-flavour QCD, PoS* **LATTICE2010** (2010) 031, [`arXiv:1011.0911`].

[108] *http://luscher.web.cern.ch/luscher/DD-HMC/index.html* (2010).

[109] M. Bochicchio, L. Maiani, G. Martinelli, G. C. Rossi, and M. Testa, *Chiral Symmetry on the Lattice with Wilson Fermions, Nucl. Phys.* **B262** (1985) 331.

[110] M. Lüscher, S. Sint, R. Sommer, P. Weisz, and U. Wolff, *Nonperturbative O(a) improvement of lattice QCD, Nucl.Phys.* **B491** (1997) 323–343, [`hep-lat/9609035`].

[111] M. Della Morte, R. Hoffmann, and R. Sommer, *Non-perturbative improvement of the axial current for dynamical Wilson fermions*, *JHEP* **0503** (2005) 029, [`hep-lat/0503003`].

[112] M. Gell-Mann, R. Oakes, and B. Renner, *Behavior of current divergences under SU(3) x SU(3)*, *Phys.Rev.* **175** (1968) 2195–2199.

[113] J. Gasser and H. Leutwyler, *Light Quarks at Low Temperatures*, *Phys.Lett.* **B184** (1987) 83.

[114] P. Gerber and H. Leutwyler, *Hadrons Below the Chiral Phase Transition*, *Nucl.Phys.* **B321** (1989) 387.

[115] M. Davier, A. Hocker, and Z. Zhang, *The Physics of hadronic tau decays*, *Rev.Mod.Phys.* **78** (2006) 1043–1109, [`hep-ph/0507078`].

[116] G. P. Engel, L. Giusti, S. Lottini, and R. Sommer, *Spectral density of the Dirac operator in two-flavor QCD*, *Phys.Rev.* **D91** (2015), no. 5 054505, [`arXiv:1411.6386`].

[117] H. B. Meyer, *The Bulk Channel in Thermal Gauge Theories*, *JHEP* **04** (2010) 099, [`arXiv:1002.3343`].

[118] G. Backus and F. Gilbert, *The Resolving Power of Gross Earth Data*, *Geophysical Journal of the Royal Astronomical Society* **16** (1968) 169205.

[119] G. Backus and F. Gilbert, *Uniqueness in the inversion of inaccurate gross earth data*, *Philosophical Transactions of the Royal Society of London A: Mathematical, Physical and Engineering Sciences* **266** (1970), no. 1173 123–192.

[120] H. B. Meyer, *A calculation of the bulk viscosity in SU(3) gluodynamics*, *Phys. Rev. Lett.* **100** (2008) 162001, [`arXiv:0710.3717`].

[121] T. Bhattacharya, M. I. Buchoff, N. H. Christ, H. T. Ding, R. Gupta, et. al., *The QCD phase transition with physical-mass, chiral quarks*, *Phys.Rev.Lett.* **113** (2014) 082001, [`arXiv:1402.5175`].

[122] M. Lüscher, *Schwarz-preconditioned HMC algorithm for two-flavour lattice QCD*, *Comput. Phys. Commun.* **165** (2005) 199–220, [`hep-lat/0409106`].

[123] **ALPHA** Collaboration, U. Wolff, *Monte Carlo errors with less errors*, *Comput. Phys. Commun.* **156** (2004) 143–153, [`hep-lat/0306017`]. [Erratum: Comput. Phys. Commun.176,383(2007)].

[124] K. Chetyrkin, V. Spiridonov, and S. Gorishnii, *Wilson expansion for correlators of vector currents at the two loop level: dimension four operators, Phys.Lett.* **B160** (1985) 149–153.

[125] D. Robaina, *Towards first principle studies of QCD at finite temperature and baryon chemical potential, Master Thesis* (2012).